Influence of viscoelasticity on the kinematics and hydrodynamic interactions of C.Reinhardtii

Anand Sudha

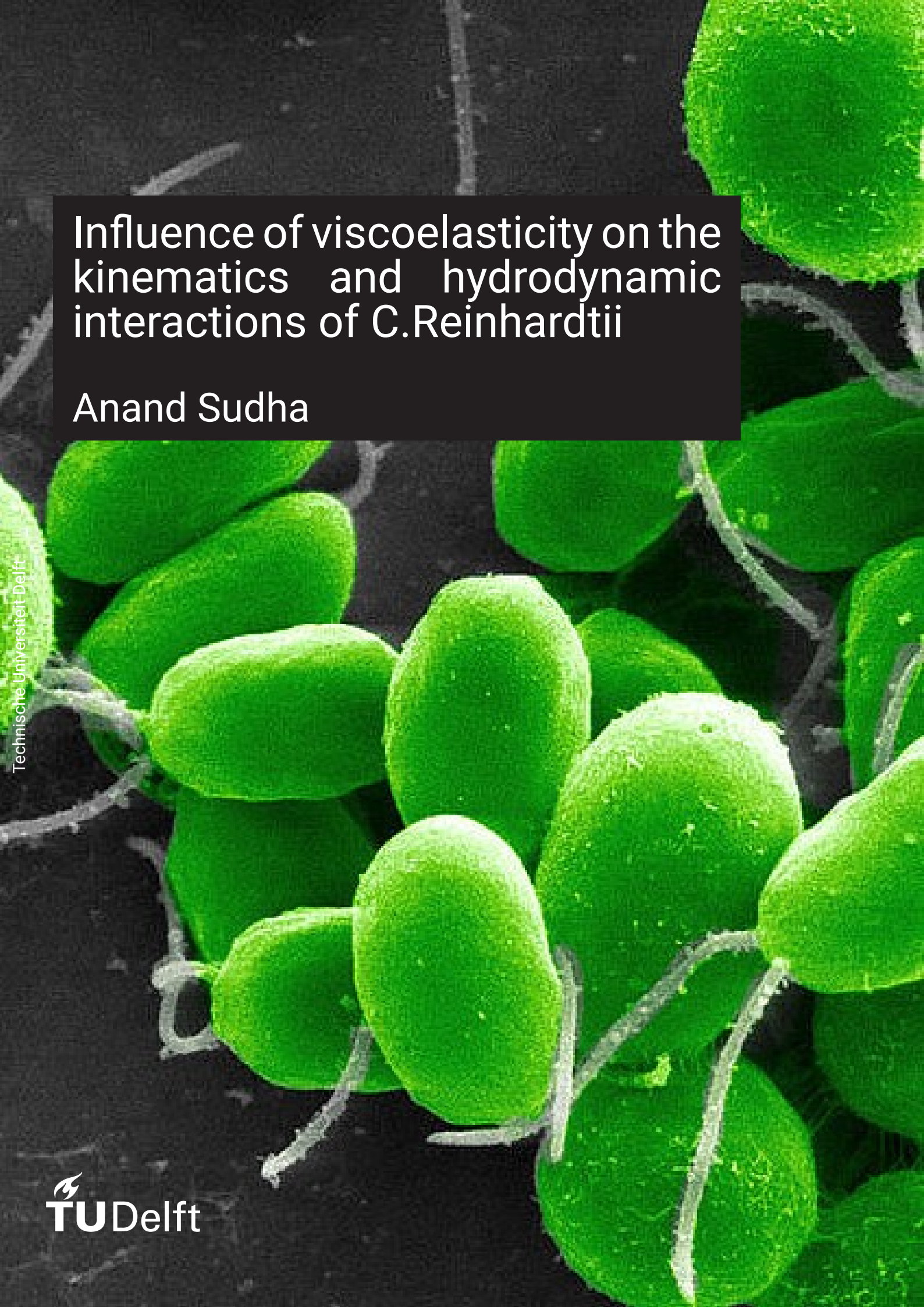

Technische Universiteit Delft

TU Delft

Influence of viscoelasticity on the kinematics and hydrodynamic interactions of C.Reinhardtii

by

Anand Sudha

to obtain the degree of Master of Science
at the Delft University of Technology,
to be defended on Friday, October 4, 2019 at 14:00 hours
P&E number 2992

Student number:	4741226	
Project duration:	January 6, 2019 – October 4th, 2019	
Thesis committee:	Dr. ir. W. P. Breugem,	TU Delft, chair
	Dr. D. Tam,	TU Delft, supervisor
	Dr. B. P. Tighe,	TU Delft
	Dr. P. E. Boukany,	TU Delft

TU Delft

Acknowledgments

9 months before, Microfluidics seemed daunting as I had no previous knowledge nor experience in the field. After the completion of my thesis, Microfluidics still does seem daunting, but that is completely masked by the enthusiasm I have for it. This thesis proved to be an excellent introduction into the meticulousness and vagaries of research, an experience that I enjoyed. This journey, however, would not be possible if it wasn't for the help of a few people. First, I would like to express my gratitude towards my family who have supported me emotionally, mentally and financially, without which I wouldn't have had such a smooth learning experience. I would like to use this space to also thank my friends for making me feel comfortable even in tough times. I am very grateful to Parviz Ghoddoosi Dehnavi for performing the relaxation experiments and to Da Wei for preparing the agar slants, despite having other commitments. I never hesitated to consult Junaid Mehmood and Koen Muller about the tracking code and experiments, and I would like to thank them for helping me when needed. Finally, I would like to express my heartfelt thanks to Dr.Daniel Tam and Dr.Abel-John Buchner for not only proposing the project but also for their invaluable guidance that ushered me through this thesis. The amiable atmosphere provided by them, along with their useful tips, gave me the confidence to explore new horizons and come up with new ideas while making me understand the requirements of good research.

Anand Sudha
Delft, October 2019

Abstract

Considering the abundance of viscoelastic fluids in nature, growing attention has been received for the study of microorganisms in viscoelastic fluids. In Newtonian fluids, the flow of microorganisms is governed by the viscosity alone. But in viscoelastic fluids, the addition of the elastic component complicates the situation. The flow of the organism is now dictated by a combination of the two forces- viscous and elastic. Understanding the behaviour of these organisms is not only important because of the presence of such environments in nature, but also because of the potential pharmaceutical applications that such studies might lead to.

This thesis focuses on the experimental study of the swimming of *Chlamydomonas reinhardtii*, a model motile swimmer that swims at low Reynolds numbers. *Chlamydomonas reinhardtii* is a single-celled green alga which has a body length of ~ 10 μm and two beating flagella to propel itself. At this small scale, microbes swim at low Reynolds number, $\mathcal{O}(10^{-3})$. The characteristics of the surrounding fluid could change the behaviour of the cells not only in terms of their swimming but also the possible interactions they could have with a surface. The main objective of the thesis is to characterize these differences in motility and hydrodynamic interactions of these cells in Newtonian and viscoelastic fluids of varying viscosities. This is accomplished by observing the motion of a dilute suspension of *Chlamydomonas reinhardtii* in 3D using four cameras. The cells are subsequently tracked using an in-house 3D particle tracking code that incorporates a recursive divide and conquer strategy to reconstruct the trajectories.

The experiments showed a drop in velocity in viscoelastic fluids as compared to its Newtonian counterparts, validating the results from existing literature. The cells also maintained their helical motion previously observed in TRIS, although with a drop in radius and pitch in viscoelastic fluids. The ratio of the radius to the pitch, however, remained constant for all the cases, indicating a tendency to retain its overall motion. The algae were found to swim with a dominant right-handed chirality in all the fluids regardless of the viscosity and viscoelasticity.

The study of cell-wall interactions is of prime importance because of the presence of confined surfaces encountered in nature. The concentration profile of the cells was observed to be similar in all the fluids, showing a non-uniform distribution with large concentration at the boundaries. Based on the distribution, cells that come within 100 μm within the wall are considered for wall interactions, with a distance of 20 μm defined as the contact region. The overall trajectories near the wall in TRIS revealed that the cells tend to arrive at steep angles in the contact region and leave at shallow angles, a phenomenon termed as asymmetric reflection. When the viscosity increased, however, this behaviour became less apparent as the incoming angles became less steep, while the outgoing angles remained shallow. For the viscoelastic case, the behaviour appears to become more symmetric with increase in viscoelasticity. Additionally, the data also points to a less steep drop in velocity in the contact region in solutions of higher viscosity as compared to the less viscous solutions. Though this might indicate a greater influence of hydrodynamics near the wall for more viscous fluids, more data is required to observe this behaviour deeply as the tracking efficiency appeared to have reduced in these cases, giving less data to work with.

The obtained results show a clear effect of viscoelasticity on the motility and kinematics of the cells, confirming results and predictions from existing literature. For cell wall interactions, differences are certainly discerned, not only for the viscoelastic cases but also for the more viscous cases. More data is required to draw substantial conclusions from these results. More experiments on these fluids are recommended to give a clear indication of the change in wall interactions in fluids of higher viscosity and viscoelasticity.

Anand Sudha
Delft, October 2019

Contents

List of Figures

List of Tables

1

Introduction

Considering the pervasiveness of microorganisms in water bodies, their motility in Newtonian flows have been extensively studied. But numerous cases of microorganisms in viscoelastic environments have been observed. The microbial biofilms formed by many bacteria such as *Escherichia Coli, Heliobacter Pylori, Pseudomonas aeruginosa* and *Bacillus Subtillus* are composed largely of a self exuded matrix that is viscoelastic in nature and these films provide the nutrients that allow these bacteria to grow on abiotic surfaces [1–4]. The growth of bacteria in bio-films alter their gene expression, leading to cause infectious diseases in humans and other animals [2]. The inhibitory potential of *C.Reinhardtii* in bacterial biofilms, especially in those of *Pseudomonas Aeruginosa*, makes the organism very important in the manufacture of pharmaceuticals against the infectious diseases caused by bacteria [5, 6]. *C.Reinhardtii*'s ability to mimic the compounds needed for biofilm formation and quorum sensing inhibits the growth of the bacterial biofilm. The transport of sperm in the cervical mucus also takes place in viscoelastic environments [7]. The pernicious biofouling caused by microorganisms in reactors, membranes and ships take place in the presence of viscoelastic bio-films [8–10]. Considering the possible application and understanding to be derived from the study of microorganisms in viscoelastic environments, it is imperative to conduct experiments in viscoelastic fluids to enhance our knowledge of these microorganisms.

These organisms generally move in fluids at low Reynolds number, $\mathrm{Re} = \rho LU/\mu << 1$, where ρ is the density of the fluid, L and U are the characteristic length and velocity scales and μ is the viscosity of the medium. In this regime, also called Stokes regime, the viscous damping effects far outweigh the inertial effects in case of Newtonian fluids. The fluid kinematics is reversible in this regime, so when cells swim in a reciprocal fashion, the net path is zero. By this, the organism moves for a particular distance along a path, then it retraces the same path to arrive at the starting point. This is the so-called 'scallop' theorem [11], and the organism must execute non-reversible, asymmetric strokes to break free from these constraints.

For microorganisms swimming in viscoelastic fluids, however, the 'Scallop' theorem is no longer valid [12]. This is because of the presence of a polymeric stress in addition to the viscous stress which leads to the introduction of a history effect in the fluid. The time scale corresponding to elastic stresses in a viscoelastic fluid is comparable to the viscous diffusion time scale of vorticity, and the interaction of these stresses leads to the breakdown of the kinematic reversibility. Even when the microorganism does not try to move, the polymeric stress causes the microorganism to slowly drift in the fluid. This implies that the microorganism has an additional problem to contend with in viscoelastic fluids, and this will probably affect the way they swim in these fluids, necessitating studies about their motion in viscoelastic fluids.

An important microorganism that has been extensively studied is *Chlamydomonas Reinhardtii*, and this organism is the focus of the thesis. *Chlamydomonas Reinhardtii* is a single-cell green alga with an ellipsoidal cell body of diameter around 10 μm [13]. A biflagellated unicellular organism with a flagella length of around 10 μm, *C.Reinhardtii* is widely distributed worldwide in soil and water. They are frequently used as a model organism in biology in a wide range of subfields, with focus especially on studying their cell motility [14]. Similar to other eukaryotic axonemes (the cytoskeletal structure which makes up the inner core of the appendages), the axoneme of *C.Reinhardtii* contained in the flagella consist of 9 double microtubules arranged around the perimeter and two central microtubules [15]. A local active bending force by the sliding of the microtubules relative to each other is caused by motor proteins connecting the neighbouring microtubules. This spreads the motor activity over the entire length of the eukaryotic flagellum.

C.Reinhardtii execute a cyclical breaststroke pattern with asymmetric configurations of power and recovery strokes at a beat frequency of ~ 50 Hz, propelling it forward at a mean speed ranging from 100-200 μm/s [16, 17]. The swimming motion of *C.Reinhardtii* resembles the human breaststroke- the flagella are pulled back in a nearly straight shape and are then bent over and pushed forward again. This motion is classified under the set of organisms called 'pullers'. Pushers, pullers and neutral swimmers represent the archetypal low Reynolds swimmers executing a particular motion to propel itself. Pushers [27] refer to the set of organisms whose propulsive force is generated behind the body, dragging the surrounding fluid in front of it. For pullers [27], on the contrary, the propulsive force is generated in front of the body, causing to drag the surrounding fluid behind it. The flow field generated by neutral swimmers are symmetric, unlike the other two categories.

The swimming direction of cells can be altered by certain environmental factors, a phenomenon called taxis [15]. The cells orient their direction according to the intensity of light (phototaxis), accumulating at moderate intensities and avoiding high intensities [15]. The presence of certain chemicals in the fluid causes the cells to get attracted to these chemicals (chemotaxis), with many of these chemattractants aiding their growth [15]. When left alone in the tube, the cells accumulate at the top of the tube, i.e, they orient opposite to the direction of gravity (negative gravitaxis) [15].

In order to understand the effect of viscoelasticity on microorganisms, their motility in Newtonian fluids need to be studied first to establish a suitable mode of comparison. The extensive documentation of the physics of microorganisms in Newtonian fluids has paved the way for studies in viscoelastic fluids. So this literature review will focus on the Newtonian studies first, and move on to the research in viscoelastic fluids later.

1.1. Literature review

1.1.1. Newtonian flows

The motility of microorganisms in Newtonian flows has been studied extensively, both experimentally and numerically. Many studies characterise the beating of flagella in Newtonian fluids, the most prominent being the experimental studies of the oscillatory flow field induced by *C.Reinhardtii* by Drescher *et al* [17] and Guasto *et al* [16]. Drescher observed the formation of side vortices close to the cells and flow in front of the body along the direction of motion towards the stagnation point. The formation of side vortices was also observed by Guasto. The paper further examined the strength of the vortices during the power and recovery strokes, noticing the time dependency of the instantaneous flow field generated by the cells.

Motility studies also involve the velocities and kinematics of the microorganisms. An impor-

tant paper characterising the kinematics was studied by Crenshaw *et al* [54]. Here, they observed that the organisms tend to execute helical trajectories. This was corroborated by Lee *et al* [18], who observed helical trajectories executed by *P.Minimum*. Muller [19] also observed this dominance of helical trajectories for *C.Reinhardtii* in his master's thesis, and applied the Frenet-Serret framework as described by Crenshaw *et al* to determine the radius and pitch of these helices. He achieved this by developing an algorithm to track the motion of the cells in 3D. Muller also observed that some cells tend to frequently reorient as they move, a result observed by Polin *et al* [20] as well. Polin *et al* noticed that this mechanism was similar to the 'run and tumble' motion of *E.Coli* [21], where the bacteria periodically reoriented its motion to explore the environment.

The hydrodynamic interactions of these microorganisms induced by the presence of a confined boundary is of great importance because of the proximity of these boundaries in nature. The biofouling caused by bacteria on surfaces [8–10] and the movement of the sperm within a confined reproductory tract [7] are some of the common examples of interactions with boundaries in nature. The presence of this boundary influences the swimming of these microorganisms, causing some of them to even exhibit different motions near a wall, such as the circling motion observed by Lauga *et al* for *E.Coli* [22] and the dancing motion observed by Drescher *et al* for *Volvox* [23]. The accumulation of swimmers near the wall was observed for organisms as diverse as *E.Coli* [24], *P.Minimum* [18] and bull spermatozoa [25].

To understand the hydrodynamic interactions of swimmers in Newtonian fluids in the presence of a boundary, Li and Ardekani [26] numerically studied the hydrodynamic interactions near a wall for neutral squirmers, pushers and pullers. The simulations observed that the swimmers tend to swim near the wall and stay there until a particular time governed by their orientation, mode of oscillation and swimming motion, followed by swimming away from the wall. When detached from the wall, pullers were found to either swim away from the wall, oscillate near the wall and eventually swim along it or swim in a cyclical motion based on the mode of oscillation.

The attraction of *E.Coli* towards the wall was explained by considering a force dipole near the wall by Berke *et al* [24] and this was verified experimentally. By using the same model, Berke proposed that a puller would orient itself perpendicular to the wall and would crash into it. He also observed the effect of far-field hydrodynamics theoretically on both pushers and pullers, with pullers experiencing a net attraction towards the wall when oriented towards it.

Hydrodynamic interactions are not the only forces that a cell experiences near a wall. Interactions among cells and contact with the wall are also possible. Qian *et al* [28] observed the emergence of hydrodynamic interactions numerically between different cells in addition to the wall interactions, leading to the development of phase locking between two cells that allows the cell to adjust its beat pattern in response to the nearby hydrodynamic forces. The synchrony arising due to motion of flagella from two different cells was also theoretically observed by Friedrich and Julicher [29] for a simple mirror-symmetric swimmer that propels by a revolving motion of spheres, but they concluded that the local hydrodynamic friction forces arising from the motion of the swimmer dominate the interactions with the boundary. Experiments conducted by Kantsler *et al* [30] also showed the dominance of direct contact ciliary interaction between cells over hydrodynamic interactions for *C.Reinhardtii* and mammalian sperm cells when it comes to the scattering of the cells near the wall. The scattering angle was found to increase with an increase in flagellar length. Kantsler *et al* observed that cells moved towards the wall at a steep angle and left at a shallow angle, implying a loss of memory of the incoming angle. The results from Muller [19], on the other hand, differed from these observations, with similar incoming and outgoing angles

being the more commonly observed phenomenon. This was classified under the phenomenon of 'symmetric reflection' by Muller. Contino *et al* [31] observed that a combination of hydrodynamic and flagellar contact interactions govern cell-wall interactions, with the incoming and outgoing angles being closer to Muller's results.

1.1.2. Viscoelastic flows

In the case of microorganisms swimming in viscoelastic environments, two other dimensionless numbers, the Deborah and Weissenberg numbers, in addition to the Reynolds number assume importance. The Deborah number is given by De = λ/T, where λ is the relaxation time of the viscoelastic fluid (the time taken for the polymer molecules in the fluid to get fully stretched after the application of stress) and T is the characteristic time for flow deformation. The Weissenberg number Wi = $\lambda U/L$ is defined as the ratio of elastic forces to viscous forces, with U and L being the characteristic velocity and length scales respectively [34]. Wi is used to characterise simple, steady viscoelastic flows and to determine the anisotropy of the forces, whereas De is used to characterise unsteady viscoelastic flows, determining when the stored elastic energy is released. De or Wi can be used interchangeably to describe the flow if one length scale is sufficient to determine the dynamics of the problem or if the multiple length scales can be related by a geometric scaling.

The effect of viscoelasticity on the swimming of microorganisms is not clearly understood and has therefore received growing attention. Many papers devoted to the subject have computed the flow fields generated by swimmers in viscoelastic fluids and their subsequent interactions with the fluid and the boundary numerically. Among these simulations, many focus on the kinematics and motility. Riley and Lauga [35] showed the enhanced swimming of Taylor's swimming sheet model [36] in a viscoelastic environment, with the speeds of the sheets being higher than the Newtonian case. Using the same waving sheet model, Lauga [37] observed that the transport and locomotion of the sheet could be adjusted by passively modulating the properties of the fluid without changing the gait of the organism. The effect of viscoelasticity on filaments was modelled by Fu and Powers [38], where they observed a decrease in swimming speed compared to Newtonian fluids and the possibility of reversing the filament direction due to changes in beating pattern caused by viscoelasticity.

Zhu *et al* [27] simulated the effects of viscoelasticity on neutral squirmers, pushers and pullers. They observed the generation of an axisymmetric vortex in front of the pusher and behind the puller. A decrease in velocity for all the swimmers was observed compared to the velocities in Newtonian fluids. In the case of pullers, the velocity ratio (Non-Newtonian to Newtonian) initially decreased with increasing Weissenberg number, after which the ratio was observed to stagnate. This decrease in velocity in a puller compared to a Newtonian fluid was caused by the action of the polymeric stress in conjunction with the axisymmetric vortex ring. For large Weissenberg numbers, the authors theorized that this observed stagnation might be related to the gait of the puller and the large relaxation time. By virtue of its gait, a puller causes the polymer to stretch behind it, thereby reducing the effects of elasticity. For fluids with long relaxation times, the elastic stress, though large, takes a longer time to achieve its maximum value. By the time this happens, the puller has already swum a considerable distance, thereby minimizing the effects of this elastic stress.

The presence of an elastic component might also change the interaction of the organisms with a boundary. The hydrodynamics of squirmers in viscoelastic fluids near a wall was assessed numerically by Li *et al* [39]. For a puller, they observed that the puller initially approaches the wall and stays there for some time until it reorients itself and escapes the wall. This residence time was found to be slightly longer than that in a Newtonian fluid. The cause for this was ascertained to be

the polymeric stress developed in the region between the puller and the wall, trapping the puller for some time until the polymeric stress diminishes due to the build-up of Newtonian torque in the opposite direction. Yazdi *et al* [40] further expanded on this subject by numerically studying the attraction of the squirmer to the wall. The puller was found to be attracted to the wall only at a particular region governed by its orientation and radius. The size of the attraction layer increased as the puller aligned itself towards the wall. Outside the attraction layer, the puller was observed to move away from the wall for almost all initial orientations, with the puller initially aligned perpendicular to the wall being the exception.

Ardekani and Gore [41], through simulations, observed that microswimmers drift towards a preferred orbit. The aggregation of these microorganisms was controlled by their motility and the viscoelasticity of the fluid, with the orbits (limit cycles) being either square or circular in shape based on the motility. Yazdi *et al* [42] numerically examined the swimming dynamics of squirmers near the wall in viscoelastic fluids, and they also observed the emergence of spiral limit cycles for pullers. The presence of a boundary was found to have a significant effect on the formation of limit cycles, subsequently affecting the cell-cell interactions, with the limit cycles being formed in a region around the boundary. This effect was attributed to the non-linearities caused by the polymeric stresses.

An additional behaviour to focus on would be the collective motion of a suspension of microorganisms. To see if viscoelasticity has any influence on the interactions among cells, the collective behaviour of microorganisms in viscoelastic fluids was studied numerically by Borzogi and Underhill [43] and, Li and Ardekani [44]. In both papers, the observation that a single microorganism causes long-ranged disturbances which moves and rotates other cells as it swims was noted. Fluid elasticity was observed by both papers to have a weaker effect on pullers compared to other swimmers.

The viscoelastic environments found in nature are largely shear-thinning [2, 7]. Some numerical papers extended the previous results for viscoelasticity to shear-thinning fluids. Nganguia *et al* [45] simulated the effect of a shear-thinning fluid on a three-dimensional ciliated model. They showed that the efficiency of swimming in a shear-thinning fluid is much larger than in a Newtonian fluid, but the swimming speed was reduced. The paper by Datt *et al* [46] also reported similar results when they simulated the motion of spherical squirmers in a shear-thinning fluid.

Experimental studies in viscoelastic fluids are slowly coming into prominence because of the growing need to understand the motility of microorganisms in viscoelastic fluids. One of the first few papers to experimentally investigate the effect of Non-Newtonian fluids on microorganisms was by Berg and Turner [47]. Their experiments were concerned with the motility of different bacteria, and they observed different behaviours when they compared with that in Newtonian fluids. The rotation rates and efficiencies of the organisms in Non-Newtonian fluids were reported to differ significantly. The paper by Keim *et al* [48] demonstrated the reciprocal motion and self-propulsion in a viscoelastic fluid theoretically proposed by Lauga [12] using artificial swimmers made with electromagnets, dimers and epoxy beads. Shen and Arratia [49] observed the hindering of self-propulsion of *Caenorhabditis Elegans* in a viscoelastic fluid, with the velocity decreasing with increasing elastic stresses. Gagnon *et al* [50] studied the motility of the same organism in a shear-thinning fluid. The velocity and beating (kinematics) of the nematode was observed to be similar to that in a Newtonian fluid, but the shear-thinning fluid modified the local velocity fields, increasing the circulation but decreasing the average velocity in the fluid. Experiments on flexible microswimmers consisting of a magnetic head actuated by a frequency-controlled magnetic field

were performed by Espinosa-Garcia *et al* [51]. The viscoelasticity in the fluid was found to enhance self-propulsion, thereby increasing the propulsive speed of the swimmer.

The motility of *C.Reinhardtii* in a viscoelastic fluid was studied experimentally by Qin *et al* [52]. The viscoelastic fluids were prepared by adding varying concentrations of Polyacrylamide (PAA) to water. The nature of the fluid was found to strongly influence the movement of the flagella, with the flagella observed to being more motile in the Newtonian fluid. In a viscoelastic fluid, however, lateral displacements of a portion of the flagellum close to the cell body appeared to be severely restricted, with localized bending at the distal tip at the initial stage of the power stroke. The beating frequency was similar to that in a Newtonian fluid for low viscosities and increased for higher viscosities. On the other hand, the swimming speed was observed to be much lower than the Newtonian case, especially at higher viscosities. The speed at the power stroke was comparable to the Newtonian value, but the speed at the recovery stroke was found to be larger than the Newtonian value and increased with viscosity. This has a net effect of reducing the speed of the cells, with the authors theorizing that the reduced speed is due to the polymeric stresses aiding the recovery stroke and hindering the power stroke.

To better understand the phenomenon, the authors [53] followed this up with a numerical paper. They observed the elastic memory effect as reported by Lauga [12], with lower elastic stresses on the power stroke and higher on the return stroke. The fluid elasticity was observed to enhance the speeds of both the power and return strokes, and this was found to increase with higher Deborah numbers. The authors suggested that the presence of fluid elasticity might make it difficult for *C.Reinhardtii* to maintain a fixed stroke due to the larger power required, leading it to change its stroke based on the local fluid properties. Though this modification in gait reduced the speed, it improved the efficiency at which the cells swim. The speeds reduced because the fluid elasticity was found to aid the return stroke more than the power stroke.

1.2. Motivation

Although some experimental studies have been conducted in viscoelastic fluids, studies which observe the motion in 3-D aren't common. Most microorganisms including *C.Reinhardtii* and bacteria execute a 3D helical motion [54, 55], and the neglect of this 3rd dimension might hinder a proper understanding of their motility. Few papers have experimentally observed the helical trajectories of bacteria and other microorganisms in 3D [18, 55], but their trajectories in viscoelastic fluids haven't been well-documented, with the existing studies focussing more on the velocities, flow fields or the effect of the fluid on the flagellar motion. The possible difference, or the lack of it, in the trajectories in Newtonian and viscoelastic fluids could provide additional understanding on the effect of viscoelasticity on the microorganisms, allowing us to observe the possible adjustments a microorganism might make with respect to the nature of the fluid.

While certain numerical studies have observed the effect of confined boundaries [39, 40] on microorganisms, experiments on cell-wall interactions in viscoelastic fluids are lacking. Considering the presence of confined environments in which the microorganisms flow [7] and the applications in biofouling [8–10], and biotechnology [56], it is important to understand how cell-wall interactions change with the change in the properties of the fluid, especially as these interactions predominantly take place in viscoelastic environments. The thesis by Muller [19] provides useful insights into the trajectories, cell-wall and cell-cell interactions of *C.Reinhardtii* in Tri-Sodium Phosphate (TRIS) medium, and this thesis hopes to provide similar insights on the influence of viscoelasticity and viscosity on the swimming and wall interactions of the microorganisms. Based on the existing literature and the possibilities of our experimental technique, the thesis

seeks to answer the following questions:

1. Does viscoelasticity have any effect on the velocities of the cells as shown by the experiments of Qin *et al* [52]?

2. Is the gait change observed by Qin *et al* [52] in viscoelastic fluids have any effect on the helical motion of the cells observed by Crenshaw *et al* [54] and Muller [19] in TRIS?

3. How does the presence of the boundary influence the cell behaviour and how does viscoelasticity (or viscosity) govern these interactions?

4. Are the cell-wall interactions primarily due to flagellar contact with the wall, as observed by Kanstler *et al* [30], or due to primarily hydrodynamic interactions, as assumed by the simulations of Li *et al* [39] and Yazdi *et al* [40] , or due to a combination of both , as observed by Contino *et al* [31] ? How does the fluid rheology change the nature of these interactions?

5. How does the far-field hydrodynamics influence the swimming of the cells? Is it similar to the results theoretically proposed by Berke *et al* [24] in TRIS? How does the fluid rheology affect the far-field hydrodynamics?

1.3. Structure of the report

The first chapter of the report gives an overview of the existing literature on the kinematics and hydrodynamics of microorganisms in Newtonian and viscoelastic fluids, followed by an establishment of the research questions based on the literature. A brief understanding of viscoelastic fluids is provided in the second chapter along with a brief description of the techniques used to measure the relaxation time. The third chapter deals with the experimental methodologies used in this thesis to characterise the rheology and track the cells. All the obtained results are shown in the fourth chapter, with the fifth chapter aiming to contextualize and understand these results in terms of the existing literature. Finally, all the results are summarized in the sixth chapter and some suggestions are given for future experiments.

2

Viscoelastic fluids

Based on the dependence of the applied shear stress on a fluid with the change in strain rate, the viscosity of the fluid can be characterised as having a linear, non-linear or plastic response. When a fluid exhibits a linear response to strain rate, it is considered to be a Newtonian fluid. The ratio of stress to rate of strain at a given temperature is constant, with the constant being the viscosity. The law describing this relation is called Newton's law of viscosity. The viscosity of a fluid is defined as it's resistance to deformation at a given rate. Any fluid that exhibits a non-linear response is termed as Non-Newtonian. The viscosity in a Non-Newtonian fluid varies with strain rate unlike that in a Newtonian fluid.

From the above paragraph, Non-Newtonian fluids can be generally defined as any fluid where a constant viscosity cannot be defined. Although the viscosity of most Non-Newtonian fluids depends on the shear rate or shear rate history, fluids with shear independent viscosities aren't uncommon. The definition of non-Newtonian fluids in terms of viscosity is thus inadequate for certain cases. The properties of Non-Newtonian fluids are better understood using tensor valued constitutive equations. Therefore, the term Non-Newtonian is an all-encompassing term for any fluid that does not obey the following equation [57]:

$$\mathbf{T} = -P\mathbf{I} + 2\eta\mathbf{D} \tag{2.1}$$

where $\mathbf{T}$ is the stress rate tensor,P is the pressure term, η is the viscosity and $\mathbf{D}$ is the strain rate tensor.

Non-Newtonian fluids can be classified based on the variables influencing viscosity and its subsequent variation, the behaviour exhibited by the fluids under stress and by their constitutive equations. Fluids for which the viscosity depends on the applied stress can be classified as either shear thickening (dilatant) or shear-thinning (pseudoplastic). The viscosity of a shear-thickening fluid increases with an increase in shear rate (eg: oobleck) whereas the viscosity of a shear-thinning fluid decreases with an increase in shear rate (eg: ketchup, whipped cream, etc.). There are also fluids whose strain rate is a function of time. Fluids that require a gradually increasing shear stress to maintain a constant strain rate are referred to as rheopectic (eg: printer ink). In these fluids, the viscosity increases with an increase in the duration of the shear force. Conversely, a thixotropic fluid (eg: Yoghurt) is a fluid that thins out with time and requires a decreasing stress to maintain a constant strain rate, i.e, the viscosity decreases with a longer duration of the shearing force. As stated before, the variation of viscosity isn't a necessary condition for a fluid to be Non-Newtonian. Certain fluids display a linear stress-strain relationship but require a certain yield stress to flow.

These fluids are called Bingham plastics (eg: mayonnaise). Figure 2.1 depicts the shear stress-shear rate relationship for these different types of Non-Newtonian fluids.

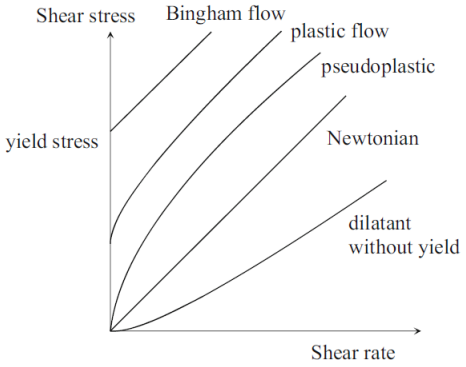

Figure 2.1: Different types of Non-Newtonian behaviour

2.1. Properties of viscoelastic fluids

Viscoelastic fluids are Non-Newtonian fluids that exhibit both viscous and elastic characteristics when undergoing deformation. While viscous materials resist shear flow, elastic materials strain when stretched and immediately return to their original state once the strain is removed, as long as the applied stress does not exceed the yield stress. Viscoelastic fluids possess properties of both viscous and elastic materials. They are generally shear-thinning in nature, though that's not always the case. Examples of viscoelastic fluids include some lubricants, whipped cream and many polymeric fluids.

Purely elastic materials do not dissipate heat after the removal of an applied load, but a viscous fluid dissipates the energy almost instantaneously as viscous fluids are resistant to deformation [58]. Viscoelastic materials display a behaviour that is intermediate of the two, with the materials losing some energy on the application of shear stress. The amount of energy lost is governed by the extent of elasticity, with viscoelastic solids losing less energy than viscoelastic fluids. Therefore, hysteresis is observed for viscoelastic fluids in the stress-strain curve as shown in Figure 2.2.

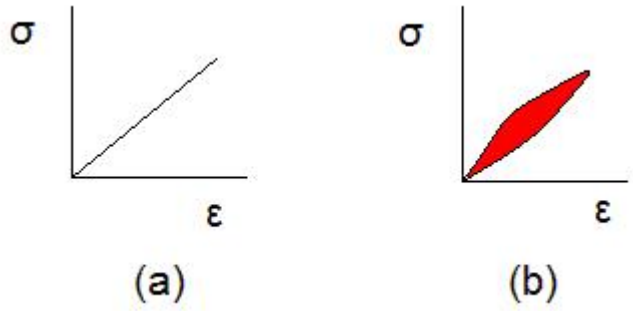

Figure 2.2: Hysteresis in viscoelastic fluids [58]

In addition to hysteresis, viscoelastic fluids also display creep and stress relaxation [59]. The application of a constant shear stress leads to a linear increase in strain for a Newtonian fluid in such a way that the ratio of the shear stress to the strain is a constant (viscosity). Once this stress is

removed, the strain is not recovered and is still applied on the fluid. For a purely elastic solid, the strain increases instantly and remains constant until the stress is removed, after which the strain is completely recovered. For a viscoelastic material, the strain shows a delayed response to stress and increases non-linearly. Once this stress is removed, the recovery is not instantaneous as in an elastic solid, but gradual. The recovery is faster for a viscoelastic solid as compared to a fluid, with even full recovery of strain over long times being possible in a viscoelastic solid. This creep phenomenon is depicted in Figure 2.3a .

When a constant strain is applied to the material, the shear stress immediately rises for a Newtonian fluid and is almost instantly dissipated after that. Thus, an immediate and complete stress relaxation occurs. The shear stress instantly increases and remains constant for a Hookean solid until the strain is removed. The stress is not dissipated in this case and is responsible for stretching the material. A viscoelastic material shows a non-linear delay in stress relaxation as a function of their viscoelastic properties. Complete stress relaxation is only possible for a viscoelastic fluid over prolonged observation but with viscoelastic solids, only partial relaxation is possible. This is illustrated in Figure 2.3b. From these phenomena, it is evident that viscoelastic materials exhibit properties intermediate to viscous and elastic materials.

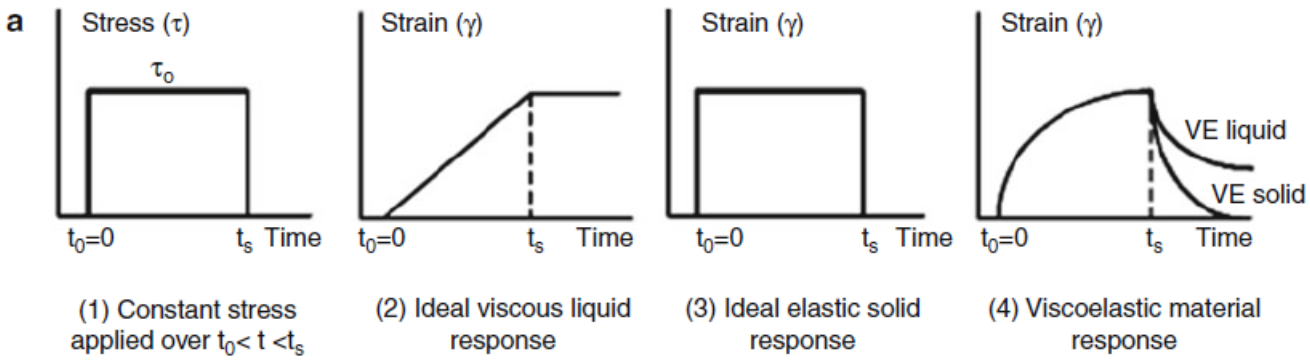

(a) Creep and recovery tests [59]

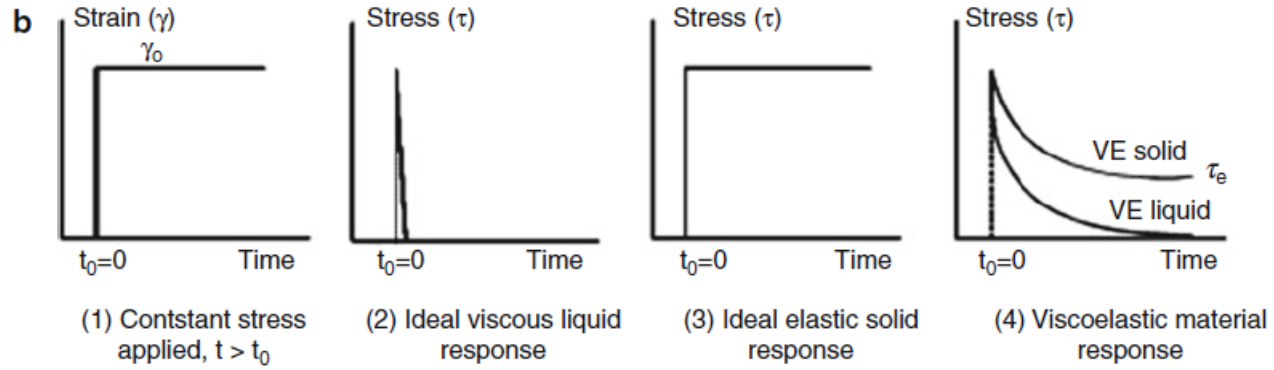

(b) Stress relaxation tests [59]

Figure 2.3: Graphs illustrating creep and stress relaxation

2.2. Relaxation time

An important parameter to consider while studying elasticity is the relaxation time, which is a measure of how the molecules respond to stress [60]. The relaxation time of a polymer is the time it takes for the polymer molecules to fully stretch after the application of stress. It can also be defined as the time required for the polymer molecules to return to its equilibrium configuration after the removal of the stress. The introduction of the elastic component in a fluid leads to the inclusion of two additional dimensionless numbers- the Deborah and Weissenberg numbers. Both these numbers are already discussed in section 1.1.2.

2.3. Methods of measuring relaxation time

Generally, polymers and viscoelastic fluids do not possess a single relaxation time but a spectrum of times [60]. In order to characterise a material's elasticity, a single relaxation time measured in the linear viscoelastic region is considered to be the value representative of a material's elasticity. For a viscoelastic material, internal stresses depend on the instantaneous deformation as well as the history of deformation [61]. The material is said to be in the linear viscoelastic region if the deformation applied is small enough so that its rheological properties do not depend on the value of the deformation. As shown in Figure 2.4, the log of the viscous and elastic moduli remain constant until a strain of γ_L is reached, after which both moduli decrease with the log of the strain. A higher elastic modulus compared to the viscous modulus in the linear viscoelastic region implies a viscoelastic solid, while the converse is true for a viscoelastic fluid. Two methods are commonly used to measure the relaxation time in this linear viscoelastic region.

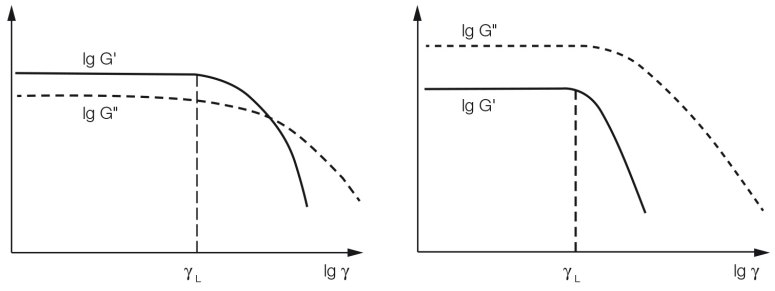

Figure 2.4: Variation of moduli with the strain to determine the linear viscoelastic region. The left graph shows a viscoelastic solid and the right shows a viscoelastic fluid.

2.3.1. Stress relaxation

The principle behind stress relaxation is the same as described in 2.1. The equation describing the shear rate when such a procedure is used is given by [60]:

$$\frac{\dot{\sigma}}{G} + \frac{\sigma}{\eta} = \dot{\gamma} \tag{2.2}$$

where σ is the shear stress, G is the relaxation modulus, η is the fluid viscosity and γ is the strain. The relaxation modulus is a measure of the material's resistance to applied shear. The solution of this equation is given by:

$$\sigma = \sigma_0 e^{-\frac{t}{\lambda}} \tag{2.3}$$

where $\lambda = \frac{\eta}{G}$ is the relaxation time and σ_0 is the stress applied at time $t = 0$. The relaxation time can be thus obtained from this equation after conducting the experiment. Since the relaxation time is measured in the linear viscoelastic region, the strain applied has to be within the limits of linear viscoelastic behaviour.

2.3.2. Small Amplitude Oscillatory Shear (SAOS)

This is the most common method of measuring relaxation time and it is carried out over a range of frequencies. A small sinusoidal strain is applied to the material. The strain is given by [61]:

$$\gamma = \gamma_0 \sin(\omega t) \tag{2.4}$$

where γ_0 is the strain amplitude and ω is the frequency. The corresponding shear stress is given by:

$$\sigma = \sigma_0 \sin(\omega t + \delta) \tag{2.5}$$

where δ is the phase shift or the loss angle. A perfectly viscous material responds 90° out of phase to the applied strain as the stress is proportional to the strain rate in a viscous fluid rather than the strain. Since a viscoelastic fluid consists of both viscous and elastic components, an in-phase and out of phase behaviour is observed. Similarly, the relaxation modulus can also be split into two components. The in-phase component is called the storage modulus, representing the elastic component, whereas the out of phase component is called the loss modulus, representing the viscous component.

$$G'(\omega) = \frac{\text{in} - \text{phase strain}}{\text{maximum strain}} \quad G''(\omega) = \frac{\text{out of phase strain}}{\text{maximum strain}} \tag{2.6}$$

From the definition of relaxation from 2.3.1, we can also calculate an in-phase and out of phase viscosity. This can be combined and written as a complex viscosity.

$$\eta = \eta'(\omega) - i\eta''(\omega) \tag{2.7}$$

The frequency at which the strain is applied is varied and the corresponding values of the elastic and storage moduli are plotted as shown in Figure 2.5. The intersection of the two curves gives the relaxation frequency, the inverse of which is the relaxation time. After the relaxation time is reached, viscous effects begin to dominate. This figure serves as a perfect illustration as to why larger relaxation times correspond to larger elasticities.

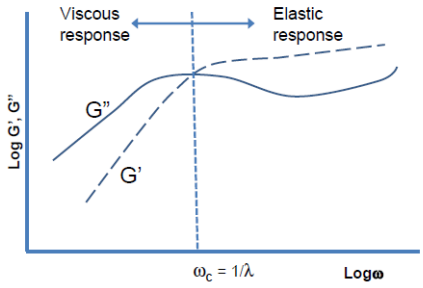

Figure 2.5: Determination of relaxation time from Small Amplitude Oscillatory Shear (SAOS) method [61]

3

Experimental methodology

The idea is to track the organisms simultaneously in 3D and to observe the trajectories of these tracks for the different fluids. This chapter seeks to define the methodologies employed to achieve this aim. To simplify and aid understanding, the chapter is divided into 6 sections according to the methodology employed. The first section concerns itself about the choice of viscoelastic solutions and the subsequent rheology performed on these solutions. The method employed to determine the relaxation time of these solutions is detailed in the second section. The experimental procedure used to culture and observe the motion of *C.Reinhardtii* is described in the third section. The fourth and fifth sections deals with the image processing and the 3D-particle tracking algorithm employed to track the cells. The final section details the techniques used in post-processing.

3.1. Rheometry

Many aqueous polymer solutions have been employed as viscoelastic fluids to study the motion of microorganisms. The commonly used polymers among these are PolyAcrylamide (PAA) [52], Carboxy-methylcellulose (CMC) [50], Xanthan Gum [49], and Polyvinypyrrolidone (PVP) [62]. All of these solutions are viscoelastic and shear thinning as these are the common properties of the fluids found in nature and bacterial biofilms [4]. CMC solutions were observed to be viscoelastic only at concentrations above 1000ppm [49, 63] and at these concentrations, the solutions were very viscous. A similar viscoelastic behaviour was observed for Xanthan Gum as well [64], with the solutions being very viscous. Since the results from Qin *et al* [52] reported low net velocities at viscosities in the range of 10-100 mPas, it would be better to study the motility of *C.Reinhardtii* in viscoelastic fluids that display good elastic behaviour at lower viscosities. Although PVP solutions are viscoelastic at lower viscosities, the degree of shear-thinning is a lot lower compared to the PAA solutions [65]. Considering the already established results and the favourable viscoelastic properties of PAA solutions, it can be concluded that PAA solutions are the most favourable medium to study the motility of *C.Reinhardtii* in viscoelastic fluids. In our case, a cationic variant of PAA, PolyAcrylamide-Sodium Acrylate (PASA, MW = 18×10^6 g) was used as the polymer.

Different concentrations of PASA were added to Tri-Sodium Phosphate (TRIS) medium to prepare viscoelastic solutions. The properties of TRIS medium are similar to that of water, except that it contains nutrients required for the growth of *C.Reinhardtii*. Since it is important to maintain a sterile environment for the organism, the properties of Polyacrylamide (PAA) under thermal stress need to be known before starting the experiment. An extensive survey was conducted on PAA by Kulicke *et al* [66]. The viscosity was observed to be very sensitive to changes in temperature, with sustained heating for long duration leading to a drop in viscosity caused by the molecular

degradation of polymers. Large concentrations of PAA in aqueous solutions were observed to show a time degradation in viscosity.

The above effects reported by Kulicke *et al* [66] were observed only for sustained heating and large concentrations of polymer. The solutions need to be autoclaved before performing the actual experiments with *C.Reinhardtii* to avoid any bacterial growth that could contaminate the medium, hence affecting the motion of the cells or killing them. The solutions were prepared by adding the requisite amount of polymer to 50 mL of TRIS, followed by stirring them evenly using a magnetic stirrer. To test the effect of heating for short periods and time, solutions containing 1000 parts per million (ppm) of PASA in TRIS were autoclaved (Tuttnauer 2540 ML) at 120° C and 2 bar for 20 minutes.
The viscosities of these solutions were measured using the Contraves Low Shear-40 (LS-40) rheometer (Figure 3.1) with a Couette geometry at 20° C. In order to check the accuracy and the repeatability of the rheometer, distilled water samples of known viscosity were first measured at different periods. A Couette geometry was employed, with 5 mL of solution placed in the cup. A measuring bob of appropriate dimension is lowered into the cup. The bob is made to rotate in this cup and the shear rates are varied. The variation of the shear rates is used to determine the applied shear stress, and subsequently the viscosity of the solution.
The value of the viscosity for distilled water was within 10 % of the true value and the results are plotted in the Appendix A. Once the accuracy was established, the rheometer was used to determine the rheologies of the prepared solutions. The shear rates were varied from 1-100 /s for the 1000ppm PASA sample and the corresponding viscosities were measured. The sample was observed to be shear thinning and the results are plotted in Figure 3.2. Autoclaving was observed to have no effect on viscosity and the time degradation of viscosity wasn't observed either. Since this is the viscoelastic fluid with maximum polymer concentration, it was concluded that all the solutions could be safely autoclaved and used at a later time.

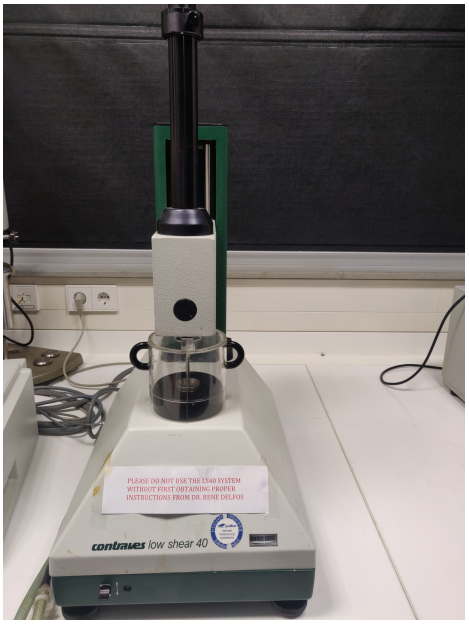

Figure 3.1: Contraves LS-40 Rheometer

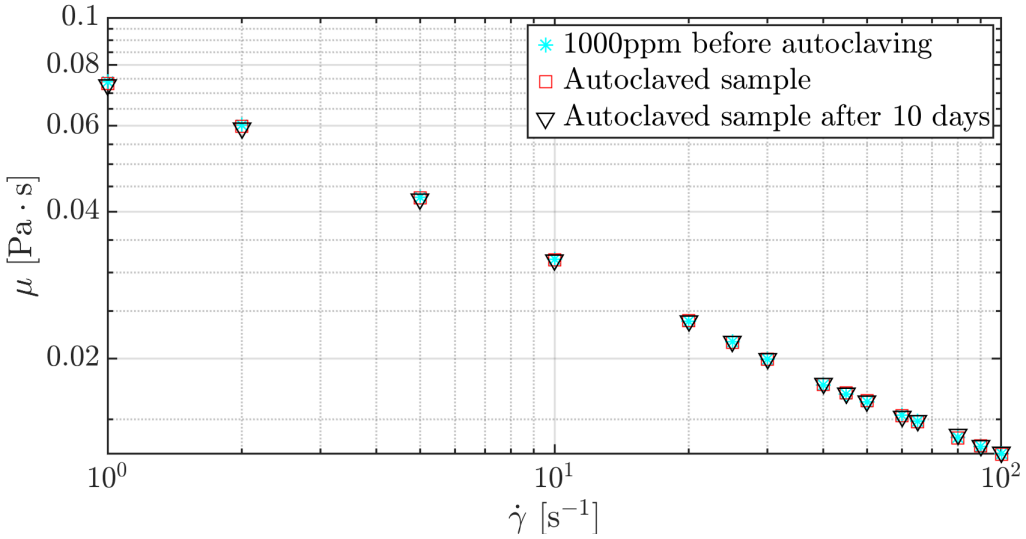

Figure 3.2: Variation of the viscosity with the shear rate for a 1000 ppm PASA sample. The blue asterisks represent the viscosities of the solution before autoclaving, the red squares the autoclaved sample and the black triangles represent the autoclaved sample after ten days. Autoclaving was found to have no effect on the viscosity.

3.2. Measurement of relaxation time

The Small Amplitude Oscillatory Shear (SAOS) method described in section 2.3.2 is utilized to measure the relaxation times of the viscoelastic fluids. The first measurements of relaxation times were carried out in the AR-G2 rheometer located in the Applied Sciences department of TU Delft. The procedure used involves SAOS measurements, similar to the procedure described in section 2.3.2. In the case of viscoelastic fluids with low relaxation times, macro-rheology or commercial rheometers cannot be used as most cannot measure small relaxation times because of their compliance limits. The difficulties involved in determining a clear relaxation time from the rheometer are elucidated in Appendix B. Naturally, a different methodology has to be used.

For fluids with low relaxation times, microrheology can be used to analyse the rheological properties of the fluid on a microscopic scale [67]. Most of these methods involve microscopic particles embedded in the solution whose thermal fluctuations in the solution (passive microrheology) or response to applied forces (active microrheology) are detected to determine the rheology of the solution [67, 68]. Among these techniques, optical traps are commonly used to perform experiments in both passive and active microrheology [67–69]. An optical trap is formed by applying a tightly focussed LASER using an objective of high Numerical Aperture (NA). This can be used to 'trap' small particles or beads by experiencing a force due to the scattering of photons [70]. The trap corresponds to an elastic spring, with the 'stiffness' related to the power of the laser. The oscillations of the particles within the trap can provide useful information about the rheological properties of the fluid [68, 69].

In this case, passive microrheology was used to record the thermal fluctuations of 5 μm sized beads embedded in the viscoelastic fluid. Only two viscoelastic fluids, 150 and 250 ppm PASA solutions, were studied for reasons relating to time and those explained in section 4.3. These experiments were conducted by Parviz Ghoddoosi Dehnavi on the optical trap setup in the Applied Sciences Department of TU Delft. The optical trap setup is similar to the one used by Wei *et al* [71] and Lang *et al* [72]. The working of this setup is shown in Figure 3.3. In essence, the setup is an

inverted microscope with modifications to accommodate two lasers and for mechanical stability. The trapping laser's effectiveness is enhanced using Acousto-Optic Deflectors (AOD) that provide dynamic position control [70]. The position of the bead is detected using a position detection laser coupled to a piezo-electric stage. The signal from the piezo stage is transmitted to a Quantum Photodiode (QPD), whose output is in Volts. Lenses are used for beam steering and separation.

To convert the information in volts from the QPD to obtain the position of the beam, a calibration procedure similar to those described by Addas *et al* [68] and Berg-Sørensen *et al* [73] is used. The experiments are conducted from frequencies ranging from 0.5-200 Hz with a trap stiffness of 7.62 pN/μm. Using the results from the AR-G2 rheometer on 100 ppm PASA (Appendix B), it is apparent that the strain is within the linear viscoelastic region. Additionally, passive microrheology ensures that large strains aren't applied [68].

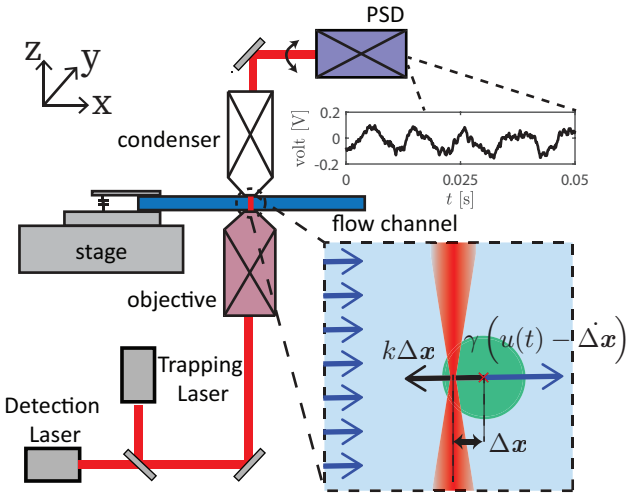

Figure 3.3: Setup used for the optical trap experiments

The viscous and elastic moduli, and hence the relaxation time, are determined from the thermal fluctuations of the bead. The experiments are carried out at frequencies ranging from 0.1 to 200 Hz. Since the viscous and elastic moduli are dependent on frequency, a relation between the thermal fluctuations of the bead and the moduli can be easily established using the fluctuation-dissipation theorem [68]. The complex particle response function in the frequency (f) space, $\alpha(f)$, relates to the Fourier transform ($x(f)$) of the bead displacement $x(t)$ as a function of time and the Fourier transform ($F(f)$) of the applied force on the bead ($F(t)$). The bead displacement is the displacement along the x-axis as shown in Figure 3.3. The relation is similar to the equation relating the applied force with the displacement for a Hookean solid. The particle response function, in essence, is similar to the spring constant. The following equations are all from the paper by Addas *et al* [68], which bases its equation from the paper of Schnurr *et al* [74].

$$F(f) = \alpha(f)x(f), \quad \alpha(f) = \alpha'(f) + i\alpha"(f) \tag{3.1}$$

The imaginary part of the response function is related to the Power Spectral Density(PSD) by the fluctuation dissipation theorem. The PSD is the measure of the signal's power content, i.e, the distribution of the power into frequency components comprising the signal.

$$\alpha"(f) = \frac{\pi}{2k_b T} f S(f) \tag{3.2}$$

where $S(f)$ is the PSD, k_b is the Boltzmann constant and T is the solution temperature, which in our case is 22° C. The real part of the response function is given by the Kramers-Kronig relation [68], provided that the imaginary part is known over a large frequency range.

$$\alpha'(f) = 4\int_0^\infty \mathrm{d}t\cos(2\pi f t)\int_0^\infty \mathrm{d}\xi\,\alpha"(\xi)\sin(2\pi\xi t) \tag{3.3}$$

Here, ξ represents the range of frequencies from 0 to ∞, and f is the frequency value for which $\alpha'(f)$ is desired [74]. The complex shear modulus is determined from the complex response function using the Generalized Stokes-Einstein Relation (GSER) [68]:

$$G(f) = \frac{1}{6\pi a\alpha(f)} \quad , G(f) = G'(f) + iG"(f) \tag{3.4}$$

where $G'(f)$ and $G"(f)$ are the elastic and viscous moduli respectively, and a is the radius of the bead.

Since the trap has a stiffness κ of its own, it introduces an apparent elastic modulus that changes the value of the response function [68]. To account for this, a correction is applied to the response function and subsequently, the elastic modulus.

$$\alpha_{\text{true}} = \frac{\alpha_{\text{measured}}}{1-\kappa\alpha_{\text{measured}}} \tag{3.5}$$

which upon inversion from equation 3.4 gives the corrected elastic modulus:

$$G'_{\text{true}} = G'_{\text{measured}} - \frac{\kappa}{6\pi a} \tag{3.6}$$

The trap stiffness is calculated using the equation, $\kappa = 2\pi\gamma f_c$, where f_c is the corner frequency and $\gamma = 6\pi\eta a$ is the Stokes drag on the bead [68] (η is the complex viscosity). The corner frequency is the frequency after which the energy flowing through the system is attenuated or, in other words, the frequency after which the PSD drops from a constant value [73]. The elastic and viscous moduli are subsequently determined for each frequency to determine the relaxation time.

3.3. Experiment

This section is concerned with the procedures and setup used to simultaneously track the motion of the cells in 3D to study their trajectories and understand their behaviour. Such experiments could reveal useful information about the effect of viscoelasticity and viscosity on the kinematics of cell motion and cell-wall interactions. The experimental setup adopted is similar to that used by Kim *et al* [75, 76]. Both these papers compared the effectiveness of two flow measurement techniques, 3D Particle Tracking Velocimetry (3D-PTV) and Tomographic Particle Image Velocimetry (Tomo-PIV), in micro-flows. Tomo-PIV is not used to study the flow fields created by the motions of the cells as tracer particles cannot be used because they disturb the motions of the cells [77].

To track the motion of the algae as active moving particles, a Lagrangian Particle Tracking (LPT) code implemented in MATLAB by Muller [19] in his master's thesis is used instead of the existing algorithm present in the commercial software, DaVis.

3.3.1. Flow chambers and cell cultures

The experiments were conducted on a wild type strain of *C.Reinhardtii* (cc-125). An agar slant consisting of colonies of *C.Reinhardtii* is prepared by Da Wei and John Buchner in TNW, TU Delft.

The liquid cell cultures are inoculated from the slant. The cells are cultured, inoculated and counted according to well-established procedures discussed by Quaranta *et al* [78]. The cells are allowed to grow for four days in TRIS medium before they are harvested. To suspend the cells in the desired viscoelastic or Newtonian fluid, the solution consisting of the cells in TRIS medium is centrifuged. The cells are then resuspended in the desired fluid.

In order to house the cells and the fluid to view their motion, acrylic flow chambers (Figure 3.4)) with dimensions 60 × 25 mm are laser-cut from a 1.5 mm thick acrylic sheet. An 8 mm diameter hole is cut at the centre of the flow chamber to house the cells and fluid. The bottom surface of the chamber is sealed by glueing a 0.1 mm thick Danzig Deckglazer glass side of dimensions 24 × 32 mm. The top surface is sealed with the same glass slides after the cells are injected into the flow chamber.

Considering the sensitivity of the cells to environmental conditions and their tendency to stick to surfaces, it is imperative to prepare the flow chambers and glass slides to prevent adhesion and ensure cleanliness. The flow chambers are washed alternatively with ethanol and distilled water (DI water) five times and are then dried. For the glass slides, however, the preparation is more elaborate as they form the walls which contact the cells. The glass slides are cleaned in a sonic bath for 25 minutes by placing them in a surfactant solution consisting of Hellmanex III detergent (0.5 % volume) and distilled water. They are washed with distilled water five times followed by another 25 minutes in the sonic bath in DI water. The glass slides are then dried.

While this procedure cleans the slides, the adherence of the cells to the slides have to be minimized. The first step in this process is to charge the slides by oxygen plasma for 30 seconds. The charged slides are then immersed in a 100 mL protein solution consisting of 1 mg Bovine Serum Albumin (BSA) (Aldrich A7906-50G) and 1 mg of Phosphate Buffered Saline (PBS) for 30-45 minutes based on the saturation of the contact line [79] to minimize cells adhering to the surface. After rinsing with DI water and drying with pressurized air, the slides are glued to the bottom surface of the chamber by Ultraviolet (UV) curing for two minutes using Norland Optical Adhesive 81.

Figure 3.4: Flow chamber

Before conducting experiments, the cells are counted under a microscope using a counting grid. The cells are then diluted according to the concentration desired. The cells are injected into the chamber using a micro-pipette. To avoid deflagellation of the cells, the tip of the micro-pipette is cut a little bit to make it wider. Nail polish is added to the sides of the top surface away from the hole to allow the glass slide to adhere to the top surface. The glass slide is gently placed on the top surface with careful attention to prevent the formation of any bubbles that could provide some background flow. Capillary action allows the fluid to spread over the glass slide.

3.3.2. Experimental setup

The experimental setup is shown in Figure 3.5a. It consists of four scientific Complementary Metal Oxide Semiconductor (sCMOS) cameras (LaVision Imager Pro M) and a large objective lens. A micron precision xyz stage (Figure 3.5a) is mounted on top of the setup to perfectly position the flow chamber in the field of view. The stage can be moved with the help of three precision micrometers on the stage. To simultaneously trigger the cameras, a portable timing unit is used and the timing and acquisition is controlled by the DaVis 8.2.1 software.

The setup is illuminated by a red LED panel located above the flow chamber as shown in Figure 3.5a. The forward scattered light by the algae passes through a large objective lens with a magnification of 1.5. The objective combines the optical paths of all the cameras and causes them to converge at one point. To increase the depth of field, the light rays are allowed to pass through a pinhole card with pinholes of diameter 2 mm before it enters the objective. Using this arrangement, the depth of field is increased to 2 mm by decreasing the original pinhole diameter [75], which is consistently observed in most experiments at this scale [19]. The optical path is deflected by 90° towards all the cameras other than the bottom camera by mirror prisms.

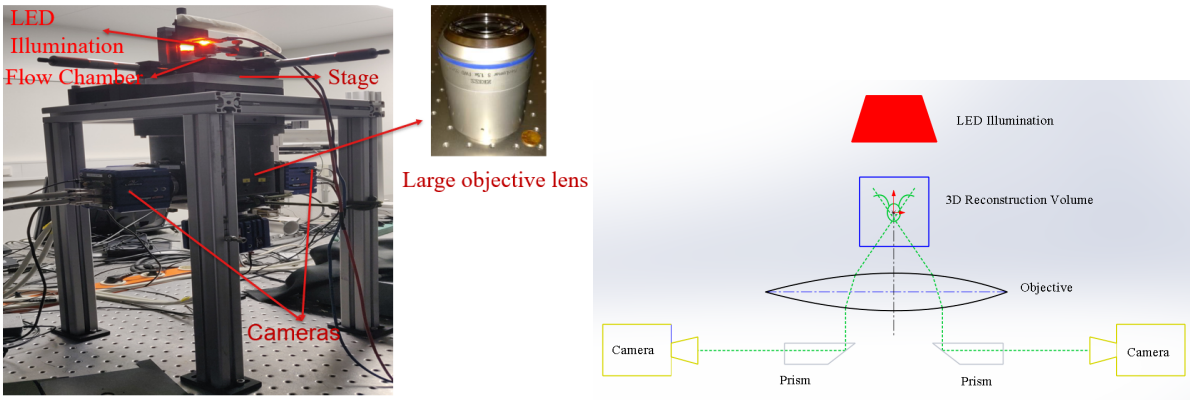

(a) Experimental setup

(b) 2D sketch illustrating the optical path followed

Figure 3.5: Experimental setup and optical path

3.3.3. Calibration

The calibration procedure is performed to obtain the relation between the coordinates of the physical object $x_0 = [x, y, z]^T \in \Re^3$ and the image plane $x_m = [x, y]^T \in \Re^2$, including magnification and optical distortion. A LaVision MP 100 μm calibration grid is placed at the position of the flow chamber holder. The coplanarity of the cameras is ensured without placing the pinhole card so as to reduce the depth of field. The orientation of each camera is adjusted until the calibration target representing a 2 × 2 mm plane, is centred and focused. This narrow depth of field reduces the Scheimflug effect [80].

After the focusing is completed, the pinhole card is added again to the setup and the LED illumination is provided for the calibration. In order to traverse a height of 2.4 mm along the z plane, the calibration is carried out on 13 planes spaced 0.2 mm apart. Although the domain volume for the object is 2 × 2 × 2 mm, an additional 0.4 mm is provided to include any possible effects of optical distortions or magnification during the experiment. The calibration is carried out on the DaVis 8.2.1 software that fits an analytical mapping function, $x_m = \mathbf{f}_{cal}(x_0)$, to map the physical

object space to the camera plane. The coefficients of this 3rd order polynomial mapping returned by DaVis in each x, y plane for a fixed height z are fitted in the object domain of height z using a 2nd order polynomial in Matlab.The calibration was carried out before and after the experiment to compensate for any mechanical misalignments.

$$\mathbf{f}_{\text{cal}}(x_0) = c_0(z) + c_1(z)x + c_2(z)y + c_3(z)xy + c_4(z)x^2 + c_5(z)y^2 + c_6(z)x^2y + c_7(z)xy^2 + c_8(z)x^3 + c_9(z)y^3 \tag{3.7}$$

3.3.4. Illumination conditions

Red LED illumination flashed from the top of the flow chamber using a DC source at 3.5 V and 1 A is used to illuminate the cells. The light is emitted at a wavelength of 613 nm and the light intensity is around 230 μmol/m^{2}s. This particular wavelength and colour of light is chosen to avoid, or at least minimize the phenomenon of phototaxis [15], the tendency of the cells to move towards or away from the light. The photoreceptors in the eyespot of the cells, rhodopsin, is sensitive to blue and green light, therefore, red light is chosen to minimize phototaxis [15]. The algae scatter the light in the forward direction towards the camera (Mie scattering) and appear as bright spots in the image. The images are taken at a frame rate of 20 Hz with an exposure time of 42000 μs.

3.4. Image processing

The raw experimental images appear as shown in Figure 3.6. The image processing is done using the codes developed by Muller [19] during his master's thesis. The code first seeks to eliminate any experimental artefacts such as pixel noise, image background and the blinking of cells (intensity not being constant in each image). The blinking is probably caused by the rotation of the algae, and this results in some cells scattering more light than the others. The pixel noise is suppressed by applying a linear Gaussian convolution whose width matches the expected particle shape. The blinking of cells is accounted for by applying a Min-Max filter.

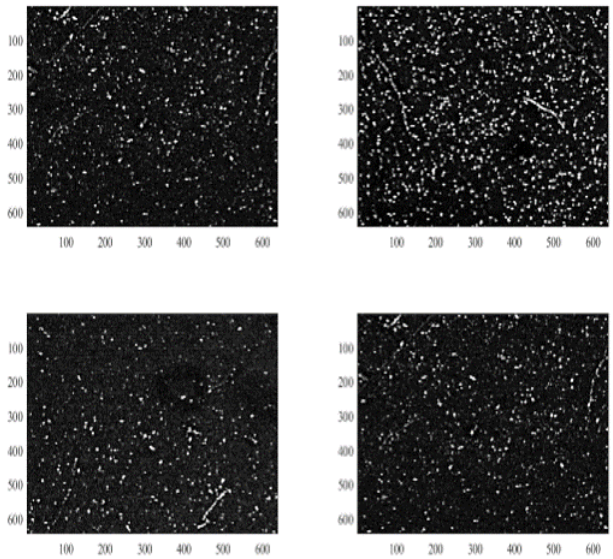

Figure 3.6: Raw image data before any processing or filtering

To determine the midpoints of the cells, the local intensity maxima of the bright cells in each image is first determined by assigning a segmentation level. The number of particle images in

each camera is thus estimated, allowing for the subsequent estimation of the variation of this number with time. To find cells that were blinking, the images are superimposed over another image where the expected number of cells is known. The variation in the number of cells with time is subsequently calculated for these images as well. The particle maxima are thickened using a binary mask that is applied to the raw image, allowing a Matlab code to determine the particle image midpoints based on an intensity weighted midpoint previously defined.

3.5. 3D Lagrangian particle tracking algorithm

To track the motion of the cells, the algorithm developed by K.Muller [19] based on the work done by Attanasi *et al* [81] was used. The first step in this algorithm is to track the cells in each camera. After this, the idea would be to find the same physical object corresponding to different positions in different cameras. This procedure is called matching [82]. Matching is achieved by projecting a particle image through the object space and projecting it back into another camera where it crosses another particle through its epipolar line [83]. This is illustrated in Figure 3.7. But as this method is sensitive to mismatching, a more robust approach is used.

The particle image midpoints are tracked in different image planes of one camera until the particle cannot be tracked due to either occlusion or disappearance. To account for displacements between other cells and to include the rapid change in direction of the cells, a search radius is defined and the particle image midpoint for each image in a camera is tracked until disappearance. This search radius is based on the average particle displacement between two frames with a confidence interval to include for higher displacements.

Though the particles are tracked in each camera in 2D, the matching of the tracks in different camera planes need to be done to obtain their positions in 3D. This consistent correspondence of tracks in different cameras is achieved by formulating an integer optimization problem by defining a cost function. The cost function contains the particle image midpoint and the distance from that midpoint to an epipolar line from another particle midpoint in another camera plane. Possible matches are considered only when the relative distance between the midpoint and the epipolar line is below a particular spatial threshold. To find the best possible match, the minimal value of the discrete cost function is solved efficiently using an Integer Linear Programming (ILP).

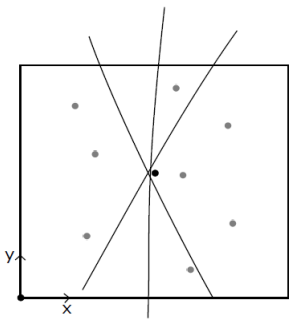

Figure 3.7: Epipolar lines projected from multiple cameras are matched with a camera's epipolar line to find the particle image midpoint. This is repeated over subsequent frames to track the cell.

This procedure can get increasingly complex for multiple camera frames, long times and a large number of particle midpoints, leading to a significant disparity between the calibration and the experimental data. A 'divide and conquer' algorithm is implemented to reduce the complexity of

the code [19]. Having matched the trajectory of the particles from different camera planes, the particle is then triangulated into physical space. The physical object position is reconstructed by the creation of a least-squares problem to invert the calibration mapping. The trajectories after triangulation appear as shown in Figure 3.8.

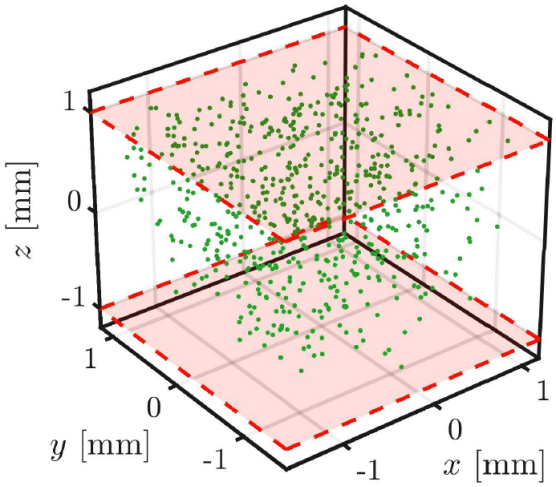

Figure 3.8: Location of cells at all times in the domain after triangulation.

3.6. Post-Processing

Though the triangulation and tracking of particles is completed, certain post-processing steps are necessary to obtain parameters important to characterise the trajectories of the cells. Once again, the post-processing steps required to do this are the same as those established by Muller [19]. To discard any noise present in the raw tracks, a curve fitting procedure is carried out using a Savitsky-Golay filter to smooth the data. A polynomial of order 3 is the minimum requirement for this filtering.

3.6.1. Kinematics of trajectory

The time-position information of the filtered trajectories is used to compute the local frame of reference using a Frenet-Serret framework [84]. The Frenet-Serret framework defines a local tangent **t**,local normal **n** and bi-normal vector **b** to the local trajectory $\mathbf{r}(t)$ known as the Frenet trihedron:

$$\mathbf{t}(t) = \frac{|\,\mathbf{r}\prime(t)\,|}{||\,\mathbf{r}\prime(t)\,||^2}, \quad \mathbf{n}(t) = \frac{|\,\mathbf{t}\prime(t)\,|}{||\,\mathbf{t}\prime(t)\,||^2}, \quad \mathbf{b}(t) = \mathbf{t}(t) \times \mathbf{n}(t) \tag{3.8}$$

The dynamics of the trihedron can be understood by the curvature κ and torsion τ which describe the evolution of the trihedron as:

$$\begin{bmatrix} \mathbf{t} \\ \mathbf{n} \\ \mathbf{b} \end{bmatrix}_s = \begin{bmatrix} 0 & \kappa\mathbf{I} & 0 \\ -\kappa\mathbf{I} & 0 & \tau\mathbf{I} \\ 0 & -\tau\mathbf{I} & 0 \end{bmatrix} \begin{bmatrix} \mathbf{t} \\ \mathbf{n} \\ \mathbf{b} \end{bmatrix} \tag{3.9}$$

where s indicates the differentiation with respect to arc length. The curvature is a measure of how much the trajectory is bent, and can be understood as a form of an inverse radius. The torsion, on the other hand, represents the twist in a trajectory. While both these parameters are useful in

describing a cell trajectory, it doesn't give the full picture. We know from Crenshaw *et al* [54] that cells generally execute a helical motion, so it would be better to characterise the trajectory in terms of the radius R and pitch P of the helix. These, along with the rotation rate Ω, can be calculated from the curvature and torsion.

$$R = \frac{\kappa}{\kappa^2 + \tau^2}, \quad P = \frac{2\pi\tau}{\kappa^2 + \tau^2}, \quad \Omega = \mathrm{sgn}(\tau) V \sqrt{\kappa^2 + \tau^2} \tag{3.10}$$

The kinematics of the trajectory can be quantified using these parameters.

3.6.2. Wall stretching

As the light scattered by the algae passes through lenses, the bounding domain of the resulting image is different from the actual value of 2 mm as the optical viewing axes pass through the flow chamber at an angle as shown in Figure 3.5b. This is primarily because of the change in refractive index from air to the lens and the viewing angle. Though the calibration is performed in air, its data is acceptable as the views are symmetric. To permit easier analysis of wall interactions, the domain is stretched by an appropriate factor so that it spans from -1 to 1. To accomplish the stretching, the actual positions of the wall has to be determined. From the results of K.Muller [19], we observe that the cells tend to accumulate at the walls. Thus, a plot of the surface distribution along the z-axis reveals the position of the walls as peaks.

While the above does give a good indication of the location of the walls, it might give a misleading impression if the images are dominated by noise. Generally, some cells adhere to the wall for some time and this leads to a drastic reduction in their speed. The position of the wall can thus be confirmed if the location of stationary cells can be determined, with the maximum concentration of stationary cells being naturally near or at the walls. Once the wall locations are determined, the positions of the cells are multiplied by an appropriate stretch factor corresponding to the refractive index of the lens.

3.6.3. Track selection criteria

In spite of taking noise and dead cells into account while running the code, some of the data it returns is bound to be spurious and noisy. In order to filter these tracks from those which are good, certain selection criteria need to be applied to the processed data. These are the following criteria that are applied to the tracks:

- A minimum and maximum median velocity limit to filter out dead cells and noisy tracks.
- A minimum track length to discard any spurious tracks.
- A standard deviation of tracks to further filter out noise.

The minimum and maximum velocity limit of the tracks are decided using the following method. The cells are tracked over 1000 images in 3D and a distribution of the median cell velocities is obtained. The cells change their velocities continuously so the median velocity of the track is selected. The median is taken over the mean as it illustrates a better picture of the swimming velocity. The velocity of the cells is drastically altered while encountering a wall or when they come in contact with another cell. To take these effects into account and to include the possibility of noise skewing the mean velocity of the tracks, the median velocity of each track is determined. The velocity limits are then chosen based on the speeds and the noise. A dead cell would naturally be drifting in the solution at low velocities as compared to the live cells. This makes them rather easy

to segregate from the rest. An upper limit for the velocities also needs to be applied as these tracks are probably noise dominated. These are determined by observing the tracks which are longer than 10 seconds, as they would give a better idea of the range of velocities at which the cells are travelling. The tracks at higher velocities are characterised by sharp jumps in different directions which appear as a bunch of straight lines rather than trajectories, indicating a result that is entirely dissimilar from the observed cell behaviour and one that is perhaps unphysical.

The code also gives out many tracks that are short in length. Many of these tracks are spurious and are likely to decorrelate over time, indicating that they are probably ghost particles. Additionally, these short tracks do not give enough information about the cell behaviour. Hence, tracks smaller than 1 or 2 seconds (chosen based on frame rate) are discarded.

In spite of applying these limits, noisy tracks characterised by drastic jumps in motion are common. While these tracks might contribute to the determination of velocities, it is difficult to characterise the nature of swimming from these tracks. For this purpose, a standard deviation between each data point based on a maximum instantaneous velocity is used to filter out these noisy tracks.

3.6.4. Frame rate

All the experiments were conducted at a frame rate of 20 Hz. For the TRIS case, this frame rate is acceptable and gives good results [19]. But for the rest of the cases, the velocities of the cells is slower than the TRIS case. This not only reduces the standard deviation of the distance between each point, thus increasing processing time, but also increases the propensity of noise to creep in the results. To illustrate this, the 500 ppm PASA is used as an example. The velocity of the cells in this solution is around 15 μm/s, which is nearly one-seventh of the value in TRIS (see section 4.3.1 for further details). The cells are tracked for 1500 images at frame rates of 2, 5 and 15 Hz and the selection criteria described in section 3.6.3 are applied. The results of the tracking are presented in Table 3.1, with a noisy track being defined as a track with a large jump in velocity as shown in Figure 3.9. From these results, it is evident that the results from the 2 Hz and 5 Hz data involves less noisy tracks compared to 15 Hz. Since the data at lower frame rates require less computational effort and time, it is advantageous to process tracks at these frame rates. The frame rate used for the data roughly scales with the velocity of the cells.

Table 3.1: Effect of frame rate on the nature of the tracks

Frame rate	Number of tracks after filtering	Number of noisy tracks
2	4545	767
5	4601	780
15	4412	2137

3.6.5. Fitting parameters

As explained in section 3.6, a Savitsky Golay filter with a cubic polynomial of order 3 is fitted over the tracks to smooth it. The fit length for the polynomial is chosen to remove the noise to a good extent without over-smoothing the tracks. This fit length is chosen based on the frequency at which the cells rotate counter-clockwise during the power stroke, which is at around 1-2 Hz for TRIS [15]. A frequency of 2 Hz corresponds to half a cycle, and this translates to 10 images for a frame rate of 20 Hz. Therefore, a fit length of 9-10 images is used for the TRIS case [19]. For the viscoelastic and

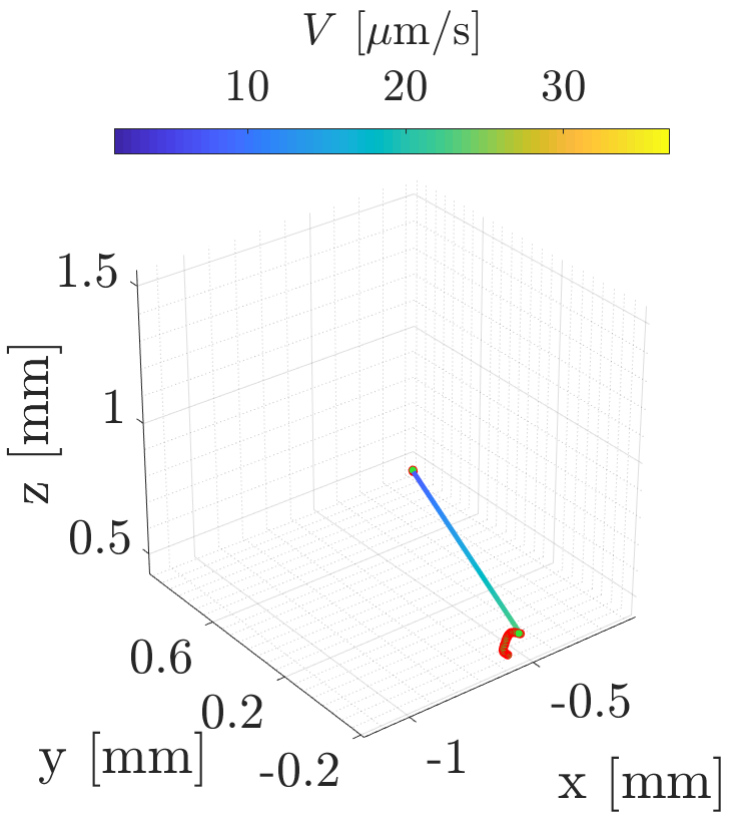

Figure 3.9: Example of noise in a track. A sharp jump is seen to connect two disparate set of points.

Newtonian cases, this is not as straightforward. An appropriate filter length needs to be chosen to avoid over-smoothing of the tracks leading to the loss of important data, while at the same time, the tracks should not be noisy. Since there are many cases to discuss, the procedure of selecting the fit parameters will be elaborated for the case of 150 ppm PASA solution, with some of the other cases touched upon in the Appendix D.

The frequency of the cells during the power stroke is unknown in all the fluids of higher vis-

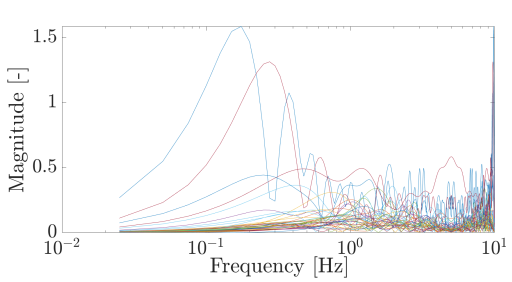

(a) FFT representing the frequency of individual tracks at every point. No clear dominant frequency is observed.

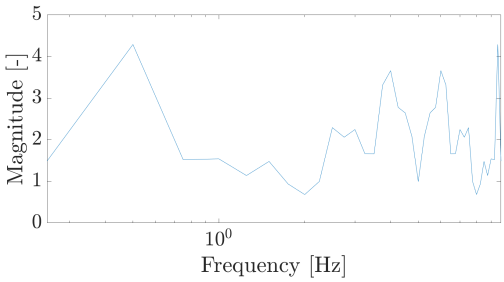

(b) FFT representing the median frequency of all the points of each track. No clear dominant frequency is observed.

Figure 3.10: Fast Fourier Transform (FFT) plots to find dominant frequency

cosity. The Fourier transform of the velocity and acceleration is plotted for each track against the frequency in log scale for the unfiltered as shown in the Figures 3.10a and 3.10b. The first plot represents all the frequencies of every track whereas the second plot only shows the median

frequency of each track. The magnitude in the plot represents the Fast Fourier Transform (FFT) of the parameter divided by the number of points. In case of the median frequency, the FFT is divided by the number of tracks. This explains the difference in magnitude between the two plots. The sampling frequency corresponds to the frame rate used for each data set, which in this case, is 20 Hz. The results from these plots are inconclusive, with the only dominant frequency close to zero Hz, which is probably either because of physical long period variations dominating over short period fluctuations or because of noise.

To decide on the filter length, the following procedure is used. The first 2000 tracks from the data set are post-processed using different fit lengths and the obtained parameters (pitch and radius of the helical trajectory, velocity, and acceleration) are plotted. The selection criteria are applied to these tracks to allow for easier analysis. As explained in section 3.6.3, the plotted velocity and acceleration represents the mean of the median track velocities. As for the pitch and radius, the absolute mean of the local values is taken instead of the median as that would give a better representation of the results for a short number of tracks. Ideally, the expected behaviour would see the mean values of the parameters initially increase with filter length, after which the values stagnate for a while, followed by a decrease in their mean which corresponds to over- smoothing. The chosen filter length should be within the stagnation range.

From the Figures 3.11a and 3.11b, we can see that the velocity remains relatively unchanged while the acceleration continues to decrease with increasing filter length. This decrease is most likely due to over-smoothing of the tracks. The trend followed by pitch and radius gives credence to this hypothesis. The pitch remains relatively constant from a filter length of 7 till 11, after which there is a noticeable change. Though the radius appears to remain constant, a slight decrease in radius is observed at a filter length of 15, possibly indicating over-smoothing. Taking all these factors into consideration, a filter length of 11 is chosen. This is repeated for the other cases as well.

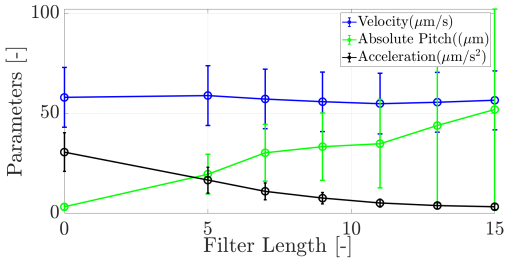

(a) Variation of parameters with filter length.The error bars represent the standard deviations of the parameters.

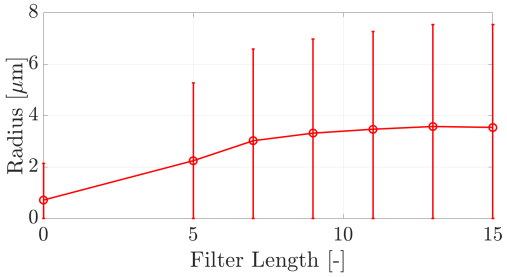

(b) Variation of radius of the helical trajectories with filter length.The error bars represent the standard deviations of the radius.

Figure 3.11: Plots to select appropriate filter length

4

Results

The results obtained from the experiments described in the previous chapter are discussed here. The main objective is to elucidate the effect of viscoelasticity on the physics of the swimming algae by characterising the differences between the Newtonian and viscoelastic cases. The first two sections deal with the results from the rheometry and relaxation time measurements. The first step in analysing the influence of viscoelasticity on the algae would be to understand the kinematics of cell motion, and that naturally, will be the focus of the third section. Here, the focus is on the velocities and the nature of the swimming trajectories. The presence of two confined surfaces naturally leads to an increase in complexity, and this cell-wall interaction would constitute the final section.

4.1. Rheometry

The viscosities (μ) of the viscoelastic PolyAcrylamide Sodium Acrylate (PASA) solutions were determined from the Contraves LS-40 rheometer and plotted in a log-log scale as shown in Figure 4.1. The viscoelastic solutions were found to depict a shear-thinning behaviour, i.e, the viscosities were observed to decrease with an increase in the shear rate. The degree of shear-thinning increased with an increase in PASA concentration.

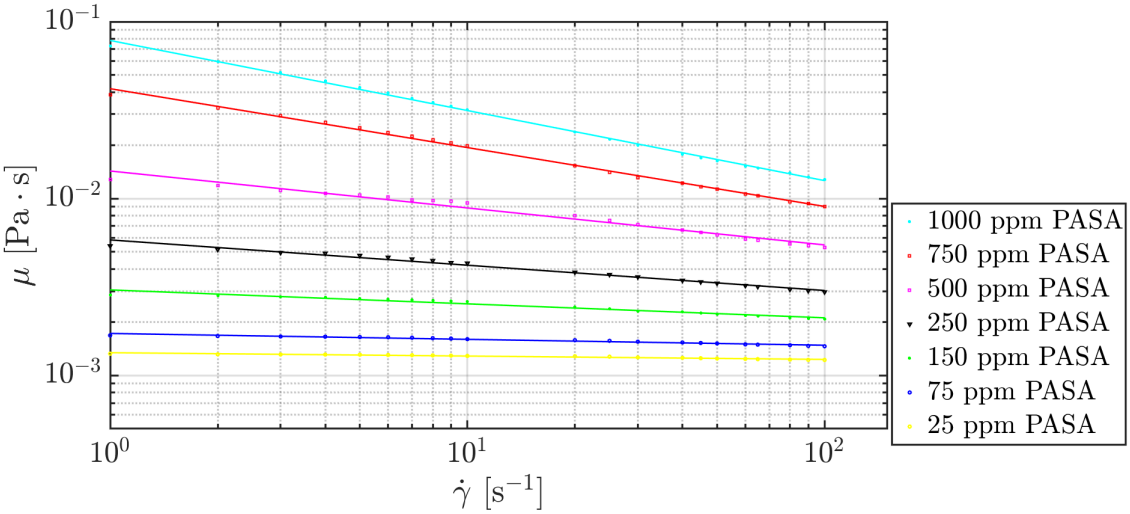

Figure 4.1: Viscosities of PASA solutions of different PASA concentrations for different shear rates

For comparison, Newtonian solutions of increasing viscosity were prepared by adding varying concentrations of Ficoll to TRIS medium. Since the viscoelastic solutions are shear-thinning, it is difficult to pinpoint the exact value of viscosity that could be used for comparison. In the case of *C.Reinhardtii*, there are two sources of shear acting on the fluid- the flagella and the body. The flagellar shear rate can be considered to be around the same order as the frequency of beating, which is around 50 Hz [16, 52]. The shear rate applied by the body is a lot more complicated, as there is an asymmetry associated with the front and reverse stroke [53]. Qin *et al* assumed the body shear rate to be equivalent to the ratio of the mean of the front and reverse stroke velocity to the cell diameter. The net shear rate applied on the fluid was taken by Qin *et al* as the average of the two values, and this was found to be ranging from 30-50 /s. Using these results, the viscosities of the Ficoll solutions were prepared to be within 10 % of the corresponding viscosities of the viscoelastic solutions at these shear rates. The viscosities are plotted in Figure 4.2

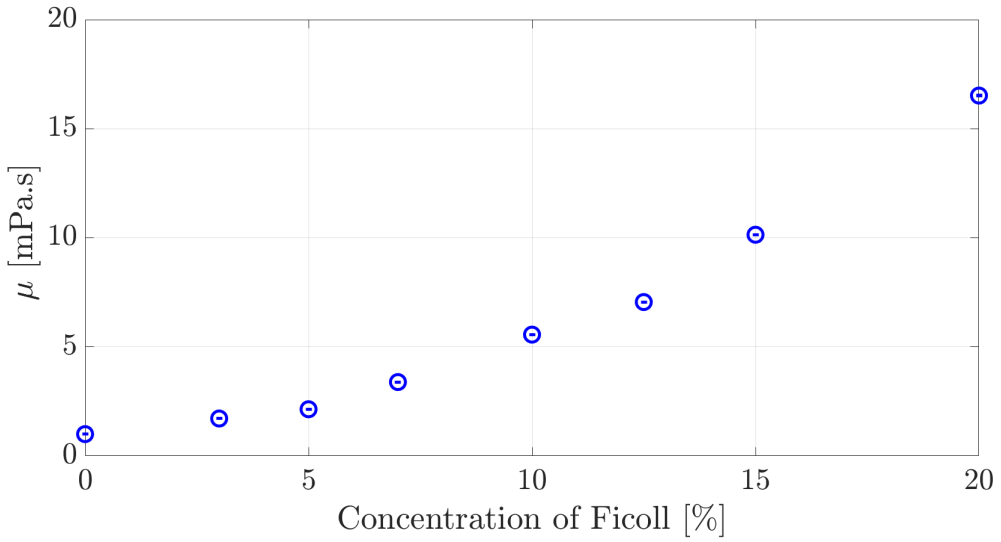

Figure 4.2: Viscosities of Ficoll solutions of different Ficoll concentrations

4.2. Relaxation time

The measurement of the relaxation times was conducted by Parviz Ghoddoosi Dehnavi using the optical trap for TRIS, 150 ppm PASA and 250 ppm PASA solutions. TRIS was used as a base to check the accuracy of the method. The rheological results for viscosity from the optical trap experiments were first compared with those from Section 4.1. The results are plotted in Figure 4.3 .

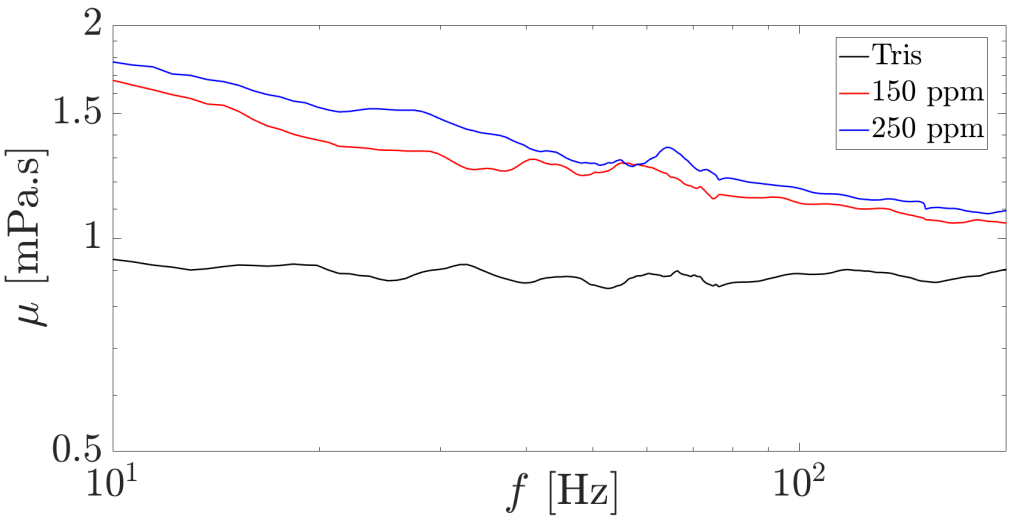

Figure 4.3: Viscosity measurements using optical trap

Though the viscosities appear different from those in Figure 4.1, it must be noted that the optical trap experiments were conducted at 22° C, whereas the experiments in the LS-40 rheometer were conducted at 20° C. Also, the results in Figure 4.1 showed the variation with shear rate, whereas the variation of viscosity with frequency is plotted in Figure 4.3. The shear-thinning behaviour in the 150 and 250 ppm PASA solutions is captured. The viscosity of TRIS is close to the viscosity of water at 22° C (0.95 mPa.s), so it can be concluded that viscosities measured by this technique are close to the true value.

The viscous and elastic moduli as a function of the frequency are plotted for the three solutions in Figure 4.4. In TRIS (Figure 4.4a), the elastic modulus appears only in the form of noise. In the 150 and 250 ppm PASA solutions (Figures 4.4b and 4.4c), no crossing of the two moduli is observed in the frequency range, although a value might be obtained by extrapolation. This means that the solutions are weakly viscoelastic or there are some errors involved when conducting the experiment. More measurements using this technique has to be done with solutions of known relaxation times to establish a definite methodology. The viscoelastic behaviour of the solutions is difficult to discern as there is no basis for comparison. Due to the lack of time, this could not be done.

(a) TRIS **(b)** 150 ppm PASA **(c)** 250 ppm PASA

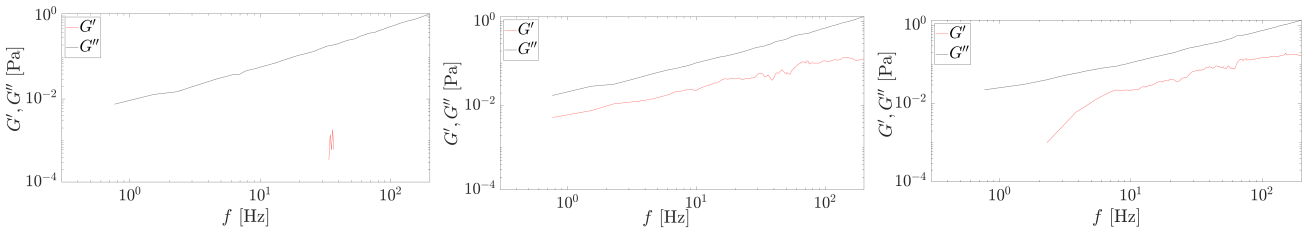

Figure 4.4: Variation of the viscous and elastic moduli as a function of frequency. No relaxation times could be obtained as no crossing was observed.

4.3. Motility and kinematics

The kinematics and motility of the cells are expected to change not only for viscoelastic fluids but also for the more viscous Newtonian fluids. The effects of higher viscosity and viscoelasticity on

the velocity of the microorganisms have been documented to some extent in both experimental and numerical studies, with some studies going even further to analyse the causes of these effects [27, 52, 53, 62]. While all these studies have focused on the velocities and stresses applied on the cells, most of them are restricted to the 2-dimensional case. This section of the thesis does not only aim to validate existing research on the velocities of the cells in 3D but also to try to understand the possible influence viscosity and viscoelasticity might have on the helical trajectories of the cells observed in the low viscosity TRIS case [19, 54].

4.3.1. Velocities

The cells were not observed to swim at a fixed velocity but a range of different velocities. The median velocity of each track, V, is determined and the range of velocities are chosen according to the procedure explained in section 3.6.3. The velocities of the cells decreased with an increase in the concentration of Ficoll (V_N) for the Newtonian case and with an increase in the concentration of PASA in the viscoelastic case (V_{VE}). The mean velocity of all these tracks are calculated and the results for the two cases are plotted in figures 4.5a and 4.5b. The error bars represent the standard deviation of the mean velocity.

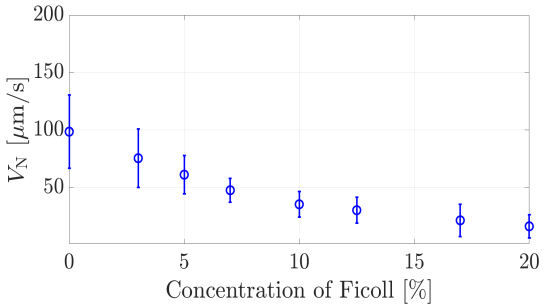

(a) Velocity of the cells in solutions of different Ficoll concentrations.The error bars represent the standard deviations of the velocities.

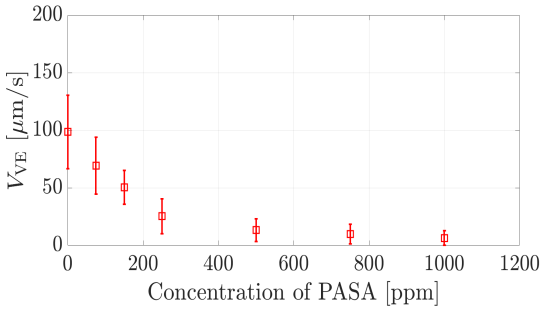

(b) Velocity of the cells in solutions of different PASA concentrations. The error bars represent the standard deviations of the velocities.

Figure 4.5: Velocity as a function of concentration

Since the polymer used for the Newtonian fluid is the same as the one used by Qin *et al* [52], the velocities from both the cases are plotted on a log-log scale against viscosity μ in Figure 4.6. Though the velocities are not the same, the qualitative behaviour is similar. The possible reason for this discrepancy is probably because Qin *et al* observed these results for fewer cells, whereas our experiments were conducted for concentrations as high as 1×10^5. The velocities from our experiments are observed to vary nearly linearly with the viscosity.

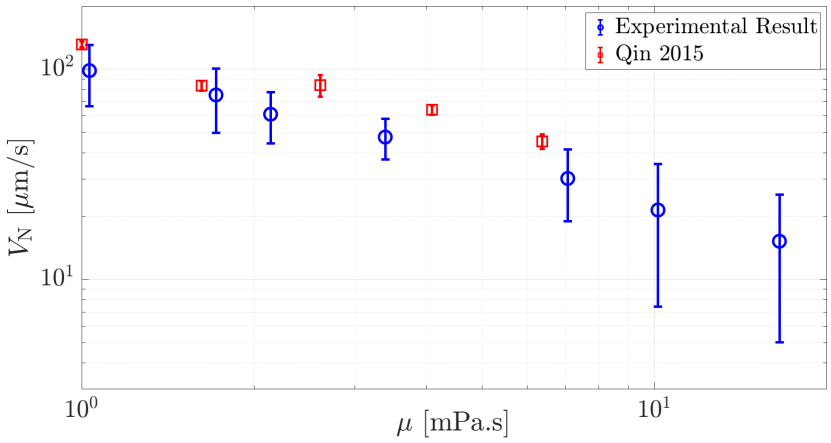

Figure 4.6: Velocity of the cells in Ficoll solutions compared to those obtained by Qin. The error bars represent the standard deviations of the velocities.

To compare, the variation of cell velocity with viscosity in viscoelastic (V_{VE}) and Newtonian (V_N) fluids is plotted along with the ratio of the mean velocity in the viscoelastic case to that of the Newtonian case against different viscosities in Figures 4.7a and 4.7b. The viscosity of the viscoelastic fluids was taken as the mean of the values at shear rates of 30, 40 and 50 s^{-1}. The experiments have been conducted twice for each case and the velocities are observed to be reproducible. The velocities in the viscoelastic fluids are clearly lower than the Newtonian case, with the velocity ratio decreasing with viscosity. A significant drop at a viscosity of around 3.4 mPas is observed, after which a stagnation of around 0.42 is reached. While the obtained results are consistent with numerical [37, 38] and experimental studies for *C.Reinhardtii* [52] and *C.Elegans* [49], it should be noted that the equivalent shear rate which the cells apply on the viscoelastic fluid has not been determined, but theorized from existing literature and obtained velocities and frequencies. Additionally, the relaxation times for all these solutions were not determined, so the results are not plotted against the Deborah or Weissenberg number. The plateau might be indicative of a maximum elastic stress generated around the organism.

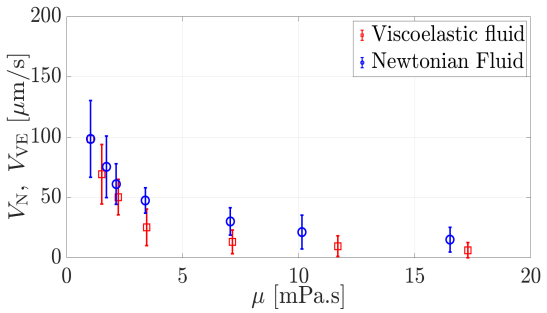

(a) Comparison of cell velocities in Newtonian (blue circles) and viscoelastic fluids (red squares) of similar viscosities.The error bars denote the standard deviations of the velocities.

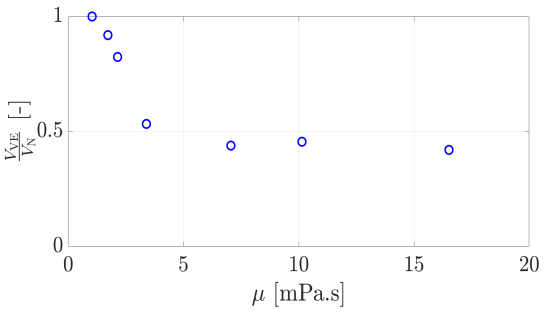

(b) Ratio of cell velocities in viscoelastic fluids to that in Newtonian fluids of similar viscosities. The ratio appears to saturate after the 250 ppm PASA solution at a value of 0.42.

Figure 4.7: Velocity of the cells as a function of viscosity in Newtonian and viscoelastic fluids.

From these results, it is pretty clear that viscoelasticity has a considerable effect on the motility of the cells. To further expand on these results, the trajectories are studied. In order to aid easier

observation and characterisation of the results, the trajectories of 150 and 250 ppm PASA solutions, and the 7 and 12.5 % Ficoll solutions are studied in detail. These solutions were chosen because their velocities were reasonably high to characterise the effects of viscoelasticity. It is difficult to demarcate the effects of viscosity and viscoelasticity on the trajectories from the solutions of high viscosities as the cells are travelling at very low speeds. Some of these difficulties are elucidated in Appendix C. Since the drop in velocity for the 250 ppm PASA solution (viscosity ~ 3.4 mPas) is drastic, it would be a good idea to observe the trajectories and compare it to the 150 ppm case, where the velocities are much higher. This would permit an easier understanding of the effect of elasticity and observe any possible effects caused by this drastic drop in velocity.

For comparison, two Newtonian solutions are selected. Since the exact shear rates applied by the cells on the solution is unknown, the trajectories of the cells are compared with the corresponding Newtonian cases of similar viscosity and velocity. The 7 % Ficoll solution has a similar viscosity to the 250 ppm PASA solution, whereas the cells in the 12.5 % Ficoll solution swim at similar velocities as compared to the 250 ppm PASA case. This is clearly illustrated in Figure 4.8. The velocity distributions of the cells in these solutions are plotted in Appendix F.

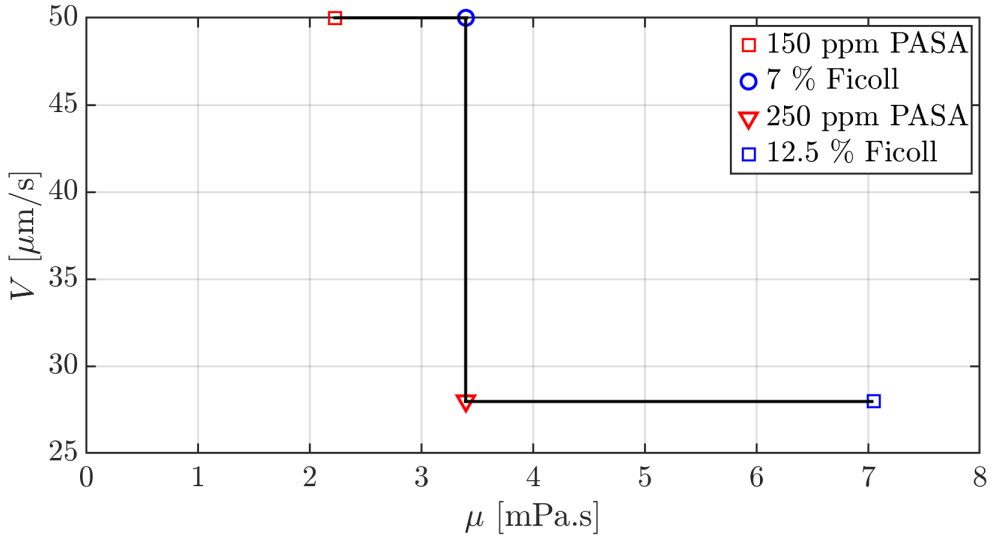

Figure 4.8: Figure illustrating the points of comparison of the chosen solutions

4.3.2. Frame rate and fit length

Based on the velocities of the cells, the frame rate is chosen according to the procedure mentioned in section 3.6.4. The fit length for the Savitsky-Golay filter is also chosen for the four solutions based on the procedure explained in section 3.6.5. These values are shown in Table 4.1.

Table 4.1: Frame rate and fit length for each solution

Solution	Frame rate	Polynomial order	Fit length
TRIS	20	3	9
150 ppm PASA	10	3	11
7 % Ficoll	10	3	11
250 ppm PASA	5	3	11
12.5 % Ficoll	5	3	11

4.3.3. Trajectories and kinematics

The helical trajectory followed by cells in TRIS medium is well documented [19, 54]. To check if these trajectories are still being maintained in viscoelastic fluids, some tracks are plotted for the 4 cases discussed above. The mean free paths of the cells, defined as the average distance travelled by the cell between collisions with other cells, in all the solutions are plotted in Appendix E to check for the possible influence of cell-cell interactions. The mean free paths were quite large which led to the conclusion that the cell motion is probably not influenced by other cells.

For all the cases, the cells have been found to display helical trajectories. Cells execute a repeatable,serpentine helical motion (Figures 4.9a, 4.9b, 4.10a and 4.10b) in all the solutions, but this motion has observed to be a lot more common in the 150 ppm PASA case. A strange phenomenon (circling) which has only been documented near the walls for the TRIS case [19] seems to occur in the bulk in all solutions with higher viscosity (Figures 4.9c, 4.9d, 4.10c, 4.10d). This circling motion in the bulk, though rare, is observed to be more common in the viscoelastic cases than in the Newtonian ones. Certain complex helical motions that are difficult to classify are also observed (Figures 4.9e, 4.9f, 4.10e, 4.10f). The boundaries for all these plots are located at $z = -1$ mm and $z = 1$ mm. The appearance of these trajectories seem to indicate a frequent reorientation in the swimming motion in higher viscosity solutions. In addition to these, there are quite a few tracks that execute a relatively straight motion.

From a mere perusal of these tracks, it is difficult to exactly pinpoint the differences between the viscoelastic and Newtonian cases, although certain differences in the pitch and nature of the helix can be seen. To quantify these differences, the relative probability density of radius and velocity, pitch and velocity, and pitch and radius are plotted in Figure 4.11. The radius R and pitch P of the helix are calculated from the torsion and curvature using the equations described in section 3.6.1. A test TRIS sample was used during the experiments as a means of confirming the accuracy of the obtained data. This sample was processed only for 5 minutes, in contrast to the 20 minutes for the other cases.

The obtained radii for the TRIS case (Figure 4.11a) doesn't appear to have any relationship with the velocity. The pitch, on the other hand, increases with an increase in velocity up to a value of around 80 μm. From Figure 4.11a, it is evident that cells tend to swim with a positive chirality, i.e, right-handed chirality, whereas in Muller's [19] case, the cells tended to swim with a left-handed chirality.

The following Figures (4.11b, 4.11c, 4.11d, 4.11e) clearly show an effect of viscosity on the trajectories of the cells. While it is hard to decipher the effect of viscosity on the radius, a reduction in pitch is clearly observed. The chirality is still maintained for all the cases. The pitch appears to reduce with an increase in viscosity, with the cells in 250 ppm PASA solution and Ficoll 12.5 % solution displaying lower values than the rest. The pitch and velocity tend to scale in a linear fashion for all the solutions until a particular value of pitch, after which it is scattered. The relationship between radius and velocity is unclear, with greater scatter observed at velocities closer to the mean velocities of the cells. Considering that Ficoll 12.5 % has a higher viscosity than the 250 ppm PASA solution (refer Section 4.1), it is surprising to find that the radius and pitch in these solutions are comparable. This might be indicative of an effect of viscoelasticity on the trajectories of the tracks.

(a) Simple helical swimming

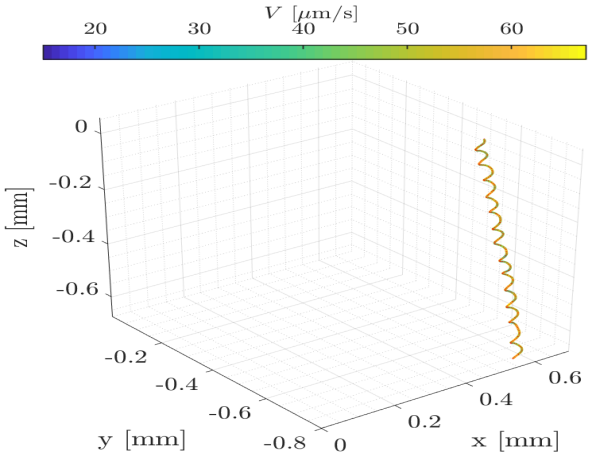

(b) Simple helical swimming

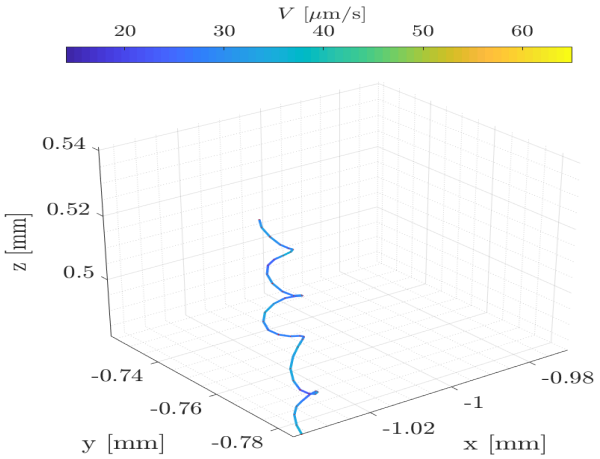

(c) Circling in the bulk

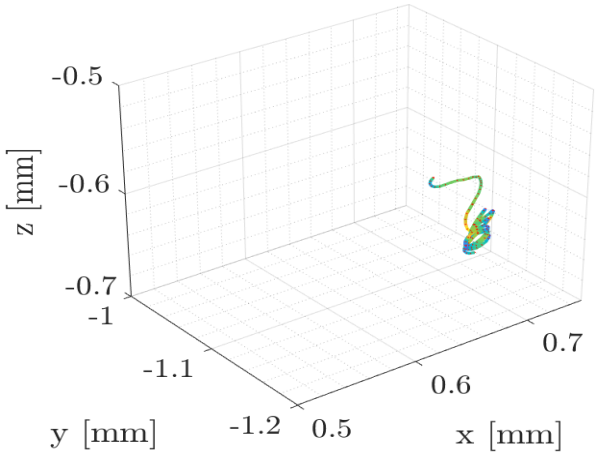

(d) Circling in the bulk

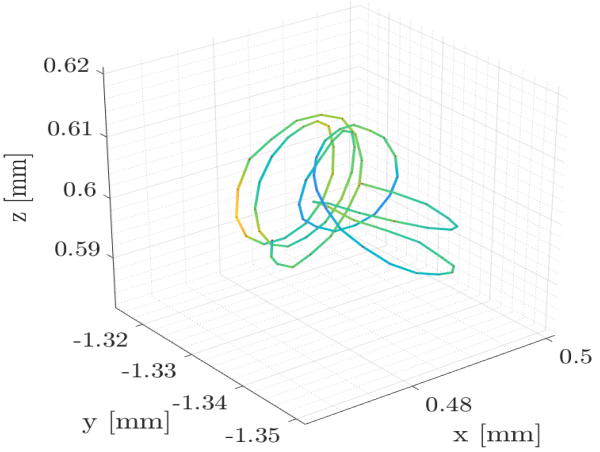

(e) Complex helical swimming

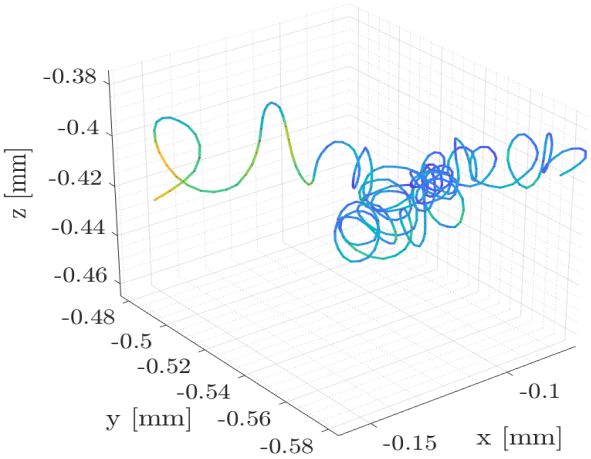

(f) Complex helical swimming

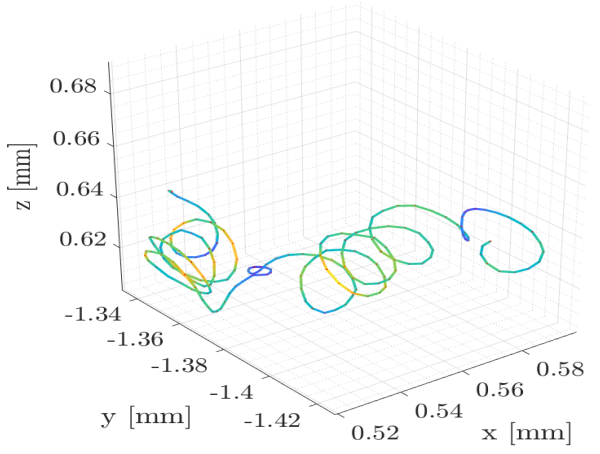

Figure 4.9: Different trajectories found in 150 ppm PASA (a,c,e) and 7 % Ficoll (b,d,f) solutions

(a) Simple helical swimming

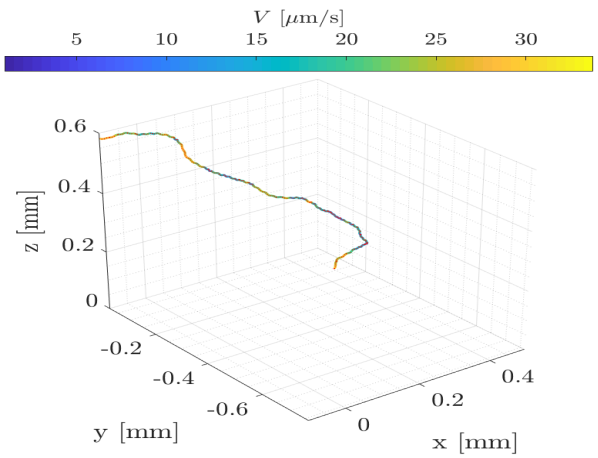

(b) Simple helical swimming

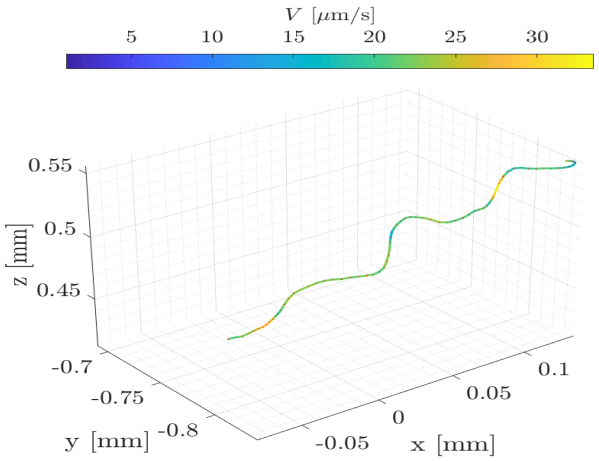

(c) Circling in the bulk

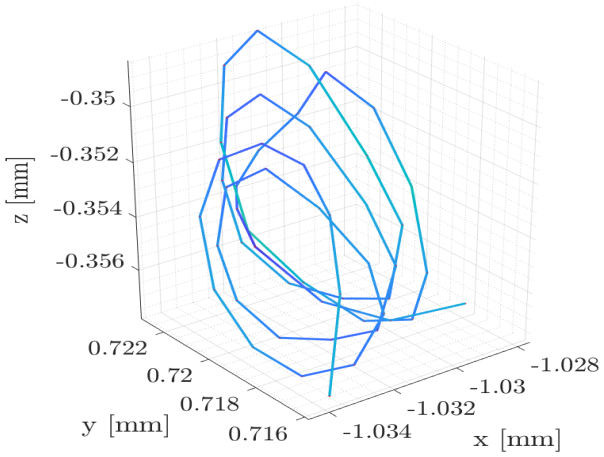

(d) Circling in the bulk

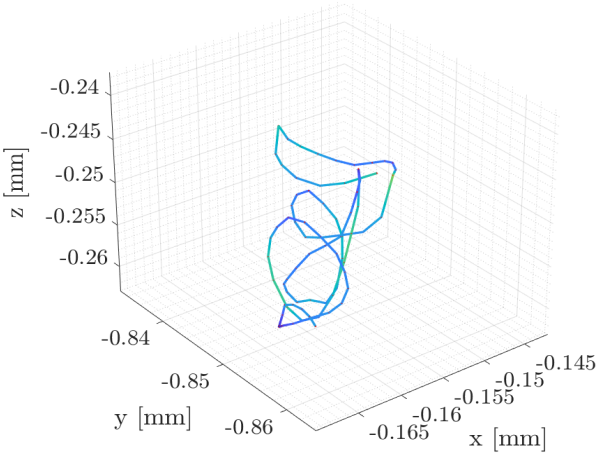

(e) Complex helical swimming

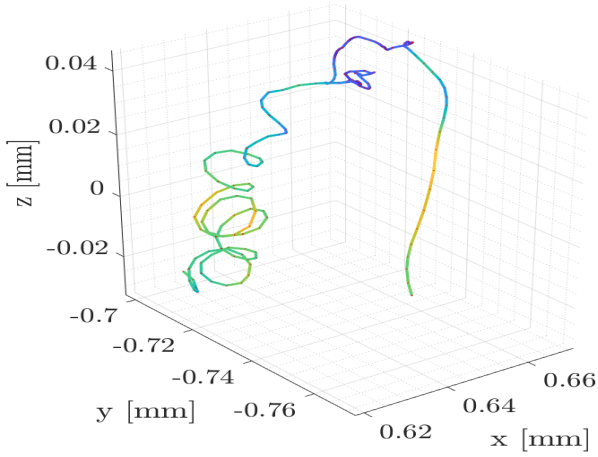

(f) Complex helical swimming

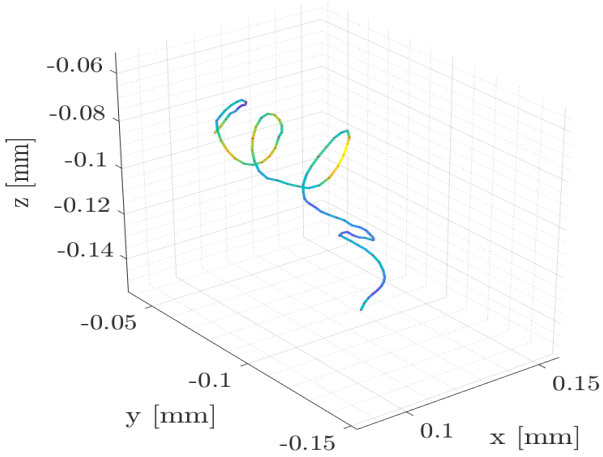

Figure 4.10: Different trajectories found in 250 ppm PASA (a,c,e) and 12.5 % Ficoll solution (b,d,f)

(a) Kinematics of cells in TRIS

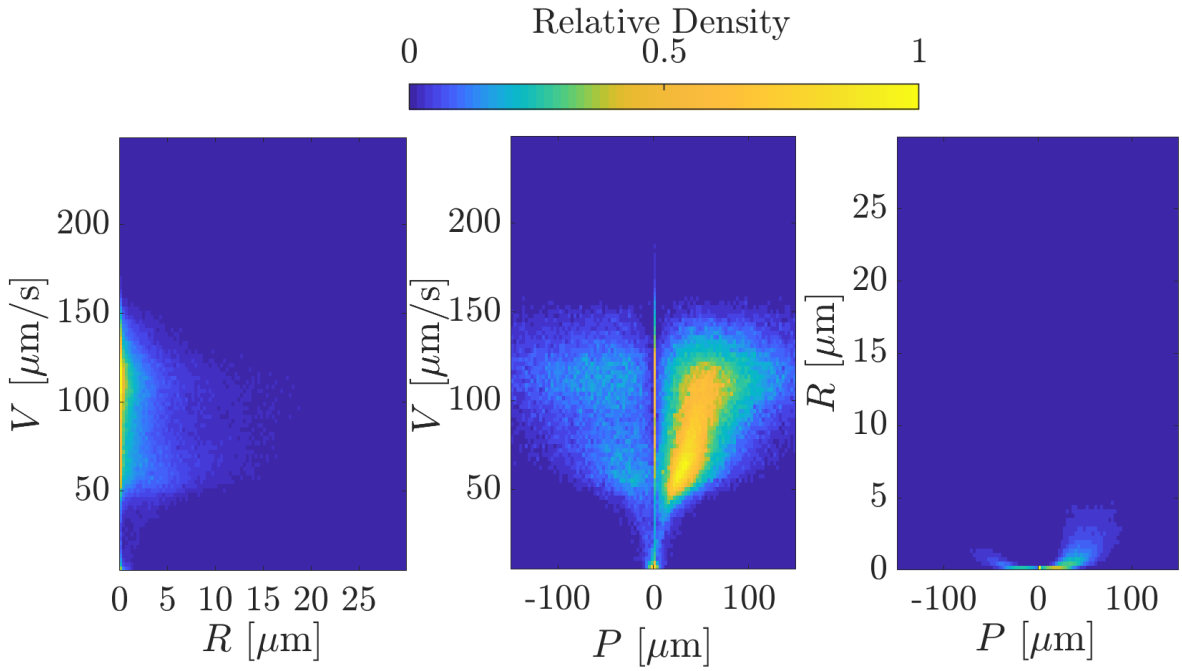

(b) Kinematics of cells in 150 ppm PASA solution

(c) Kinematics of cells in 7 % Ficoll solution

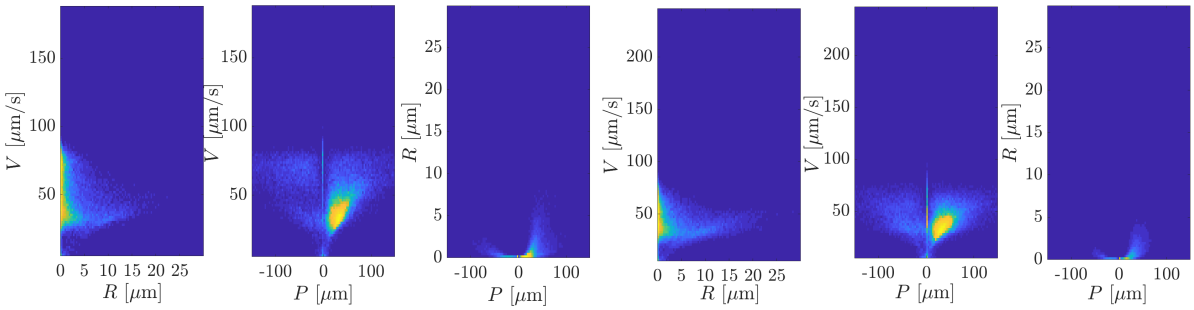

(d) Kinematics of cells in 250 ppm PASA solution

(e) Kinematics of cells in 12.5 % Ficoll solution

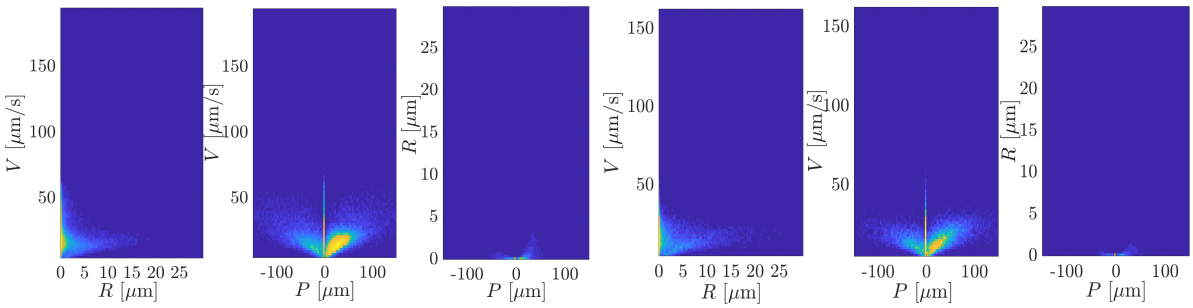

Figure 4.11: Relative probability density of parameters pertaining to the kinematics for different solutions

To further characterise the kinematics, the mean radius, pitch and the rotation rates are summarized along with the velocities in Table 4.2. The rotation rate Ω is calculated using Equation 3.10. It is found to reduce for the viscoelastic solutions if the comparison is restricted in terms of viscosity alone. For solutions where cells swim at similar velocities, however, the rotation rates in the viscoelastic solutions are slightly higher than the corresponding Newtonian case. The table gives a better idea on the effect of viscosity on the radius of the tracks, with the mean radius decreasing

with viscosity. The mean values of the absolute pitch merely confirm what we already observe in Figure 4.11. The ratio of the radius to the pitch (aspect ratio, A) is also calculated for all these cases to observe if there is any change in the nature of their helical trajectories. The aspect ratios for all the cases were determined to be around 0.09, indicating that the cells still retain their tendency to move in elongated helices though the actual helical trajectory is constricted. The percentage of cells swimming with a positive chirality is also calculated, to check if viscosity has any effect on how the cells move. There is a slight drop in the percentage from TRIS to 150 ppm PASA, after which the percentage remains constant. Thus, the viscosity does not seem to have a tangible effect on the chirality.

Solution	V **(μm/s)**	R**(μm)**	P**(μm)**	A	**% Positive Chirality**	Ω **(rad/s)**
TRIS	97.07±34.58	4.97±5.77	53.5±34.72	0.093	73.4	11.54±11.13
150 ppm PASA	52.92 ±15.76	3.76±5.11	41.84±32.92	0.09	65.9	7.33±8.07
7 % Ficoll	49.96±12.04	3.98±6.09	45.16±31.89	0.088	66.1	6.24±6.93
250 ppm PASA	26.63±13.41	2.66±4.87	30.77±34.73	0.086	64.8	3.56±4.95
12.5 % Ficoll	24.36±6.91	2.81±4.92	30.95±29.71	0.091	64.6	2.086±3.28

Table 4.2: Parameters representing motility and kinematics for all solutions

4.4. Cell-Wall interactions

The presence of a confined boundary naturally introduces certain complications of its own. From the results of Muller [19], it is evident that there are numerous factors to consider when trying to classify cell-wall interactions. From the existing literature in the Newtonian case [30, 31, 85], cell-wall interactions can either be of a hydrodynamic nature, a contact nature, or both. For the viscoelastic case, however, there are primarily papers concerned with simulations [39, 40, 42], near a boundary, and all of these focus only on the wall hydrodynamics without taking the possible wall contact into account. Though it is difficult to tell whether the obtained results in our case is due to contact or hydrodynamics as the flagellar movement is not captured in these experiments, the objective is to elucidate the possible differences in cell-wall interactions in solutions of higher viscosity and viscoelasticity. Certain statistics are plotted for the 4 cases to possibly understand the happenings near the wall and comment on the nature of the interaction as well. It should be noted that the presence of the boundaries do not necessarily influence the dynamics in the bulk and restrict the motion of the cells as they can traverse over a large domain with a depth of 2 mm.

4.4.1. Cell distribution

The results from Muller [19] indicate a concentration of cells near the boundaries. Of course, there is a possibility that the data is skewed because of an inordinate number of immobile cells. To minimize this bias, the cell distributions are plotted only after applying the track selection criteria discussed in Section 3.6.3. To see if viscosity or viscoelasticity might have a possible impact on the accumulation of cells at the boundary, the probability density function (PDF) of cell positions in the z-axis for all the tracks is plotted against the height of the domain for the 4 cases along with TRIS in Figure 4.12. The overall trend followed by the cell concentration profile is similar for almost all the cases, with a significant proportion of the cells moving towards the boundaries. A decaying trend from the top to the bottom wall is observed, indicative of negative gravitaxis. The only solution that differs from this trend is the Ficoll 12.5 % case (Figure 4.12e). This discrepancy is probably due to the noisiness of the images captured for the Ficoll 12.5 % case, indicated by the faint dots shown

in Figure 4.13. These faint dots were absent in the other cases, possibly explaining the reason for the discrepancy. Although the noisy tracks are removed using a standard deviation as discussed in Section 3.6.3, there are tracks with low standard deviations that still have jumps in distance that might skew the distribution. This doesn't mean that the other cases are entirely free of these tracks, but the degree is considerably lesser. A median filter is applied to remove the fainter dots in the image, but the number of viable tracks is still lesser than the rest of the cases. The efficiency of the tracking code is reduced because of these faint dots.

Figure 4.12 indicates the total number of points in each z bin for all the cells. While this gives a good idea of the region where the data is concentrated, the effect of time is not taken into account, thus this metric does not give a full picture of the cell density. If there are a greater number of longer tracks near the upper wall, the concentration profile portrays a skewed picture based on the number of points instead of the overall cell behaviour. To take this factor of time into account to get a better understanding of cell accumulation at the walls, the cell density, ρ is calculated by determining the ratio of the mean number of points corresponding to each frame to the volume, and subsequently determining the z bin where these points are concentrated. Since the area in the x-y plane is not constant throughout, the area is determined by finding the convex hull corresponding to the height. As this includes the normalised density from each frame instead of the overall number of points and accounts for the varying area in the x-y plane, these cell densities provide a clearer picture of the cell distribution than Figure 4.12. The cell densities are plotted in Figure 4.14. Again, the cell densities indicate a tendency to move towards the upper wall for all the cases except for the Ficoll 12.5 % solution, although the gravitaxis is not as pronounced as before.

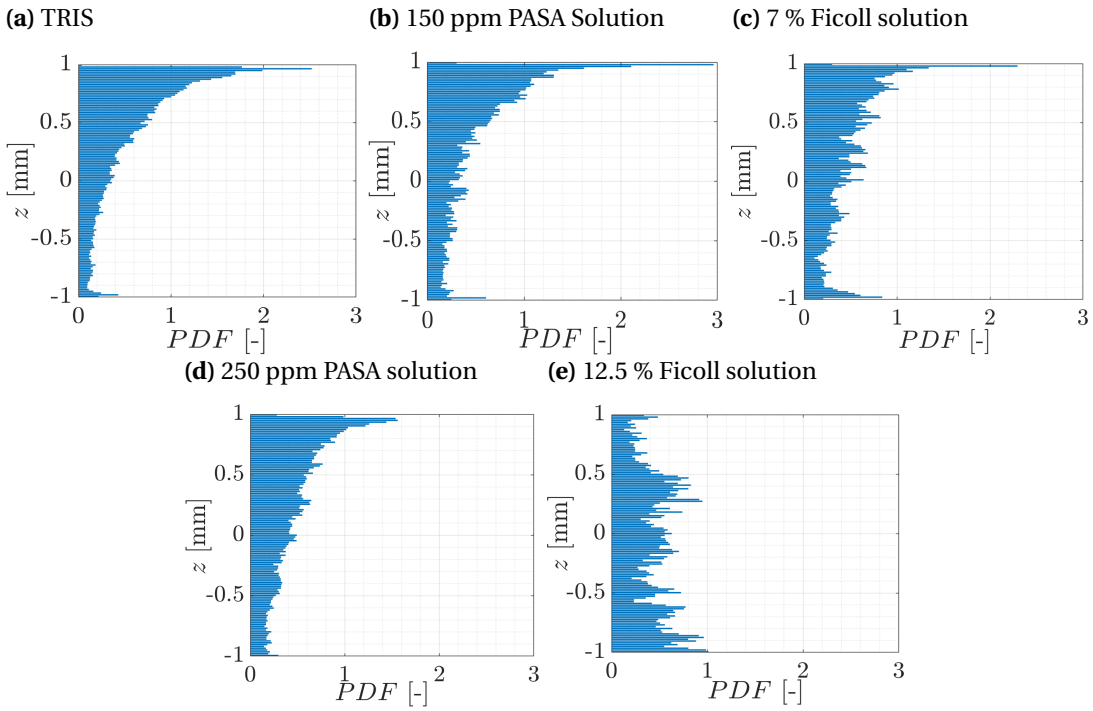

Figure 4.12: Cell concentration profiles in different solutions

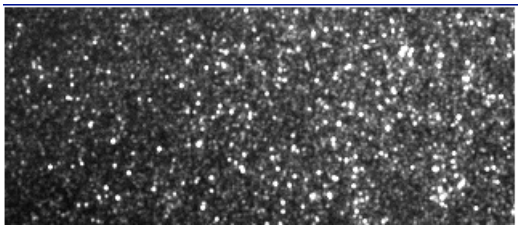

Figure 4.13: The images for the cells in the Ficoll 12.5 % solution. In addition to these bright dots (algae) observed, there are a large number of faint dots of smaller size that might have affected the tracking efficiency

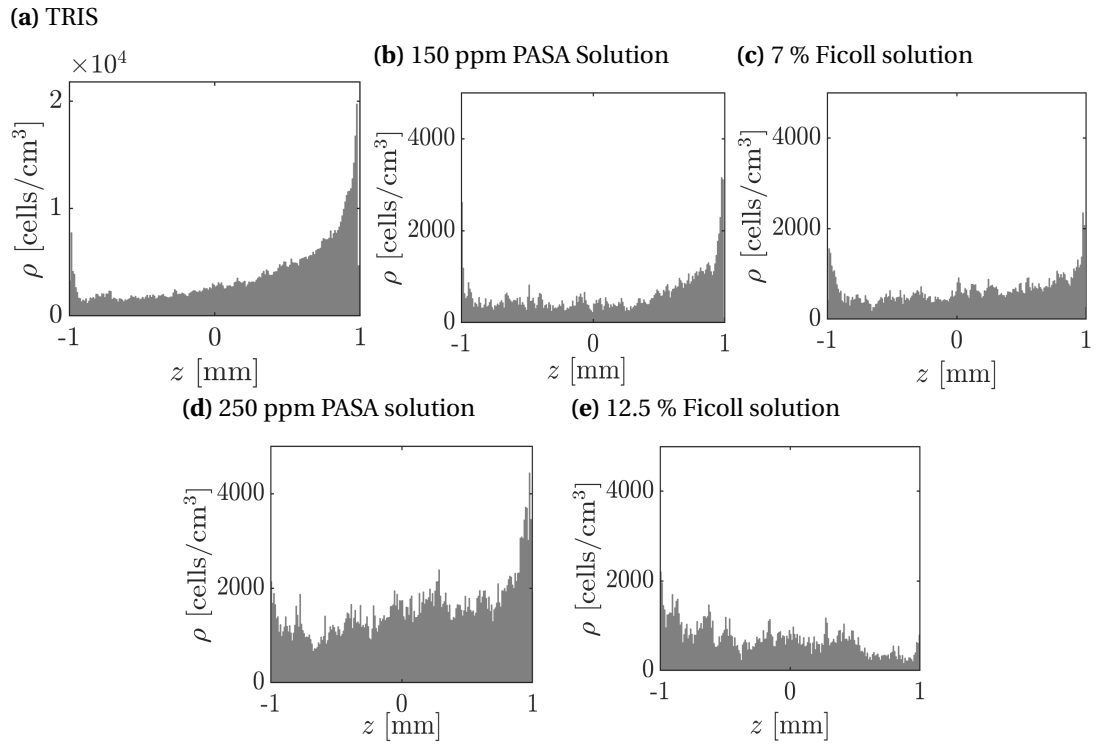

Figure 4.14: Time averaged cell densities

4.4.2. Trajectories

Before trying to analyse the cell-wall interactions, the limits defining a possible cell-wall interaction, with a demarcation between contact and hydrodynamic region, need to be defined. The limits utilized by Muller [19] are used here, with interaction events for both boundaries being studied. Cells that come within a threshold of $l_t = 100\mu$m from the wall are only considered. From the results of Kanstler *et al* [30], it is apparent that the cells tend to contact the wall with their flagella when close to it and for this purpose, it is necessary to define a region where such contact can take place. The contact region is chosen to be approximately two body lengths ($l_c = 20\mu$m) from the wall. The reason for choosing this length is to account for possible flagellar contact, as the length of the flagella is approximately the same as the body. The orientation of the cell with respect to the wall is determined as illustrated in Figure 4.15. Here, θ refers to the orientation of the cell with respect to the wall. A positive θ implies an orientation towards the top wall while a negative θ implies an orientation towards the bottom wall.

The tracks which reach these limits are then selected. The trajectories for the TRIS case are similar to that obtained by Muller [19], and some of these trajectories will be discussed in Appendix G. The

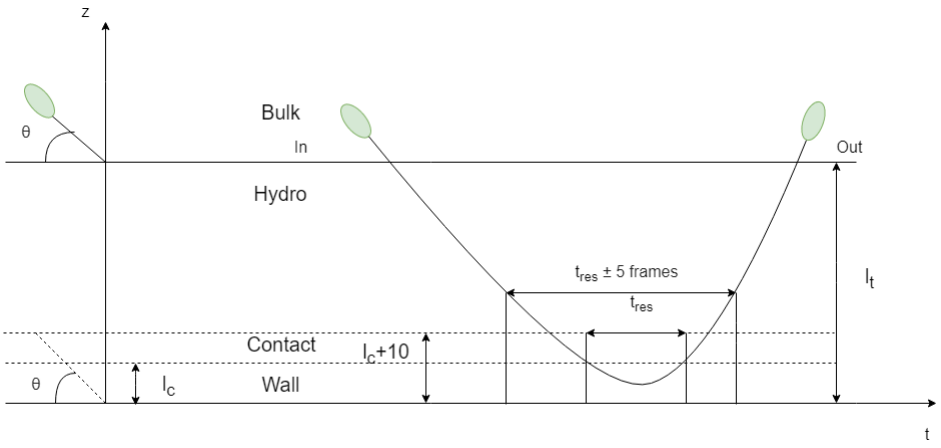

Figure 4.15: Illustration depicting how cell-wall interactions are defined and how certain parameters are calculated

trajectories for the 3 cases are plotted in Figures 4.16, 4.17 and 4.18. As mentioned in section 4.4.1, the tracks from the 12.5 % Ficoll are noisier than the rest. This implies that there are less completed tracks to plot and discuss, and this is especially so for the wall scenario. Therefore, there are no trajectories plotted for the Ficoll 12.5 % case.

The plots on the left-hand side of Figures 4.16, 4.17 and 4.18 depict the trajectory of the track near the wall. In this case, $z = 0$ represents the wall, with positive values of z indicate the track moving towards the top wall and negative indicating the track moving towards the bottom wall. The colour codes represent the velocity of the tracks and for many tracks, it is apparent that the velocity reduces once it enters the contact region. The plots on the right-hand side represent the variation the height (l_d) with time (t), with the colour codes representing the orientation with respect to the wall. All the trajectories here are only concerned with the contact region, although some of these trajectories occur outside the contact region as well.

The top two rows of the figures represent the phenomenon of reflection. Here, the cell comes into the contact region, spends some time there, and then leaves the contact region. If the angle at which it enters and leaves are similar, the phenomenon is termed as symmetric reflection (Figures 4.16a, 4.17a, 4.18a). If it isn't the case, then it is asymmetric reflection (Figures 4.16b, 4.17b, 4.18b). The third row represents the tracks that circle (Figures 4.16c, 4.17c) or move in a complex, helical fashion (Figure 4.18c) around the wall region, and the fourth row depicts the phenomenon of bouncing (Figures 4.16d, 4.17d and 4.18d) near the wall region. In addition to these trajectories, the phenomenon of wall-bound wobbling is also common. All these interactions have been reported by Muller [19] as well, so the overarching trajectories and interactions near the wall are still retained by the cells regardless of the fluid, with the only exception being the absence of circling for the 250 ppm PASA solution.

(a) Symmetric Reflection

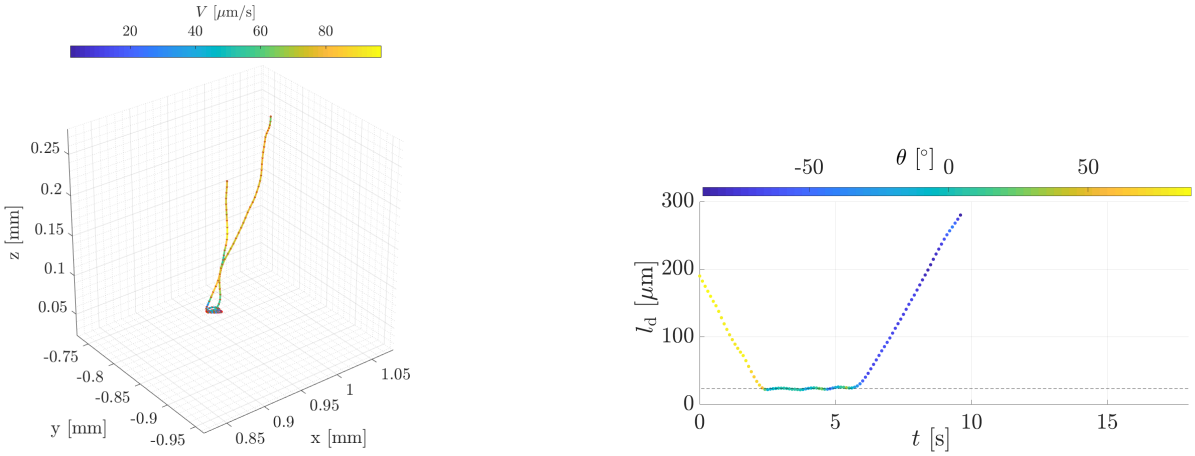

(b) Asymmetric Reflection

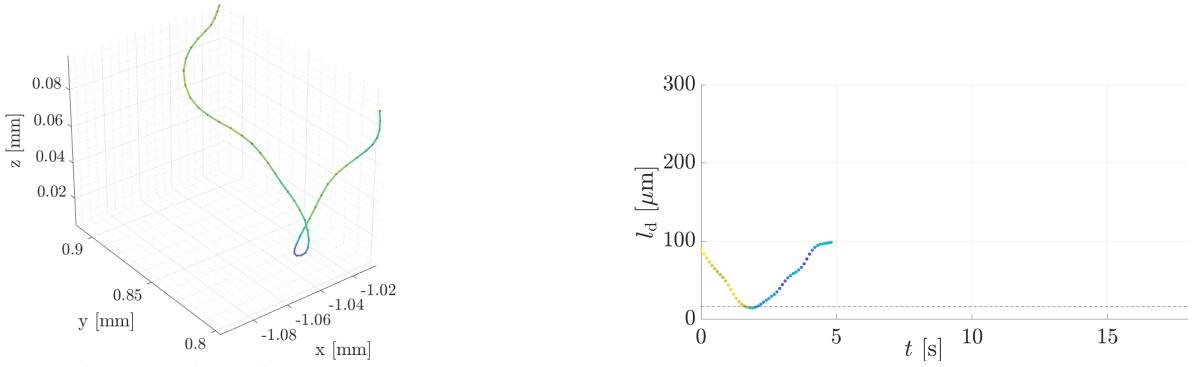

(c) Circling near the wall

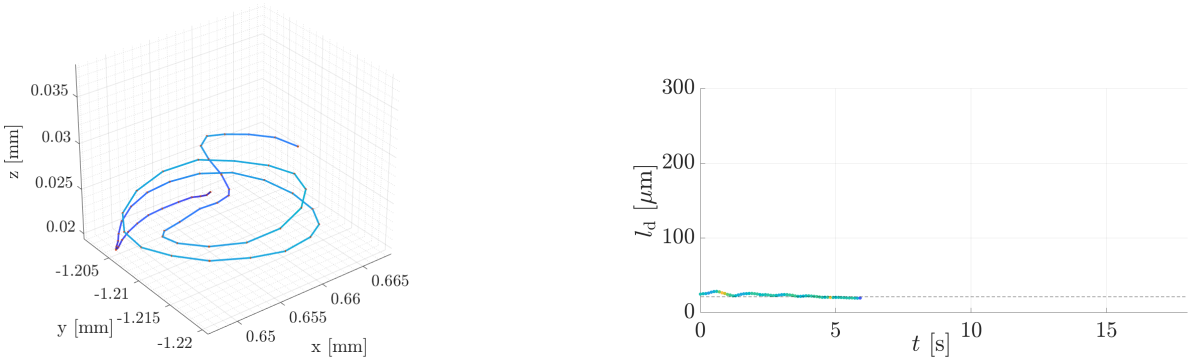

(d) Repeated wall bouncing

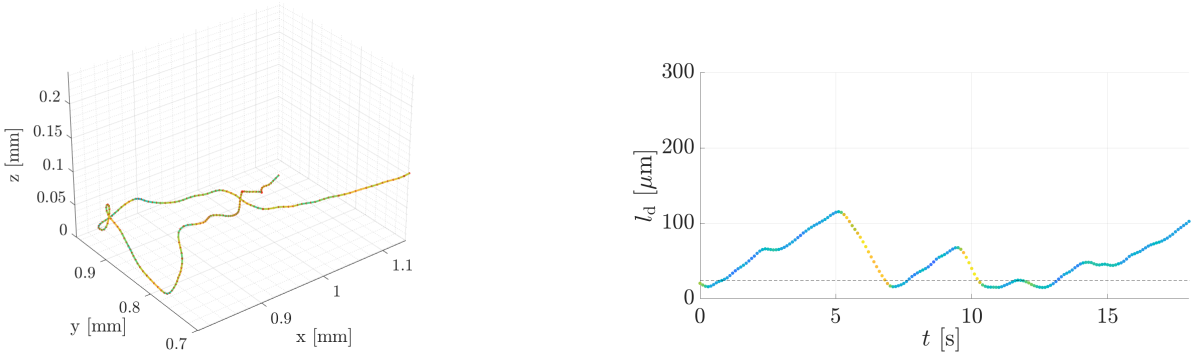

Figure 4.16: Typical trajectories found near the wall for 150 ppm PASA. The dashed black line in the 2D plot indicates the contact region

(a) Symmetric Reflection

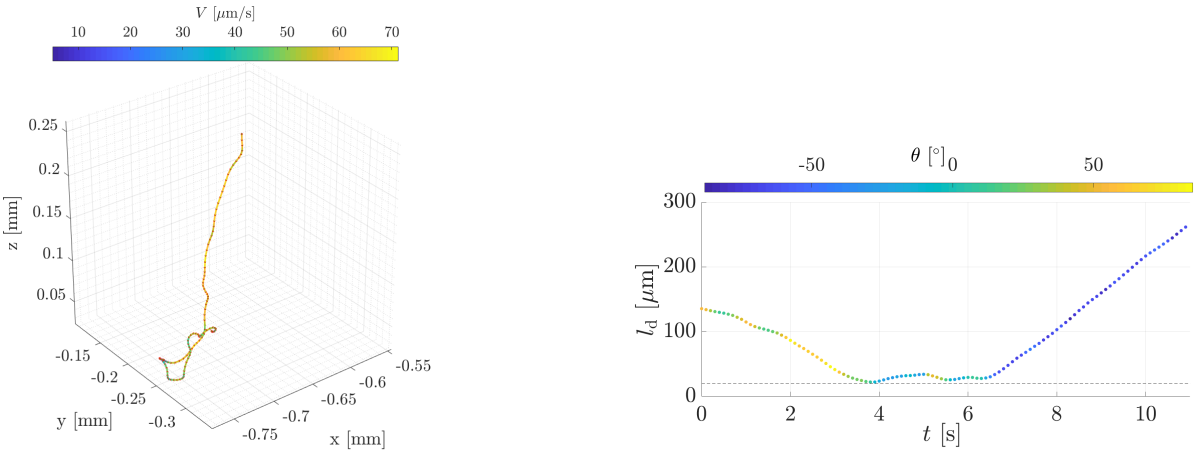

(b) Asymmetric Reflection

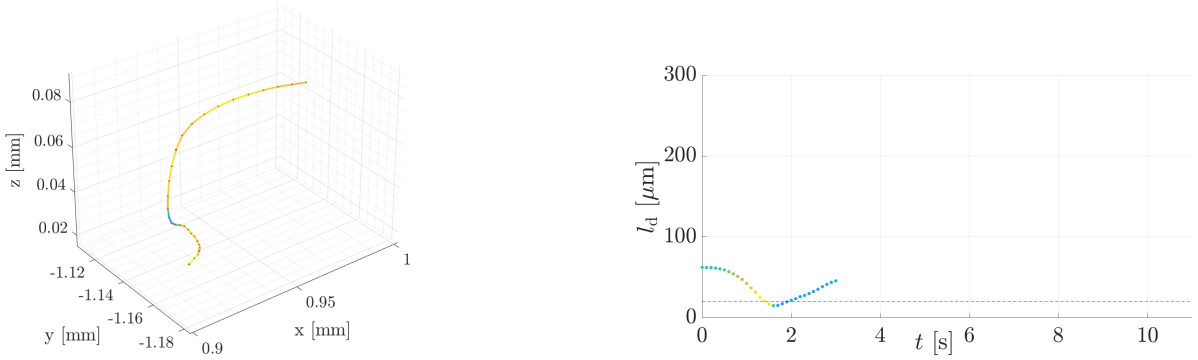

(c) Circling near the wall

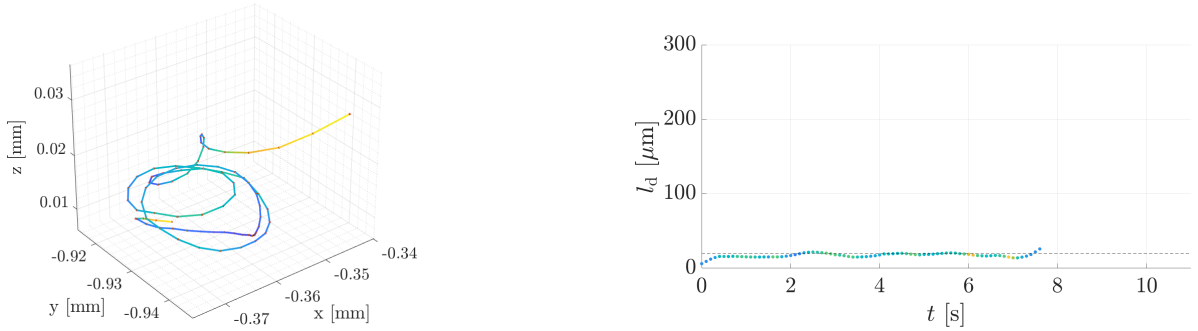

(d) Repeated wall bouncing

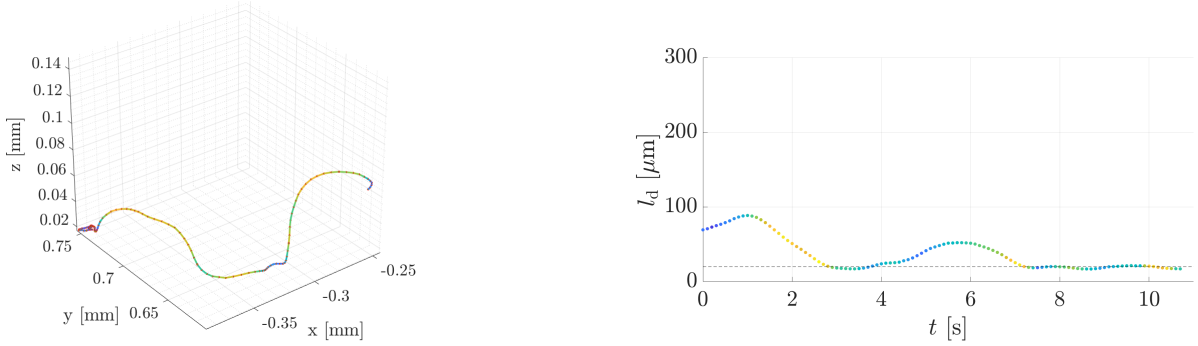

Figure 4.17: Typical trajectories found near the wall for the 7 % Ficoll solution. The dashed black line in the 2D plot indicates the contact region

(a) Symmetric Reflection

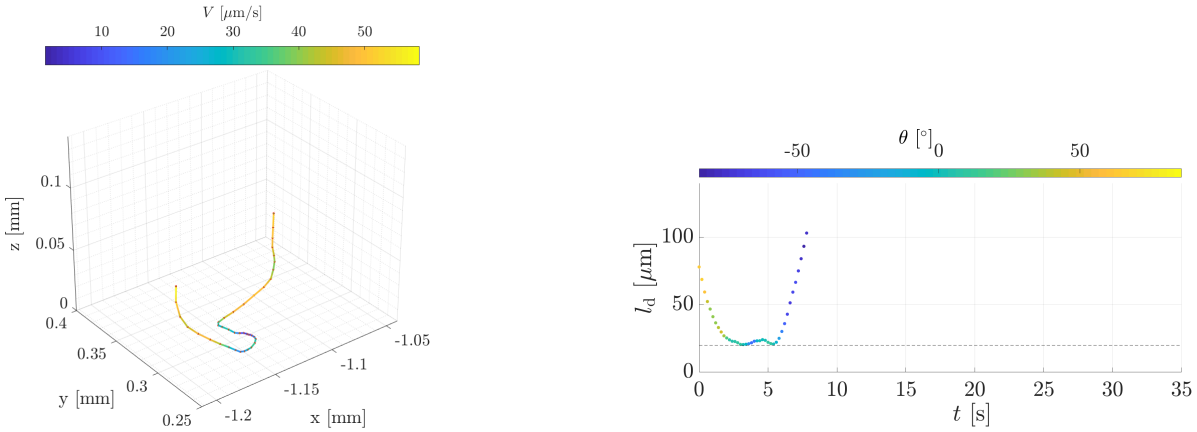

(b) Asymmetric Reflection

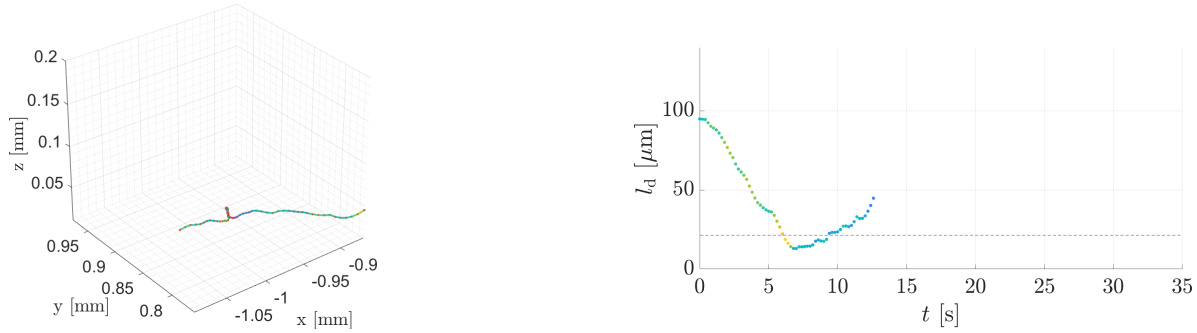

(c) Helical wall bound wobbling

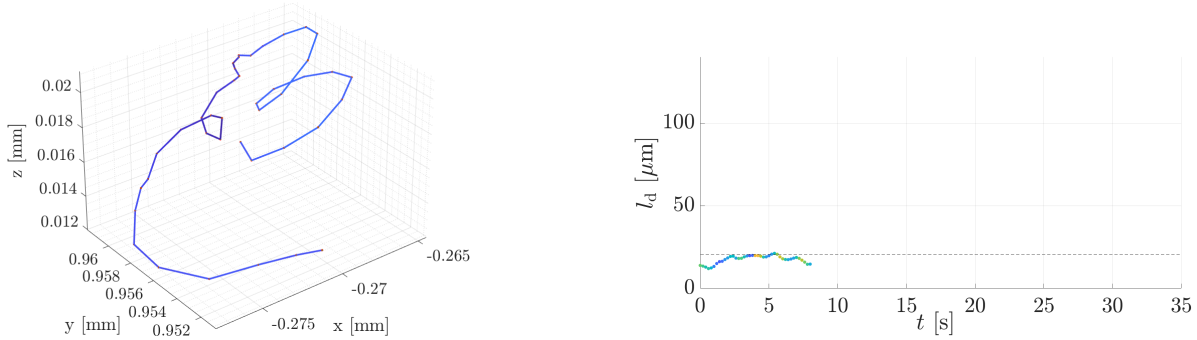

(d) Repeated wall bouncing

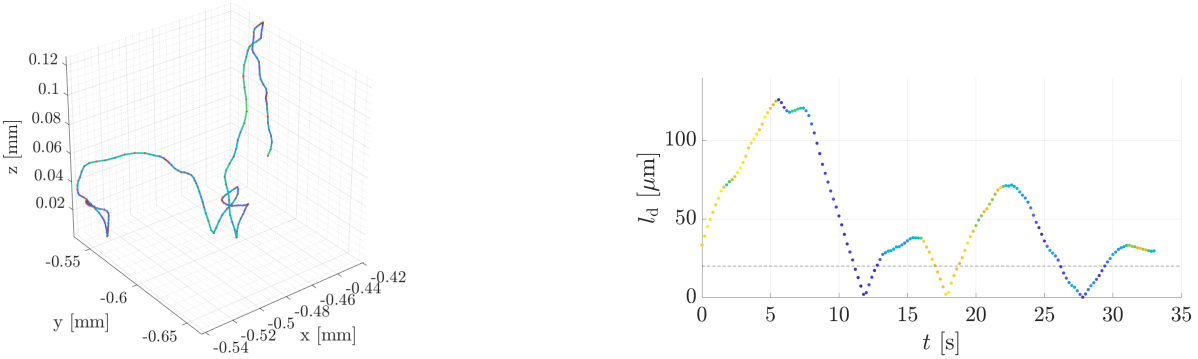

Figure 4.18: Typical trajectories found near the wall for 250 ppm PASA. The dashed black line in the 2D plot indicates the contact region

4.4.3. Interactions and reflections

In this portion, the focus is on explaining the possible cell-wall interactions through graphs and statistics, with a greater emphasis on the phenomenon of reflection. As mentioned before, the idea is to understand the contact and hydrodynamics observed near the wall. From the graphs in section 4.4.1, it is evident that there is a greater accumulation near the wall for all the cases, except for the Ficoll 12.5 % solution, which will not be discussed in detail. Probing further, the minimum distance in the z-direction (l_{min}) for all the wall-bound tracks (those that come within a distance of l_t) are plotted (Figure 4.19) for the 5 cases to observe if there is a tendency to go towards the contact region. Interactions near both walls are considered as discussed before. For the solutions of lower viscosity (TRIS,150 ppm PASA and Ficoll 7 % solutions), there is a significant accumulation at a distance of $\sim$ l_c from the wall, but the accumulation is left of l_c for the more viscous 150 ppm PASA and Ficoll 7 % solutions unlike the TRIS case. The cells tend to move near the wall and continue their motion. But for the more viscous solutions (250 ppm PASA and Ficoll 12.5 %), there is, surprisingly, maximum accumulation of cells at the wall. From these graphs, it can be deduced that the cells tend to go closer to the wall with higher viscosity.

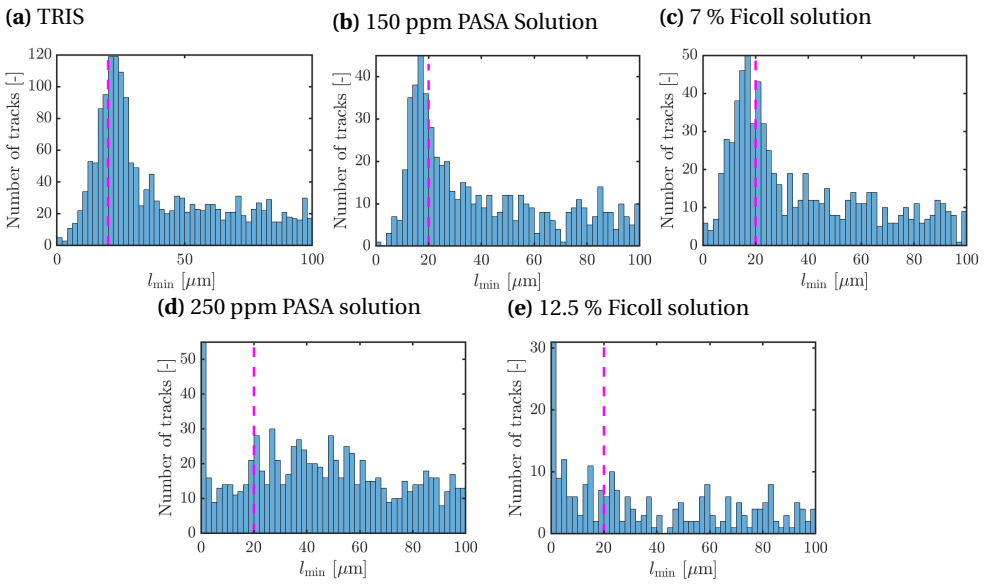

Figure 4.19: Minimum distance of wall-bound tracks. The purple dashed line indicates the contact region

We move on towards the phenomenon of reflection in the wall-bound region, and this can be segregated into two categories- tracks that come within 30 μm from the wall, and those that don't. 30 μm is chosen as the region of possible contact instead of 20, primarily to account for wobbling around l_c and uncertainties in the estimation of wall location. To characterise reflection, the incoming and outgoing angles and the residence times are some of the parameters studied for both contact and non-contact regions. The residence time, t_{res} is defined as the time cell spent by the cell in the contact region from entry to exit. In the case of reflections with no contact, the residence time is defined as the time spent by the cell in the region within 10 μm of the minimum height from the wall reached by it. To calculate t_{res}, there are naturally certain caveats to be wary of. Tracks which start at the contact region can't be chosen as the events preceding the encounter are unknown. The procedure for selecting and calculating the residence times is illustrated in Figure 4.15 for contact cases, and for no contact, it is illustrated in Figure 4.20. Only the tracks that are present for at least 5 frames before and after the event occurs are considered. The incoming and

outgoing angles are determined as the mean angle of these five frames. After these conditions are satisfied, the residence times are calculated and plotted for all the cases except for the Ficoll 12.5 % solution, for reasons mentioned previously. From the results in Appendix E, the cells do not swim at a fixed velocity but over a range. The residence times might be affected by the velocity at which the cell swims and this might lead to a misinterpretation of the results. To allow easier analysis of the results so as to focus only on the wall interactions, the residence times are normalised in such a way that $t^*_{\mathrm{res}} = \frac{t_{\mathrm{res}} V_{\mathrm{t}}}{V_{\mathrm{m}}}$, where V_{t} is the median velocity of the track and V_{m} is the mean velocity of all the cells. Therefore, all the residence times are contextualized in terms of the mean velocities of the cells. Both contact (Figure 4.21) and non contact (Figure 4.22) regions are considered.

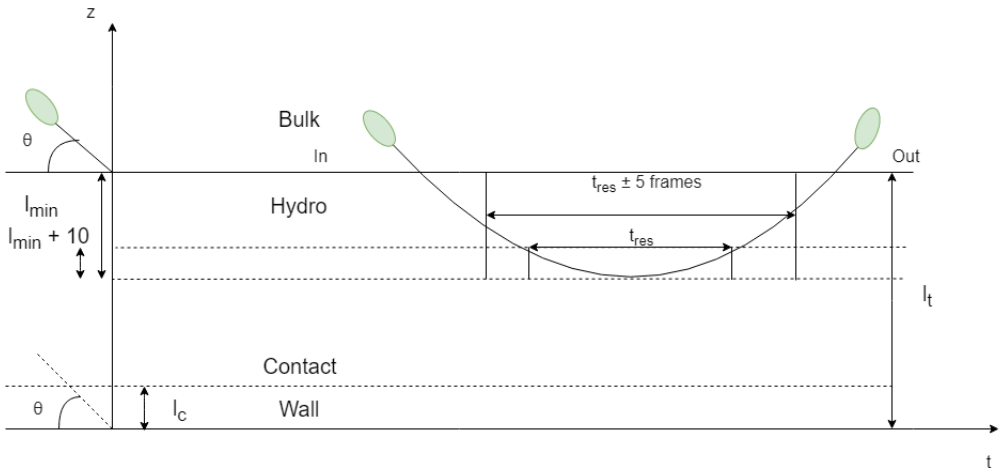

Figure 4.20: Illustration depicting how cell-wall interactions are defined for tracks that do not touch the contact region

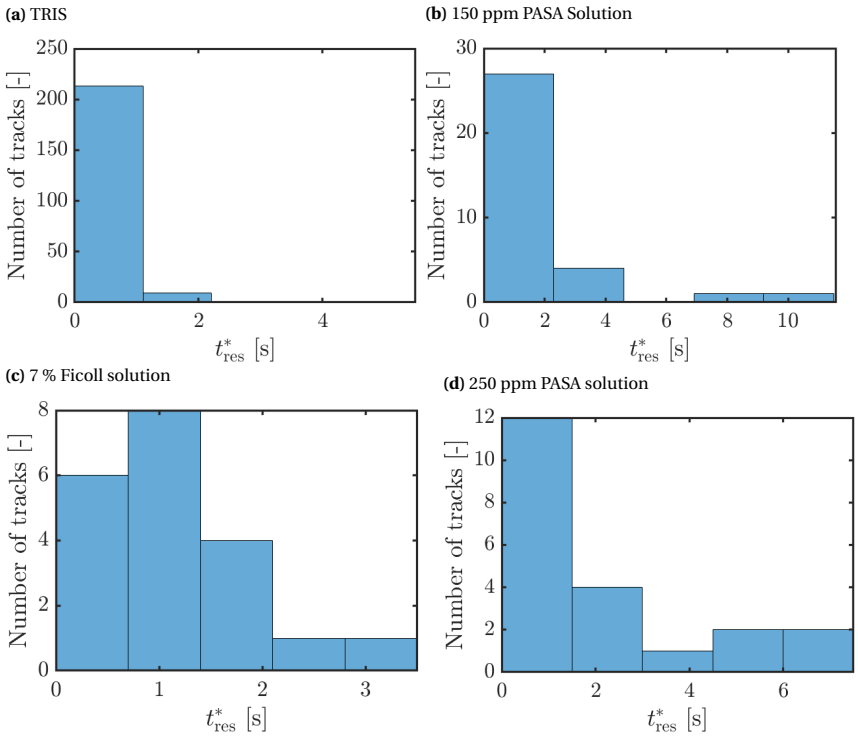

Figure 4.21: Residence times of all the tracks that come near the contact region

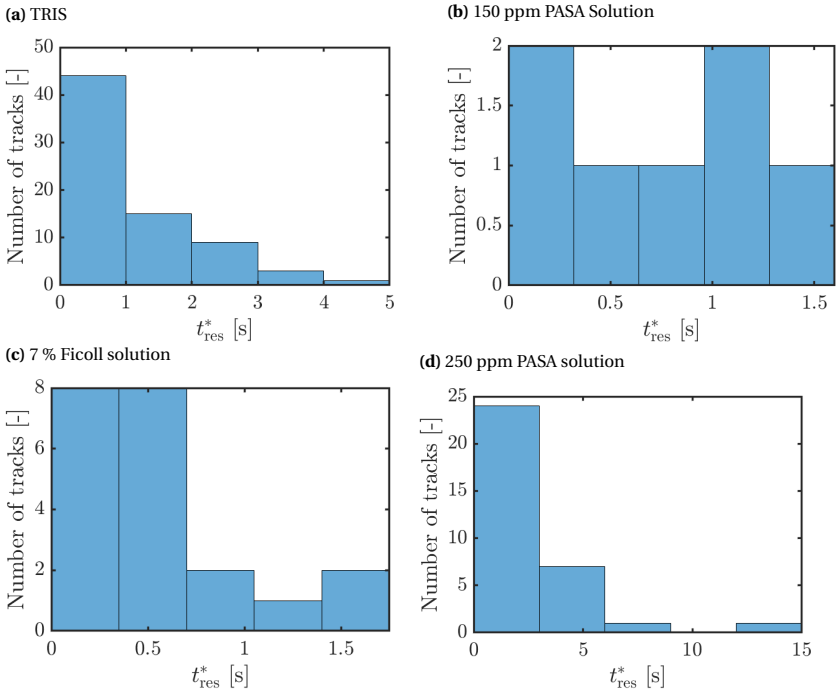

Figure 4.22: Residence times of all the tracks that do not come near the contact region

The maximum number of tracks that satisfy our conditions is for the TRIS case. Since it is difficult to determine the residence times for such a small number of bins, the median residence time is determined. The number of bins is small as there are fewer completed tracks in the other solutions. The median residence time is around 0.45 seconds for the contact scenario (Figure

4.21a), whereas the residence time in the non-contact scenario (Figure 4.22a) is a little higher, with the median around 0.75 seconds. For the rest of the cases, the number of tracks that satisfy the conditions is appreciably lower, with the number not exceeding 36 tracks for any of the cases. Tracks with long residence times are observed for the contact scenario in the 150 ppm PASA case (Figure 4.21b), with the bulk of the residence times concentrated around 1 s. The median residence time is 1.5 seconds in this case. In the case of the 7 % Ficoll solution, the residence times near the contact region (Figure 4.21c) are more evenly distributed, with the median residence time around 1.1 seconds, slightly lower than the 150 ppm case. In the 250 ppm PASA case (Figure 4.21d), the residence times near the contact region are also concentrated at around 1 second. There are fewer tracks for the non-contact scenarios in the 150 ppm PASA and 7 % Ficoll cases, but for the 250 ppm PASA solution, there are more completed tracks. The residence times in the non-contact scenarios are smaller for the 150 ppm PASA and Ficoll 7 % cases, with the median around 0.75 seconds in 150 ppm PASA and 0.5 seconds in the 7 % Ficoll solution. The 250 ppm PASA case seems to buck the trend, with the residence times for the non-contact scenario being around 1.6 seconds. It is difficult to draw any conclusions, however, as there are few tracks for all the cases of higher viscosity.

The residence time represents only one facet of wall interaction. To characterise the behaviour of the cells near the wall, the incoming and outgoing angles in the contact and non-contact regions are determined for all the cases except for the Ficoll 12.5 % case. The incoming angle, θ_{in}, is determined as the mean angle of the five frames before the cell enters the contact region, as shown in Figures 4.15 and 4.20. The outgoing angle, θ_{out}, is defined as the mean value of the angles in five frames after the cell leaves the contact region.

To probe further into the reflections, a 2D histogram of θ_{in} and θ_{out} in the contact and non-contact regions are plotted in Figures 4.23 and 4.24 respectively , with the colour bar indicating the relative density. Here, the outgoing angle corresponding to the incoming angle is plotted, allowing to characterise if symmetric or asymmetric reflection is the dominant phenomenon. The results for TRIS in the contact region in Figure 4.23a seem to point towards asymmetric reflection , with θ_{in} being steep and θ_{out} shallow. The incoming angles are concentrated around 60-70 °, with the most common outgoing angles around 40-50 °. Symmetric reflection isn't entirely uncommon, with a significant number of tracks exhibiting it. The histogram for the non-contact region (Figure 4.24a) indicates a mild reversal of this trend, with θ_{out} being steeper than θ_{in}. Although the angles are more evenly distributed here, asymmetric reflection again appears to be the dominant phenomenon, with θ_{in} ranging from 5-20° and θ_{in} ranging from 20-50°.

Asymmetric reflection is the dominant phenomenon near the contact region for both 150 ppm PASA and 7 % Ficoll solutions (Figures 4.23b and 4.23c respectively), albeit with lower θ_{in} and θ_{out} for the Ficoll case. The incoming angles are still steep, ranging from 60-80° for 150 ppm PASA and 50-60° for the 7 % Ficoll solution. The outgoing angles in both cases range from 5-30°. Asymmetric reflection is the dominant phenomenon near the contact region even for the 250 ppm PASA case (Figure 4.23d), but there's no discernible trend for the incoming and outgoing angles, with both assuming steep and shallow values.

For reflections outside the contact region, symmetric reflection appears to be the more common interaction for the 150 ppm PASA (Figure 4.24b), whereas asymmetric reflection is dominant in the 250 ppm PASA case (Figure 4.24d). A steady mix of both interactions is observed in the 7 % Ficoll solution (Figure 4.24c). The incoming angles are surprisingly steep for the 250 ppm PASA case, mirroring the results near the contact regions for the rest of the cases. It is worth reminding that all these results presented are only for small sample sizes, so any trend observed is

not necessarily an indication of overall cell behaviour.

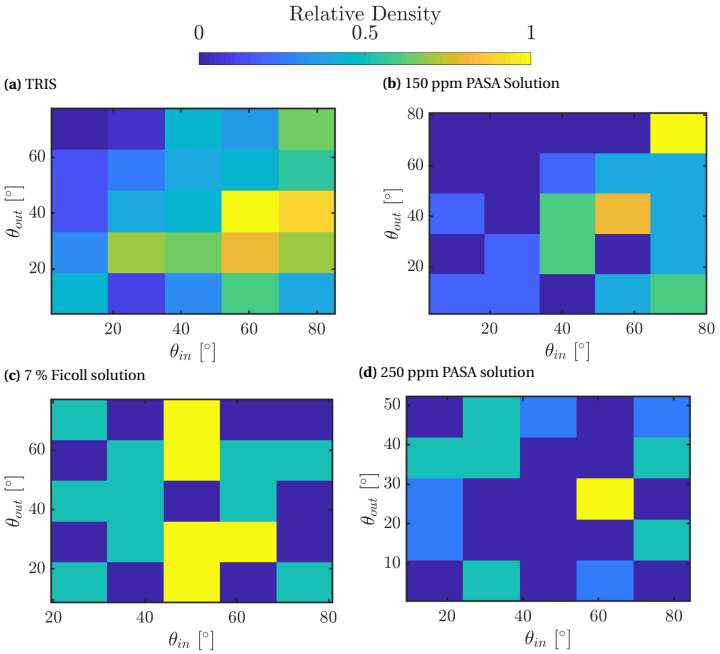

Figure 4.23: 2D Histogram representing the relationship between incoming and outgoing angles for tracks that come near the contact region

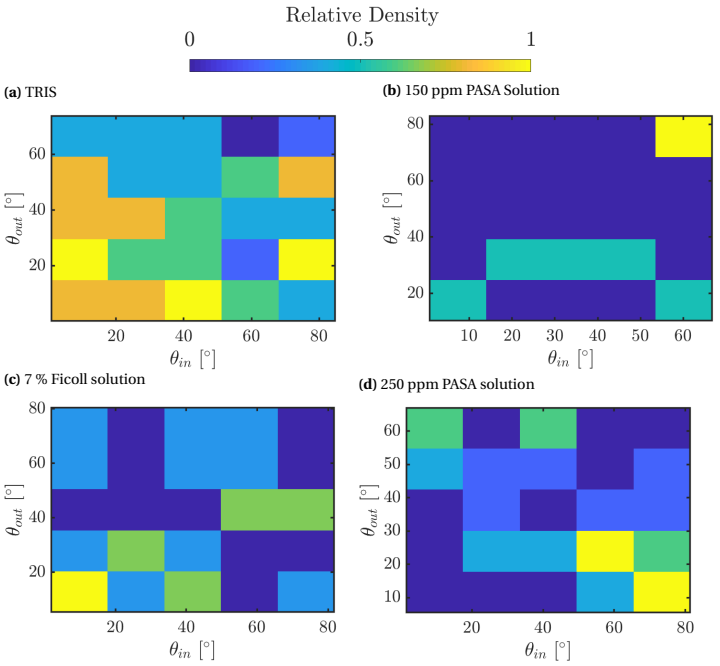

Figure 4.24: 2D Histogram representing the relationship between incoming and outgoing angles for tracks that do not come near the contact region

Since there aren't many tracks to analyse for all the cases except TRIS, analysis of the trajectories near the wall might give a much better picture of the underlying phenomenon. Tracks that are within 30 μm from either of the walls are considered for all the 5 cases. The minimum height z_0

reached by all the tracks are determined. x_0 and y_0 are the coordinates along the x and y axes corresponding to z_0. t_0 is the time at which the track reaches z_0. These values are set as the datum for each track. All the tracks are truncated in such a manner that there are only the points that lie within 1.5 seconds on either side of this datum. To plot the trajectories in 2D, the spatial path travelled along the x and y axes, x_{2D} is subsequently determined according to Equation 4.1. x_2 and x_1 refer to the current and the previous point. Once x_{2D} is determined, all these values are subtracted from x_{2D} (t_0) at the datum. The height is normalised by the diameter of the cell (z^*), which has a value of around 10 μm. z^* is plotted against (x_{2D} -$x_{2D}(t_0)$) as a contour plot to observe how the cells tend to swim near the wall for all the 5 cases in Figure 4.25. The black circles in each figure represent the mean trajectory followed by the cell near the wall. The mean trajectories in all fluids are plotted separately in Figure 4.26.

$$x_{2D} = \sqrt{(x_2 - x_1)^2 + (y_2 - y_1)^2} \tag{4.1}$$

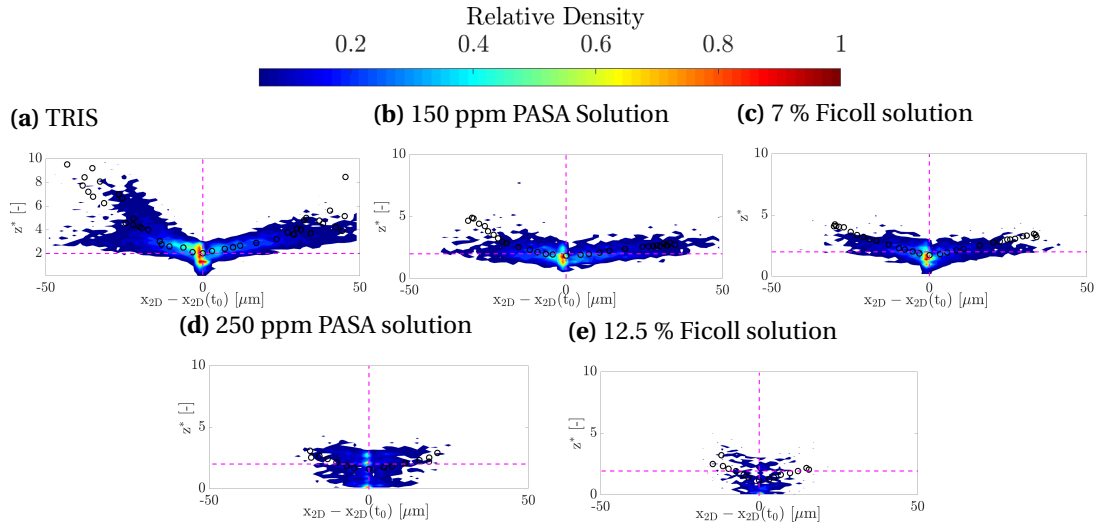

Figure 4.25: Nature of cell trajectories that come near the contact region. The horizontal purple dashed line represents the contact region and the vertical purple dashed line represents the datum.

The contour in Figure 4.25a for the TRIS case indicates a bimodal distribution on the left side of the datum, where the tracks enter at steep and shallow angles. On the right side of the datum, there appears to be only a single path as it leaves the wall. This implies the presence of both symmetric and asymmetric reflections. The mean trajectory corresponds to an asymmetric reflection, implying a greater tendency for the cells to enter at steep angles and leave at shallow angles, corroborating the results obtained in Figure 4.23a.

The spatial paths covered by the cells would naturally be smaller for the more viscous cases as the velocities are slower. Also, the tendency of the cells to hover around the wall region increases with increasing viscosity. Interpreting the contours in all these cases is not straightforward because of the lower speeds and clustering around the wall region. To analyse the wall interactions better, the mean trajectories are discussed.

In case of the 150 ppm PASA solution, the behaviour observed in TRIS is still retained, although the incoming angle is shallower than the TRIS case. The mean trajectory in the Ficoll 7 % solution also indicates the tendency of the cells to gravitate towards asymmetric reflection, but the incoming angle is a lot shallower than the 150 ppm PASA case. The incoming angles for the 250 ppm PASA and 12.5 % Ficoll cases are similar to those in the Ficoll 7 % case, but the behaviour is

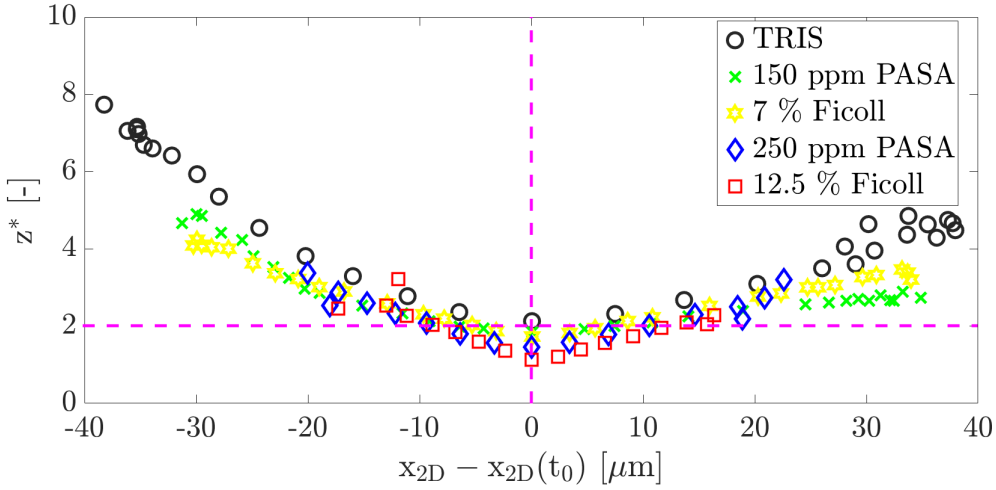

Figure 4.26: Mean Trajectories followed by cells in TRIS (black circles), 150 ppm PASA (green cross), 7 % Ficoll (yellow star), 250 ppm PASA (blue diamond) and 12.5 % Ficoll (red square) solutions. The horizontal purple dashed line represents the contact region and the vertical purple dashed line represents the datum.

more symmetric.

According to Contino *et al* [31], both contact and hydrodynamic interactions are possible near the wall for the TRIS case. Since there is no view of the flagella, it is difficult to differentiate between the two interactions. From Figures 4.16 and 4.17, a drop in velocity is observed for some of the tracks once they enter the contact region. To see if this is something common, the velocity magnitudes normalised by the mean cell velocity (V^*) of all the wall-bound tracks are plotted against the height as a 2D histogram for all the 5 cases in Figure 4.27. The colour bar represents the relative density in this case.

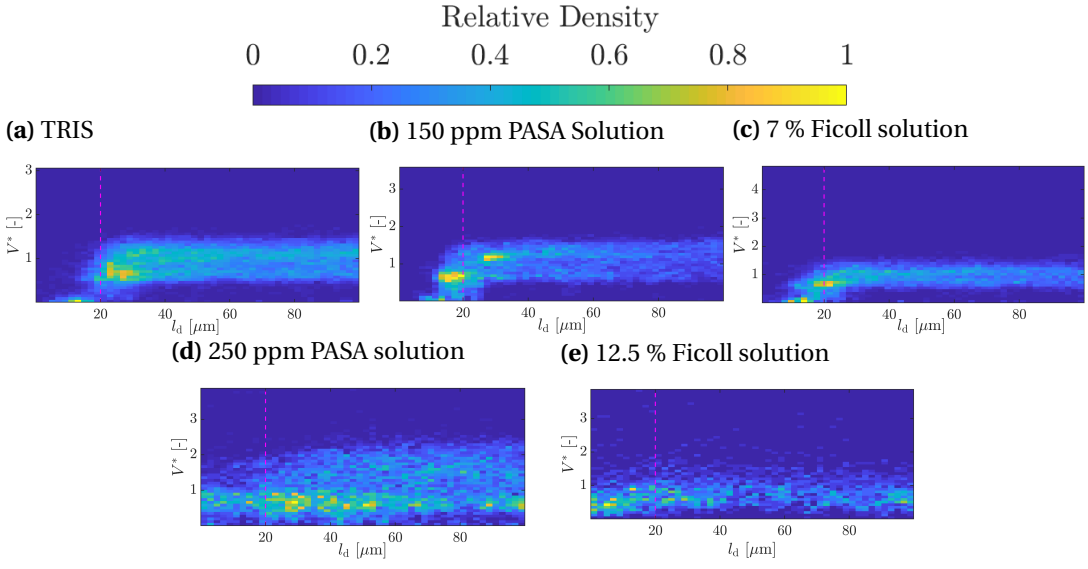

Figure 4.27: 2D histogram depicting the relationship between the height and the non-dimensionalised for wall-bound tracks. The purple dashed line indicates the contact region.

From Figure 4.27a, it is evident that the velocity magnitude plummets once the cell comes

into the contact region in TRIS. This perhaps serves as an indication of the cell touching the wall, leading to a reduction in velocity, though the influence of hydrodynamics shouldn't be neglected. The histograms for 150 ppm PASA and 7 % Ficoll solutions show a trimodal distribution instead of the bimodal distribution shown in the TRIS case. The velocities in the contact region do not drop as drastically until a distance of around 10 μm, with many cells swimming at the same velocity as the mean until this distance is reached. As we move on to more viscous solutions, the histograms become less clear. The drop in velocity in the contact region for both the 250 ppm PASA and 12.5 % Ficoll cases isn't apparent. The bins that point to low velocities are also present outside the contact region. The only evidence that points to a reduction in velocity is the absence of the higher velocities in the contact region.

While all these results show a zoomed-in picture of the interactions near the wall, the overall behaviour of the cells as they move towards the wall from the bulk isn't clear. To see if more information can be obtained for the overall behaviour of the cells toward the walls, the orientation of the cell with respect to the wall is plotted against the height normalised by the cell diameter over the entire domain, z^*, in Figure 4.28 for all the five cases. A positive angle indicates the movement towards the top wall while a negative angle indicates the movement towards the bottom wall. Since many cells tend to concentrate near the wall region, a 2D histogram with relative density as a colour bar doesn't give a clear picture of the general behaviour. A track can have multiple points in each bin, and this is particularly so near the wall, where the cells tend to stay for some time. This might skew the results and lead to a possible misinterpretation. To avoid all this, it is ensured that a track can have only one point in each bin. The rest of the points are removed. This is repeated for all the tracks. The colour bar in the figure represents the probability that a cell assumes a specific orientation in a particular z^* bin.

From Section 4.4.1, it was shown that there is less data at the bottom wall as compared to the top wall. Since it is difficult to comment with less data, most of the comments will be restricted mainly to points above $z^* = 100$. In the TRIS case, the tendency of the cells to enter the wall at steep angles and leave at shallow angles is observed. This is evident from the right-hand side of the plot, with the density pointing to data concentrated at steep angles. This is consistent with the results of Figure 4.25a. Around $z^* = 150$ and at the left-hand side of the histogram (the side with negative angles), there are quite a few cells that start moving towards steeper angles from the shallower angles. This implies that there is a possibility of cells following this behaviour for the bottom wall as well, although there isn't sufficient data to show for it. At 5 cell diameters from the wall, most of the cells tend to swim at angles ranging from -20 to 20°. This is probably due to any contact or hydrodynamics occurring near the wall region.

For the 150 ppm PASA, the movement of cells towards the upper wall still occurs at steep angles, with the leaving angles shallower than the incoming angles. This behaviour is apparent only above $z^* = 100$, and the switch from shallow to steep angles as in the TRIS case is not observed. In case of the Ficoll 7 % solution, the entrance angles are shallower, being around the range of 40-50°, and the leaving angles are also steeper. The cells tend to assume an orientation that is more evenly distributed and symmetric than the previous two cases. Surprisingly, some of the cells in the 250 ppm PASA case still appear to retain the steep angle movement towards the upper wall, although the bulk of the entrance and exit angles are shallow. The distribution still appears to indicate symmetric reflections. From the 12.5 % Ficoll histogram, it is difficult to draw any conclusions as the data appears to be dominated by noise.

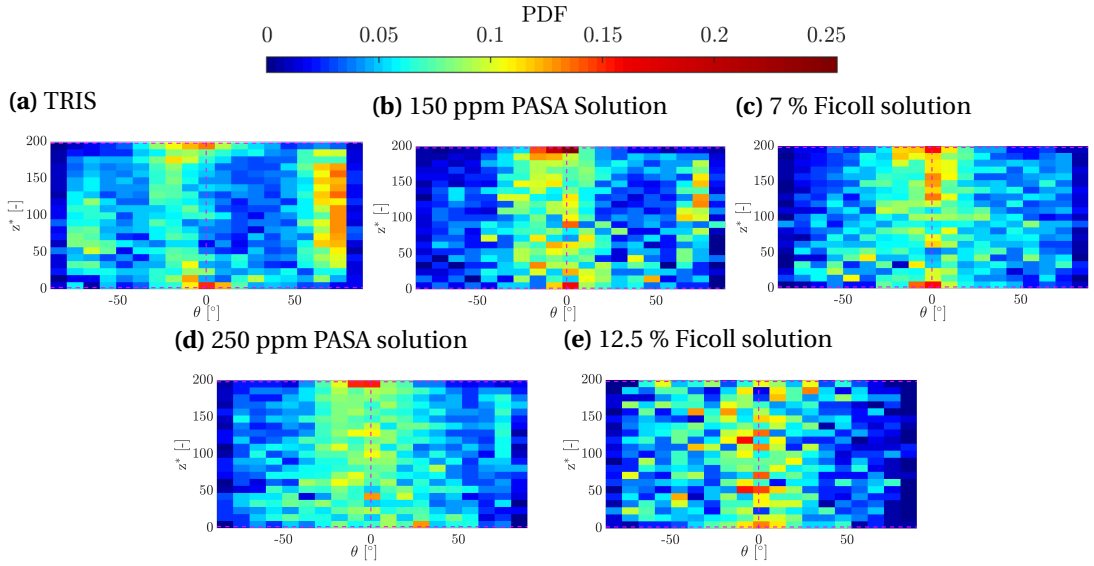

Figure 4.28: 2D histogram of the orientation of the cell with respect to the wall against the normalised height of the domain. The two horizontal purple dashed lines indicate the position of the upper and lower contact regions. The vertical purple dashed line separates the histogram into two halves- the points on the right-hand side that are oriented towards the upper wall and those on the left-hand side that are oriented towards the bottom wall.

Delving deeper, the gradual attraction of the cells toward the walls caused by any hydrodynamic forces is studied. Inspired by the results from Berke et al [24], the angular velocities of the cells with respect to the wall is determined. The angular velocity, ω, is determined by the formula:

$$\omega = \frac{\mathrm{d}\theta}{\mathrm{d}t} \tag{4.2}$$

where θ is the orientation of the cells with respect to the wall and t is the time. Berke modelled *E.Coli* as a force dipole with the propulsive and drag force as the equal and opposite forces. In the absence of any hydrodynamic forces, the average rotation rate and attraction to the walls over the entire population will be equal to zero. But these results are valid only for viscous fluids, where there are only two forces- propulsive force and viscous drag. In viscoelastic fluids, there is an additional complexity introduced by the presence of the elastic forces [27, 53]. To verify if hydrodynamic attractions have any role to play and observe the possible changes a viscoelastic fluid might induce, a contour plot involving the orientation with respect to the wall and z^* is plotted. While the colour bar indicated the probability that a specific orientation is assumed for a particular z^* in Figure 4.28, here it represents the mean angular velocity in each bin. A track is ensured to have only point in each bin using the procedure as in Figure 4.28. The angular velocity in each bin represents the mean angular velocity of all the points in the bin.

The results from Figures 4.28 and 4.4.1 show the lack of data near the bottom wall. Instead of discarding the data entirely, all the points below z^*=100 are combined with the points above, thereby displaying one wall instead of two. Here, z^*=0 represents the walls and z^*=100 represents the centre of the entire domain. Since there are more cells near the top than the bottom wall, the mean angular velocity for each bin is calculated based on the following equation:

$$\omega_\mathrm{m} = p_1\omega_1 + p_2\omega_2 \tag{4.3}$$

where ω_m is the mean angular velocity corresponding to each bin, ω_1 is the angular velocity for the

bin above the centre and ω_2 is the angular velocity for the bin below the centre of the domain, p_1 and p_2 being the percentage of points in the bins above and below the centre of the domain. After calculating the angular velocity, the results are plotted in Figure 4.29. A positive angular velocity indicates pitching towards the walls. The 12.5 % Ficoll solution is not considered in this case because of the presence of noise. The white spaces in these plots indicate unusually large angular velocity magnitudes that are probably caused because of noise.

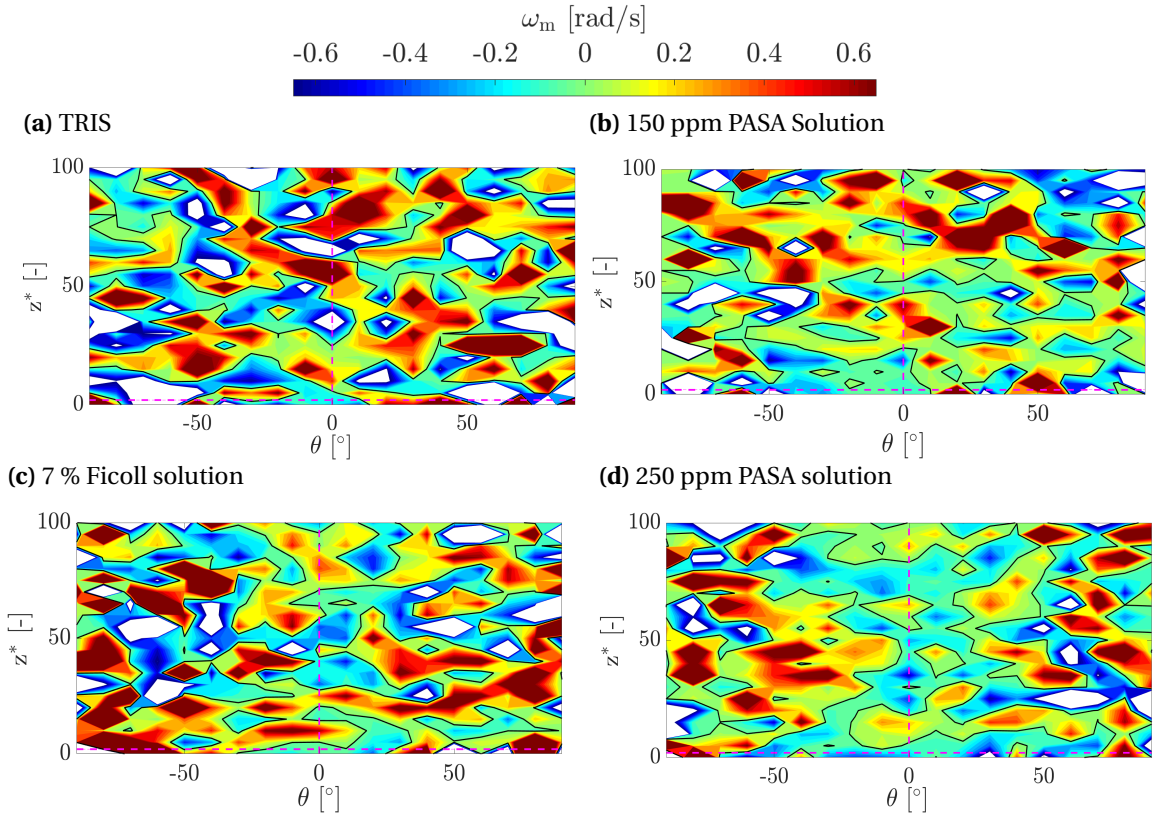

Figure 4.29: Contour plot of the orientation of the cell with respect to the wall against the normalised height of the domain with the colour bar representing the mean angular velocity in each bin in rad/s. The horizontal purple dashed line indicate the position of the contact region. The vertical purple dashed line separates the histogram into two halves- the points on the right-hand side that are oriented towards the walls and those that aren't.

The results from these histograms are inconclusive, to say the least. For the TRIS case, though the overall angular velocities are not zero, there isn't any clear indication that the cells tend to pitch at steep angles towards the walls, except for the high angular velocities at around z^*=20. The leaving at shallow angles isn't captured either. This is probably because of the lower sample size presented, making noise dominate the results. But it does not mean that the plot does not give an indication of cell behaviour. The right-hand side of the plot shows a tendency to go towards the wall since the angular velocities are largely positive throughout. The left-hand side, on the other hand, points to an overall neutrality in the angular velocity, implying that the cells tend to move towards the wall for the TRIS case, though the overall behaviour of the incoming and outgoing angles aren't captured.

The contours for the more viscous cases are a lot murkier to interpret. Though it appears that the mean angular velocity is not zero for all the cases, the behaviour represented by these contours doesn't corroborate with the previous figures. The angular velocities seem to be neutral

on both sides in the 150 ppm PASA case, and this is even apparent in the 250 ppm PASA case. For the Ficoll 7 % solution, the angular velocities are largely positive regardless of the orientation, implying that the cells tend to move towards the wall always. It might be easy to dismiss this data as noise, especially since the overall behaviour is not captured in TRIS, but as the previous plots have shown, the cells tend to exhibit different behaviours in more viscous and viscoelastic solutions. Additionally, the cells showed a tendency to pitch towards the wall in TRIS, making a good case to not entirely rule out the plots for the other solutions. Perhaps a lot more data is required before anything concrete can be said about the hydrodynamics.

5
Discussion

The aim of this chapter is to contextualize the obtained results using existing literature and to perhaps understand and explain the possible reasons for the observations. The first section focusses on the kinematics and velocities of the cells in Newtonian and viscoelastic fluids, while the second section seeks to understand the cell-wall interactions in all the fluids. Since the flagellar action cannot be seen during the experiments, this report will hypothesize the obtained results using the results from simulations and experiments that present a closer view of the flagella.

5.1. Kinematics

The results from Section 4.3.1 show a clear reduction in velocity with an increase in viscosity. This is expected as the viscous drag increases with an increase in viscosity, thus slowing the cells. The accuracy of the results is confirmed by comparing it with the results obtained by Qin *et al* [52] for the Ficoll solutions. The difference in the values is possibly related to the different experimental conditions and culturing methods used. Qin *et al* [52] conducted the experiments in water, not TRIS like our case, and the culturing procedures were not exactly the same as those established by Quaranta *et al* [78]. Additionally, they worked with a small number of cells instead of a suspension like our case. The results, though similar qualitatively, is indicative of how important culturing and experimental conditions are when it comes to comparative studies.

The presence of an elastic component introduces an additional complexity to the results. The velocities of the cells in viscoelastic fluids are lower than those in Newtonian fluids, and this result is consistent with those observed in experiments by Qin *et al* [52] on *C.Reinhardtii* and in simulations [27] for pullers. Qin *et al* reasoned that this was because of the bending of the distal tip in a viscoelastic fluid and an elastic stress located behind the organism that aided the return (backward) stroke and hindered the power (forward) stroke. Zhu *et al* [27] also observed this elastic stress located behind the puller, reducing its speed. Qin *et al* followed their experimental results with simulations [53] of flagellar action. The change in gait in a viscoelastic fluid reduced the speed as compared to the Newtonian stroke, but increased the efficiency of swimming. The reduction in speeds is consistent with the results observed.

All these results are interpreted with the caveat that the shear rate applied by the cells on the viscoelastic fluids is unknown. The viscosity plotted is for an 'equivalent shear rate' as rationalized by Qin *et al* [52] based on the sources of shear rates applied on the cells and bodies. Regardless of the shear rate, the velocities of cells in the viscous viscoelastic fluids are lower than or comparable

to the velocities in Newtonian fluids of viscosities higher than the viscoelastic fluids. This clearly attests to an effect of viscoelasticity on the swimming of the cells.

The ratio of the cell velocities in viscoelastic to that in Newtonian fluids plotted in Figure 4.7b reveal a big drop in the ratio for 250 ppm PASA, after which it plateaus at around 0.42. Qin *et al* observed that this drop corresponded to a Deborah number of 2, the value at which the beating frequencies of the viscoelastic and Newtonian fluids started to diverge. This saturation is consistent not only for the results obtained for *C.Reinhardtii* [52], but also for experiments on *C.Elegans* [49] and simulations [37, 38]. Though the shear rates are unknown, the existence of this plateau might indicate an upper limit on the applied stress on the organism. The simulations conducted by Zhu *et al* [27] revealed that for fluids with short relaxation times, the elastic stresses acted immediately. For fluids of higher elasticity, and therefore, longer relaxation times, the elastic stresses were stronger but the polymers took a longer time to become fully stretched. The swimming motion of a puller caused this elastic stress to stretch behind it, thus only a portion of the elastic stress was found to act on the puller. In the case of highly viscoelastic fluids, the pullers swam away before the polymer got fully stretched. This could possibly explain the plateau in our results.

To verify if the cells swim in a helical motion as observed by Crenshaw *et al* [54] and Muller [19], the relationship between velocity, pitch and radius are plotted as 2D histograms for the TRIS case first. The increase in pitch with increasing velocity is observed in our results up to a pitch of $\sim$ 80 μm, which is similar to those obtained by Muller [19]. There doesn't appear to be a similar relationship between radius and velocity though, with the radii appearing to concentrate in one region as confirmed by the radius vs pitch histogram. The mean radius and pitch, however, is similar to the values obtained by Muller [19]. A glaring difference between the two plots is in the chirality, with our results exhibiting positive chirality in contrast to Muller's negative chirality. Crenshaw *et al* [54] reported that the cells switch chirality during a phototactic response. The chance for phototaxis is, however, greater under the green light used by Muller [19] than under red light used in our experiments [15]. This might be because of other factors that influence chirality, be it during culturing or experimentation. The overall behaviour exhibited by the cells in TRIS still remains similar to previous results though [19], and more experiments might reveal the cause of this chirality shift.

The radius and pitch reduce with increasing viscosity, with the values dropping further for the viscoelastic solutions. The drop in radius and pitch for the viscoelastic solutions could be explained by the results from the numerical simulations of the flagella of *C.Reinhardtii* by Li *et al* [53]. The trajectories executed by *C.Reinhardtii* were plotted by them for both viscoelastic and Newtonian strokes. While the shapes executed by the two strokes remained the same, the distance covered by the trajectories were a lot smaller for the viscoelastic stroke. This is primarily because of the bending of the distal tip in the viscoelastic fluid. To observe if the overall shape remains the same, the aspect ratio (radius to pitch) is determined for all the 5 cases. The aspect ratios were found to be around 0.09, indicating that the cells retain their tendency to form elongated helices in all fluids though the actual radius and pitch drops. The aspect ratio is also consistent with the results in TRIS obtained by Muller [19]. The drop in radius and retention of shape seem to corroborate the results obtained by Li *et al* [53] in viscoelastic fluids. While these results explain the drop in radius and pitch for viscoelastic fluids, it does not necessarily explain the drop in more viscous Newtonian fluids. This drop might be related to the drop in velocity, increasing the viscous drag on the cell.

The rotation rates were also observed to drop with an increase in viscosity. The rotation rates in viscoelastic solutions were lower than the corresponding Newtonian cases, but if the comparison

is based on solutions of similar velocity, the rotation rates in viscoelastic solutions are larger than the corresponding Newtonian cases. This is in contrast to the trends exhibited by the other parameters, which were comparable. This implies that there is a tendency to reorient frequently in a viscoelastic fluid, and this might be useful in interpreting these results from a hydrodynamic point of view.

The trajectories followed by the cells in all the viscous and viscoelastic cases are similar to the results obtained for the TRIS case and by Muller [19], which provides more evidence for the retention of the cell trajectory implied by the similar aspect ratios. The only trajectory which appeared to differ from the TRIS case was the circling in the bulk, something which was only observed near the walls for the TRIS case. The cause for this is unclear, though it must be noted that these trajectories are quite rare in all the cases.

5.2. Cell-Wall interactions

Figures 4.12 and 4.14 showed that the cells tend to accumulate near the walls of the chamber regardless of the fluid. These results have also been reported by Muller [19] for *C.Reinhardtii*, Lee *et al* [18] for the organism *P.Minimum* and for *E.Coli* by Berke *et al* [24]. The concentration profiles from Figure 4.12 show a greater accumulation at the top wall than the bottom, and this is probably due to the tendency of the cells to display negative gravitaxis [15]. The time averaged cell densities in Figure 4.14 confirm this, although the effect of negative gravitaxis doesn't appear to be as pronounced. The only exception among these tracks is the Ficoll 12.5 % case, and the possible reason is due to the noise in the images, which result in jumps in the tracks. The data obtained from the kinematics is still valid, as the jumps are filtered out while calculating the radius, segmenting a single track into two. The same cannot be done when the cell-wall interactions are analysed, as it is difficult to judge the events that have transpired before and after the jump. Because of this, this case is not discussed in detail when it comes to cell-wall interactions.

The trajectories near the wall are similar to the results obtained by Muller [19] for all the cases, with the cells executing symmetric reflections, asymmetric reflections, circling, bouncing and wobbling near the contact region. The circling near the wall has also been observed for bacteria by Lauga *et al* [22], who reasoned that the circling was due to the viscous drag acting on both the head and tail. Since we do not have any view of the flagella when these interactions take place, it is difficult to ascertain the possible reasons for this movement. Reflections near the wall have been reported by Kanstler *et al* [30] and Contino *et al* [31]. Though the cells still retain the overarching trajectories near the wall, the frequency of events and general wall behaviour is different for each case.

To see if the cells have a tendency to enter the contact region, the minimum distance of all the wall bound tracks are plotted in Figure 4.19. The cells seem to show an inclination towards entering the contact region in all the cases, but the cells seem to move closer to the wall as the solutions become more viscous, crashing into it for the 250 ppm PASA and 12.5 % Ficoll cases. Berke *et al* [24] theorized that a puller would crash into the walls by using a dipole approximation, but this prediction is only for the TRIS case. The observed phenomenon merits more experiments to see if this is this behaviour is related to deficiencies in the tracking code due to possible noise or if it is actually exhibited by the cells.

To understand the events that occur near the wall, the residence times, incoming and outgoing angles were determined for complete tracks. The residence times for the TRIS case near the

contact region were found to be around 0.5 seconds, whereas the residence times were around 2 seconds for Muller [19]. It should be noted that the definition for residence time in Muller's case is slightly different from ours. Muller defined the residence time as the time spent within l_c instead of 30 μm from the wall, and he didn't normalise using the bulk velocity as well. The discrepancy is probably due to the commonality of symmetric reflections in Muller's case, whereas asymmetric reflection is dominant in ours. The obtained results are closer to those obtained by Kanstler *et al* [30], where the cells displayed a loss of memory in incidence angle, rather than those of Muller [19]. The paper by Kantsler *et al* [30] showed that cells tend to accumulate at a distance of 25 μm from the wall and our results appear to confirm this. The cells tend to enter at a steep angle and leave at a narrow angle, and Kanstler proposed that there was a trapping mechanism near the wall as a result of direct ciliary interactions. The possible reasons for the discrepancy from Muller's results are perhaps related to the usage of a different light source that minimizes phototaxis and improved efficiency of the tracking code.

The tracks that do not come near the contact region but still enter within 100 μm of the wall are also observed as they could be of interest from a hydrodynamic point of view. Here, the trajectories are a lot more diverse, with asymmetric reflections being more common in TRIS. The incidence angles are not always steep, and the outgoing angles do not seem to map onto any relationship with the incidence angles. A clear correlation between incoming and outgoing angles was not observed by Muller [19] either, but it should be noted that there were lesser tracks than in the contact case.

Its difficult to identify any sort of consistent behaviour from the obtained residence times and angles for the more viscous cases as there are less completed tracks. One explanation for lesser completed tracks would be the slower speeds of the cells, as a cell in TRIS would cover larger distances in a span of 10 seconds as compared to cells in other solutions. But the idea of choosing a lower frame rate, in addition to minimizing noise, was to circumvent the limitations of the tracking code by allowing it to track for the same amount of frames but for longer times. Unfortunately, though there were some long tracks, it wasn't enough to discern any trend near the wall. Perhaps more experiments in these fluids need to be conducted to investigate the interactions and the tracking efficiency at lower frame rates.

The residence times for the limited number of tracks near the contact region are longer than those obtained for the TRIS case, but the times are more evenly distributed as well. The mean residence times for all the cases are around 1-1.5 seconds. A numerical study by Li *et al* [39] showed that the residence times are slightly longer for the viscoelastic cases for a puller located near the wall. The residence time was found to be the longest for a Weissenberg number of 0.2, after which the residence times were observed to stagnate at a value slightly longer than the Newtonian case. They theorized that this was because of the nearly even polymeric stretching around the puller, in contrast to an asymmetric elastic wake generated for pushers and neutral squirmers. Though this is consistent with what we observe, one should bear in mind the lesser number of tracks. The simulations by Li *et al* [39] fixed the starting positions of the cells, ignoring the possible effects of the far field hydrodynamics. Also, flagellar contact with the walls and the change in gait shown by the experiments of Qin *et al* [52] were not taken into account here. For the tracks that do not come near the contact region, the data available from all the cases was even lesser, making it all the more difficult to discern any possible correlations.

Since there are few tracks to draw any conclusions, the general trajectories of the cells that come near the contact region were plotted in Figure 4.26 for all the fluids. The trajectory of the

cells in TRIS showed a bimodal distribution indicating both symmetric and asymmetric reflections near the contact regions, with the mean trajectory indicating that the cells tend to gravitate towards asymmetric reflections near the wall. This result appears to validate the work by Kanstler *et al* [30], also confirming our previous results for TRIS. The outgoing angles are almost always shallow, and a steep entrance angle is more common. This behaviour appears to be retained in the 150 ppm PASA, although the entrance angles are shallower and the trajectory also points to some wobbling near the wall. The primary reason for this greater wobbling might be due to the slower speeds near the wall. Once the viscosity increases, the tracks appear to get more symmetric. This might be related to an increase in viscous drag, which results in a reduced rotation rate that might align the cell parallel to the surface. The entrance angles are shallower for the 7 % Ficoll case, but the overall behaviour still points to asymmetric reflection. In the 250 ppm PASA solution, however, the trajectories are symmetric, with the outgoing angles being a lot steeper than the other cases.

To understand the reasons for this change in behaviour, we need to find a way to determine if the interactions near the contact region involve flagellar contact, hydrodynamics or both. One way of explaining this might be to check if there is a drop in velocity near the contact region, and this was checked in Figure 4.27. Contino *et al* [31] found that both hydrodynamic and contact interactions occur near the wall for *C.Reinhardtii*, differing from Kanstler's results [30]. The contour plot between distance and non-dimensionalised velocity in TRIS shows a drastic drop in cell velocity once it enters the contact region. From Contino *et al's* [31] results, a drop in velocity higher than what was theoretically predicted was recorded, leading them to conclude the effect of both contact and hydrodynamic results. But this was observed only for shallow incoming angles, unlike the steep angles obtained in our case. Further, the loss of memory in incidence angle was less frequently observed in their case. Our obtained values of incoming and outgoing angles seem to corroborate with Kanstler's results [30] near the contact region, but their experiments were conducted in a more constricted space, unlike the 2 mm depth in ours. It should be noted that the drop in velocity does not necessarily point to flagellar contact, with simulations by Li and Ardekani [26] and Li *et al* [39] showing reductions in velocities near the walls because of hydrodynamic forces related to the viscous drag. Since there is no view of flagellar action in our case, it is difficult to pinpoint the exact reason for the drop in velocity, though the similarity of our results with that of Kanstler *et al's* [30] experiments might point out to the dominance of flagellar contact.

The trend becomes less clear once we move towards the more viscous solutions. In case of the 150 ppm PASA and 7 % Ficoll solutions, there are cells that are observed to swim at the mean speed even in contact region, though this drops once we enter a distance of about 10 μm. This might indicate that there are some hydrodynamic interactions observed in this region, though there is some uncertainty because we can't view the flagellar action. In the 250 ppm PASA and 12.5 % Ficoll solutions, however, there's no significant drop in velocity, with the lower velocities being observed in the bulk as well. Also, it was observed that there are a large number of tracks that seem to hit the wall in both of these solutions, something that was not observed in the others. The presence of a large number of tracks at the wall might indicate that the dominant interaction is flagellar contact, but the velocities indicate that there might be some hydrodynamics involved here as well. The results obtained from these histograms could also explain the shallower incoming angles for the more viscous cases, with the angles being related to the nature of the interaction.

Berke *et al* [24] modelled the bacteria in TRIS as a force dipole, with the two forces corresponding to the propulsive force and viscous drag. He observed that for bacteria, the cells induce a flow field near the wall that align it parallel to the surface. Extending this analogy for a puller, which can also be represented as a dipole but of opposite sign, Berke theorized that the wall induced

forces tend to align the puller perpendicular to the wall, causing it to crash into the walls. To see if this is indeed the case for TRIS, the orientation with respect to the wall is plotted against the normalised height in Figure 4.28 though *C.Reinhardtii* is asymmetric [15] and flows unsteadily [16]. The results show that the trends observed near the wall extend towards the bulk as well in TRIS, with the cells tending to align at steep angles closer to 90° when it pitches towards the wall. The cells also leave at shallow angles which are observed to transition to steep angles, corroborating Berke's hypothesis and indicating an influence of hydrodynamics induced by the boundaries.

The cells continue to enter at steep angles even in 150 ppm PASA, though the values appear higher than those obtained from Figure 4.25b. There also appears to be a large number of cells aligned parallel to the wall throughout the bulk. This is even more apparent in the 250 ppm PASA solution, with a large number of cells concentrated at shallow angles. The tendency to enter the wall at steep angles hasn't dissipated entirely, although its considerably lesser. Yazdi *et al* [40] investigated the locomotion of microorganisms near a no-slip boundary in viscoelastic fluids, and found the existence of an attraction layer close to the wall for pullers. Except for orientations perpendicular to the wall, the simulations observed that pullers tend to align themselves parallel to the wall without going towards it. Only cells near the attraction layer moved towards the walls. Though these results could explain the bulk of the cells that are parallel to the surfaces in viscoelastic fluids and perhaps the lack of evidence for contact interactions, it doesn't explain the large number of cells concentrated near the walls. Not all these cells enter at steep angles, so it might imply that an 'attraction' layer, if any, might probably exist at regions further away from the wall than predicted by Yazdi *et al* [40]. These simulations also didn't take into account the bending of the flagella in viscoelastic fluids. Additionally, the dipole approximation loses its validity in a viscoelastic case because of the presence of a non uniform elastic component that might aid or deter the swimming [27, 52, 53], so differences are naturally expected from the TRIS case. The accumulation of cells at shallow angles might be due to this interaction of elastic forces that frequently alter the orientation of the cells. The higher rotation rates for solutions of comparable velocity might be as a result of these elastic forces as well.

While this line of argument might explain the tendency to align parallel to the surface for viscoelastic fluids, it doesn't explain the near symmetric distribution in the Ficoll 7 % solution, where the angles are shallower than in its viscoelastic counterparts. The bulk of the cells have aligned themselves nearly parallel to the surface, though there are quite a few cells that seem to enter the wall at around 40-50°. There also some cells that leave the wall at angles around 30°, displaying a closer retention of incoming angles than the TRIS case. This is a strange observation for a Newtonian fluid, as one would expect the maintenance of angles in the viscoelastic fluids because of the elastic memory effect. These results certainly merit more experiments and further investigation. The reduction in the magnitude of the orientation might be tied to the decrease in beating frequency with viscosity [52], an effect not observed in viscoelastic fluids. The cells display certain similarities in terms of wall interactions in the Newtonian and viscoelastic fluids despite the presence of different phenomenon.

Berke *et al* [24], expanding on his previous results, also showed that the average wall induced attraction for a large number of dipoles will be zero, with those oriented towards the wall showing a positive attraction and those oriented away from it showing a repulsion. To see if this is the case for TRIS, a contour of the orientation against the normalised height was plotted in Figure 4.29, with the colour bar indicating the mean angular velocity for each bin. For a perfect dipole, the net angular velocity should be zero. The mean angular velocity isn't necessarily the best measure, as the standard deviations in each bin are high. Still, it could reveal the general disposition of cells and

nature of the hydrodynamic forces. Though the contour isn't very clear, the tendency of the cells to move towards the wall for a positive orientation is seen, with larger angular velocities observed at steep angles at z^*=20. On the left-hand side, there is some indication of the cells moving away from the wall at first, but the left-hand side of the plot appears to show an overall neutrality in angular velocity. The behaviour observed in Figure 4.28a is not reflected in the contour, with no clear leaving at shallow angles. Though vague, these results might point to an increased attraction towards the wall, considering that the overall angular velocity appears to be slightly positive. That said, more data sets are required for conclusive evidence because, as stated before, the cells are not entirely symmetric and flow unsteadily. Also, it is possible that the contour is dominated by noise. More data sets and experiments might shed some more light on the hydrodynamics which this contour just touched.

The dipole approximation might not be valid in the viscoelastic cases as there is an additional uneven elastic force to contend with. Still, the contours are plotted as they might reveal something about the hydrodynamics in viscoelastic fluids, especially if the elastic memory effect leads to a greater wall attraction. Both the results from the 150 ppm and 250 ppm PASA solutions are inconclusive and do not point to any specific behaviour, though the attraction towards the wall appears to be reduced for the 250 ppm case. The average wall induced attraction for the entire set appears to be neutral, matching the results for a perfect dipole. These results also seem to be in good agreement with the results of Yazdi *et al* [40], who, despite their assumptions, showed that the angular velocities of the puller constantly changes sign in an Oldroyd fluid (model viscoelastic fluid) with a Deborah number of 10, giving it an overall neutrality. Though the Deborah number of the 250 ppm PASA solution isn't that high, it shows traces of this behaviour. The cells in the 150 ppm PASA solution, on the other hand, show a tendency to move towards the wall like the TRIS case. More data sets could reveal if the behaviour in viscoelastic fluids is consistent with the results of Yazdi *et al* [40], implying that the simplified assumptions might hold its ground from a hydrodynamic point of view, though the dominance of noise cannot be ruled out as the behaviour in TRIS hasn't been captured.

As for the viscous cases, the results continue to confound. The angular velocities in the 7 % Ficoll solutions are largely positive, even more than the TRIS case. This could be tied to the increased viscous drag that increases the hydrodynamic attraction. The dearth of experiments in more viscous fluids and the results obtained in our experiments makes the effect of viscosity as important as viscoelasticity for further investigation.

6

Conclusions and recommendations

6.1. Conclusions

Using the existing methodology used by Muller [19] and described in Chapter 3, experiments were conducted and the cells were tracked in viscoelastic and Newtonian fluids of varying degrees of viscosity. The velocities of the cells were found to be lower in viscoelastic as compared to Newtonian fluids, corroborating the results of Qin *et al* [52] for *C.Reinhardtii*, with the observed trend similar to those obtained for *C.Elegans* [49] and simulations [27, 38]. Though the exact shear rates applied by the cells on the viscoelastic fluid is unknown, the replication of behaviour from existing literature point to a clear effect of viscoelasticity. To study the trajectories and cell-wall interactions, four solutions were chosen- 150 ppm PASA, 7 % Ficoll, 250 ppm PASA and 12.5 % Ficoll solutions. Since it is difficult to compare based on the viscosity as the applied shear rates are unknown, solutions were compared based on similar cell velocities as well.

The cells were still observed to swim in helices as observed by Crenshaw *et al* [54] regardless of the fluid medium. The radius and pitch of the helices reduced with increasing viscosity. This effect was more pronounced in the viscoelastic cases, with solutions of lower viscosity still showing comparable radii and pitch as Newtonian solutions of higher viscosity. The aspect ratio, however, was similar in all the fluids, implying that the cells retain their overall shape. These results are consistent with the observations by Qin *et al* [52] and the subsequent simulations of Li *et al* [53] on *C.Reinhardtii*, where the bending of the distal tip in viscoelastic fluids was observed, which led to the reduction in distance travelled despite retention of the overall shape. The rotation rates were observed to be higher in viscoelastic solutions when compared in terms of velocity, with the overall rotation rates dropping with increase in viscosity.

The results in TRIS show a similar behaviour as compared to those obtained by Muller [19], with the glaring difference being in the dominance of right-handed chirality in our case. Though the results from Crenshaw *et al* [54] indicate that this might be due to phototaxis, there is a greater chance of phototaxis with the green light used by Muller rather than the red light used in our case [15]. More experiments need to be done to observe if this chirality change is related to experimental conditions and culturing.

The results for the cell wall interactions are more complicated to draw conclusions. The cell concentration profiles were observed to be similar for all fluids except for the 12.5 % Ficoll solution, where the data presented might be affected by the noisiness of the image. The cells were observed to concentrate at the boundaries, especially near the top wall, possibly because of the cells'

tendency to exhibit negative gravitaxis [15]. These results have been reported by Muller [19] in TRIS, with this distribution also being observed for the organisms, *P.Minimum* [18] and *E.Coli* [24]. The trajectories observed in all the fluids near the wall are similar to those observed by Muller [19] in TRIS, though the frequency of events is different.

The wall interactions are segregated into two categories- those that involve the cells entering the contact region, and those where the cells are within 100 μm from the wall but do not enter the contact region. The residence times near the contact region in TRIS appeared to concentrate at around 0.5 seconds, different from the results of Muller [19]. The obtained values of the outgoing angles also show a loss of memory of the incidence angles, implying the dominance of asymmetric reflection. These results are closer to those predicted by Kanstler *et al* [30] than Muller [19]. For the more viscous cases, there were fewer completed tracks to draw any conclusions.

So to discern any possible differences, the overall trajectories of the tracks near the wall were considered. The trajectories in TRIS appeared to confirm the previously obtained results for incoming and outgoing angles, with asymmetric reflection being the dominant phenomenon near the contact region. This was also observed for the 150 ppm PASA and 7 % Ficoll solutions, but the incoming angles were less steep than the TRIS case, while the outgoing angles remained comparable. For the 250 ppm PASA case, however, the trajectories were a lot more symmetric. To understand the phenomenon, the velocities near the contact region were checked. The normalised velocities of the cells in the TRIS case showed a drastic drop in velocity, probably indicating the dominance of contact interactions near the contact region as predicted by Kanstler *et al* [30]. The results from the 150 ppm PASA and 7 % Ficoll cases also showed a drop in velocity, though cells were swimming at velocities close to the mean near the contact region. This trend appears to have changed for the 250 ppm PASA solution, with no discernible drop observed in the contact region. The only observable change is the absence of higher velocities in the contact region.

To focus on the hydrodynamics, the orientation of the cell with respect to the walls was plotted against the normalised height. The cells in the TRIS solution appeared to retain their behaviour in the contact region even in the bulk, with a large number of cells moving at steep angles until they encounter a wall, after which it leaves at a shallow angle. These results in TRIS are consistent with those predicted by Berke *et al* [24] for a puller modelled as a dipole, which might not be valid for a viscoelastic case. The results for the viscoelastic solutions revealed a greater tendency to align parallel to the surface, with this being more pronounced at higher viscoelasticity. The tendency to enter the wall at steep angles is still retained, although this behaviour is vestigial. This behaviour is similar to those predicted by Yazdi *et al* [40], though there are stark differences with respect to the other predictions observed. The behaviour for the Newtonian Ficoll 7 % solution is strange, with many cells tending to concentrate at shallow angles. The entrance angle is still larger than the outgoing angles, though this is not apparent in this case. These results imply that the viscous fluids might be more complicated than previously imagined, with the dipole approximation not being valid for these cases. More data is required for the viscoelastic as well as the viscous cases to provide concrete conclusions about changes in behaviour.

The hydrodynamics are further studied by focussing on the angular velocities to see if there's a tendency to go towards the wall or if the overall wall induced attraction is zero as predicted by Berke *et al* [24] for a dipole. Though the results from the TRIS case indicate a positive wall interaction, the behaviour of entering walls at a steep angle and leaving at shallow angles is not captured. In the viscoelastic solutions, the wall attraction appears to reduce with increasing viscoelasticity, with the overall angular velocity being neutral in the 250 ppm PASA case. This

behaviour is consistent with the simulations of Yazdi *et al* [40] for fluids of high Deborah number. In the Newtonian Ficoll 7 % solution, the angular velocities are observed to be even more positive than the TRIS case. All this implies that a lot more data is required to draw suitable conclusions about the hydrodynamics and wall-induced attraction, so more experiments need to be conducted.

6.2. Recommendations

Our results not only show a clear influence of viscoelasticity on cell behaviour and motility but also the effect of higher viscosity on these parameters. As with most experimental results, more experiments need to be conducted to understand the underlying phenomenon further and draw conclusions, and this is especially true in the case of wall interactions. From the results of this thesis, the following is recommended for future experimentation and understanding:

- More experiments on both the viscoelastic and Newtonian cases have to be conducted. The tracking efficiency of the code at lower frame rates also needs to be characterised and if necessary, improved.
- Concatenate data from all the experiments to understand the hydrodynamics and cell-wall interactions clearly.
- Expand on the results of Yazdi *et al* [86] and Ardekani *et al* [41] for pullers by checking for the emergence of limit cycles, characterising the possible differences for the viscoelastic and viscous cases.
- The experiments can be conducted in different viscoelastic and Newtonian solutions to see if the cell behaviour changes based on the material.
- Tomographic Particle Image Velocimetry (Tomo-PIV) could reveal useful information about the physics of the flow. An alternative to this would be to conduct simulations of the flagellum based on the results observed in our thesis and by Qin *et al* [52].

A

Rheometer accuracy

The accuracy of the LS-40 rheometer was tested using distilled water. The experiment was conducted over three days, with the calibration changing over each reading. The viscosities were determined for each shear rate and plotted in Figure A.1a. The accuracy of the rheometer was found to vary with the shear rate and the calculation. The error of each reading based on the true value of viscosity at 20° is plotted in Figure A.1b, along with the mean error for these five readings. The maximum mean error was around 6 %, with the maximum local error being 12 %. These readings showed that the accuracy of the rheometer was satisfactory for solutions of unknown viscosity. Also, the calibration was found to affect the accuracy of the rheometer, though the discrepancy isn't large.

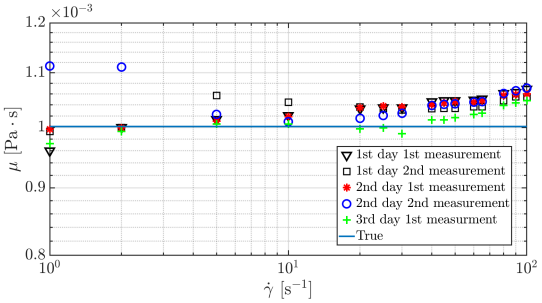

(a) Rheometry results for viscosity of distilled water over different measurements at 20° C, as compared to the true value.

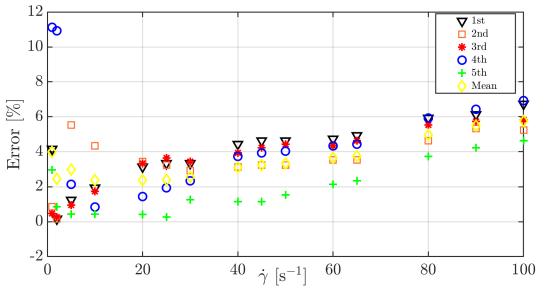

(b) Error of the measurements for each shear rate. The mean error is shown as yellow diamonds,whose maximum value is 6 %.

Figure A.1: Accuracy of the rheometer

B

Relaxation time measurements with AR-G2 rheometer

Initially, Small Amplitude Oscillatory Shear (SAOS) measurements were carried out in the AR-G2 rheometer to determine the relaxation time. First, a strain sweep was done at an angular frequency of 10 rad/s to determine the linear viscoelastic regime. This test was carried out up to a strain of 10 for the 100 ppm PASA solution. As seen from Figure B.1, the elastic and viscous moduli remain roughly constant until a strain of 10 except for the lower strains, which is mostly noise associated with the compliance of the machine. Since this data is unknown when performing the optical trap experiment, results from this test confirm that the obtained relaxation times for the optical trap test correspond to the linear viscoelastic region.

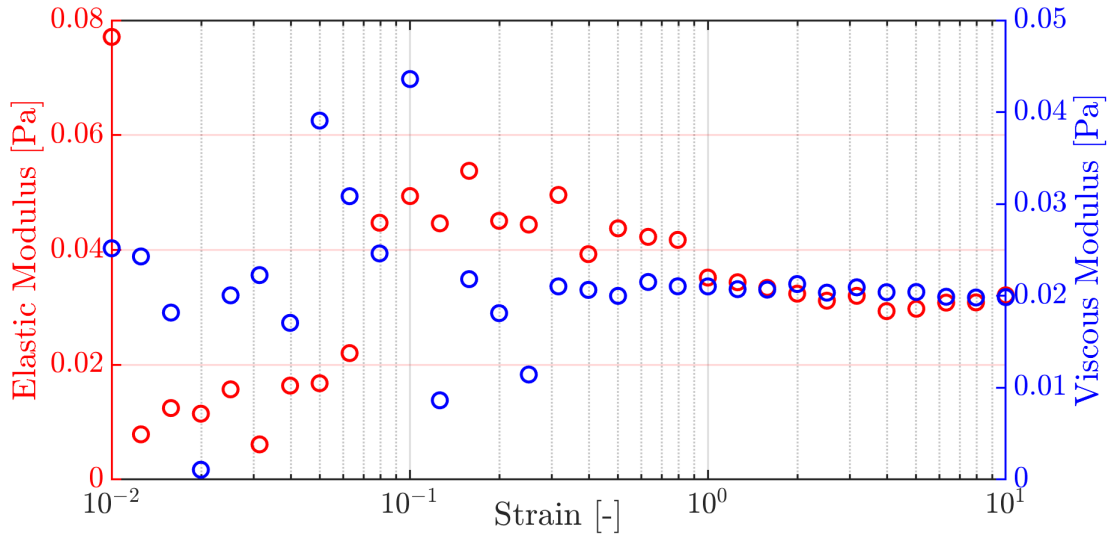

Figure B.1: Strain sweep test at an angular frequency of 10 rad/s for 100 ppm PASA. The solution appears to be in the linear viscoelastic region until a strain of 10.

Unfortunately, the rheometer could not measure low relaxation times, as shown in the results of 1000 ppm PASA solution, because of compliance errors inherent to the machine. To verify if our solutions were viscoelastic, SAOS measurements were performed for the 4000 ppm PASA solution. This showed a clear intersection between the viscous and elastic modulus (Figure B.2a), in contrast to the 1000 ppm PASA case (Figure B.2b), giving a relaxation time of 2.51 seconds. This validated the viscoelasticity of our solutions, allowing to proceed with the experiments.

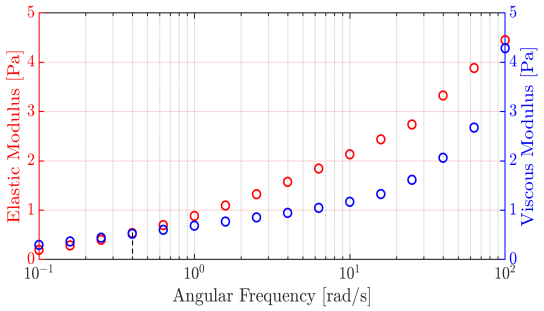

(a) SAOS measurements for the 4000 ppm PASA solution. The black dashed line indicates the intersection.

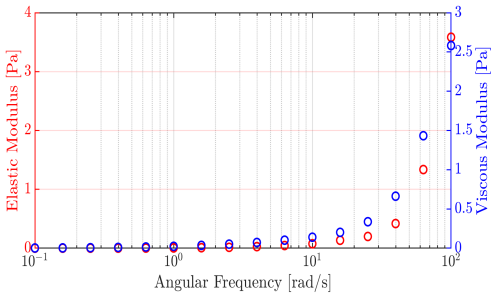

(b) SAOS measurements for the 1000 ppm PASA solution.There is no clear intersection observed here.

Figure B.2: SAOS measurements using AR-G2 rheometer

C

Kinematics in highly viscous solutions

The velocity, radius and pitch are plotted in Figure C.1 for the cells in the 1000 ppm PASA and 20 % Ficoll solutions. A fit length of 9 was used as the analysis to select the correct fitting parameters as elucidated in section 3.6.5 was not performed. Even so, these results reveal that the radii and pitch of the cells in these solutions are too low, with the values ranging from 0-0.3 μm. Though it appears that the radii in the 20 % Ficoll solution are larger, it is difficult to draw any conclusion about the effect of viscoelasticity and the nature of the trajectories at these small radii. The effects observed from these plots might be due to the high viscosities rather than anything else. A relationship between the velocity and pitch would be even more difficult to establish at these small values. In order to provide clarity and aid understanding of the phenomenon involved, the solutions of lower viscosity are chosen to discern the differences in cell behaviours and characterise the influence of viscoelasticity and viscosity clearly. In addition to the kinematics, the cell wall interactions are all the more difficult to characterise at these velocities primarily because the local velocities of the cells can reach very low values. This makes it difficult to characterise the nature of the interaction and also, the problems stated in Chapter 5 with respect to tracking are more pronounced in these cases.

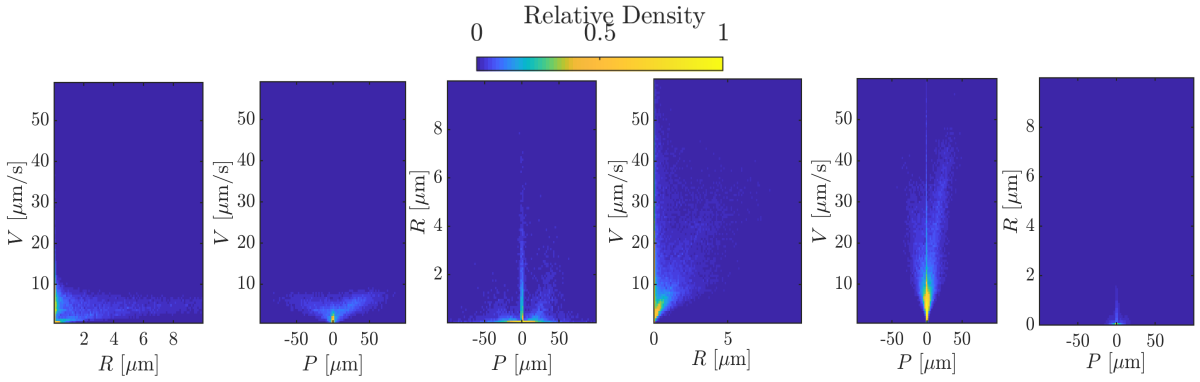

(a) 1000 ppm PASA **(b)** 20 % Ficoll solution

Figure C.1: Kinematics for solutions of high viscosity

D

Filter length for other solutions

The fitting parameters for the other solutions are calculated in the same manner as explained in Section 3.6.5. The results are plotted in Figures D.1, D.2 and D.3, and the filter length for all the solutions was chosen to be 11.

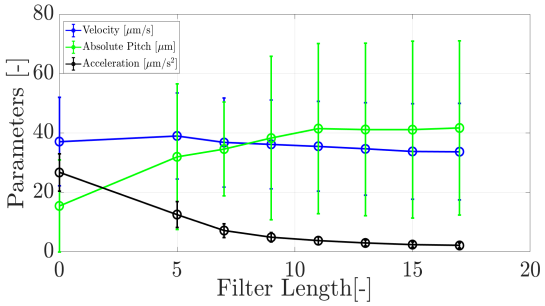

(a) Variation of parameters with filter length for the 250 ppm PASA solution.The error bars represent the standard deviations of the parameters.

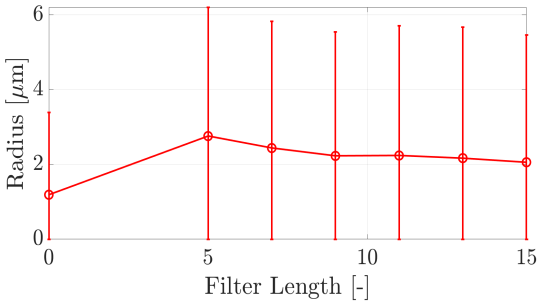

(b) Variation of radius with filter length for the 250 ppm PASA solution.The error bars represent the standard deviations of the parameters.

Figure D.1: Selection of filter length for 250 ppm PASA solution

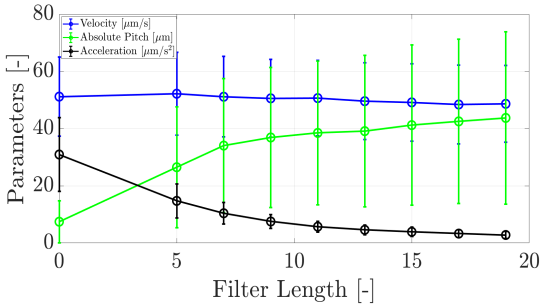

(a) Variation of parameters with filter length for the 7% Ficoll solution.The error bars represent the standard deviations of the parameters.

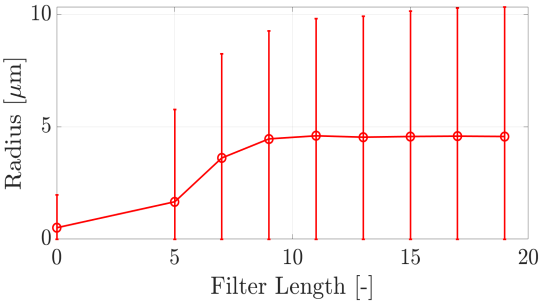

(b) Variation of radius with filter length for the 7% Ficoll solutionThe error bars represent the standard deviations of the parameters.

Figure D.2: Selection of filter length for 7 % Ficoll solution

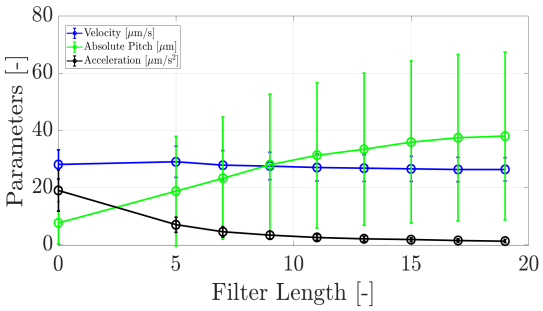

(a) Variation of parameters with filter length for the 12.5% Ficoll solution.The error bars represent the standard deviations of the parameters.

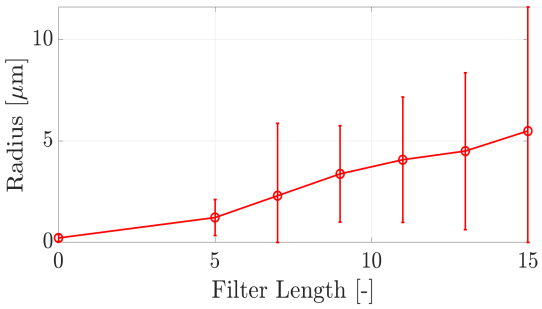

(b) Variation of radius with filter length for the 12.5% Ficoll solution.The error bars represent the standard deviations of the parameters.

Figure D.3: Selection of filter length for 12.5 % Ficoll solution

E

Mean free path

To check for the influence of cell-cell interactions on the cell behaviour, the mean free path for all the cases are plotted over the height of the domain in Figure E.1. The mean free path is defined as the average distance travelled by the cell between collisions with other cells. The formula to calculate the mean free path is similar to the formula used in kinetic theory for molecules.

$$MFP = (\frac{\pi}{4} d^2 \rho)^{-1} \tag{E.1}$$

where MFP is the mean free path, d is the diameter of the cell (10 μm) and ρ is the cell density. Since the mean free paths are at least 50 times more than the body length, we can conclude that the results presented aren't influenced by any interaction among cells.

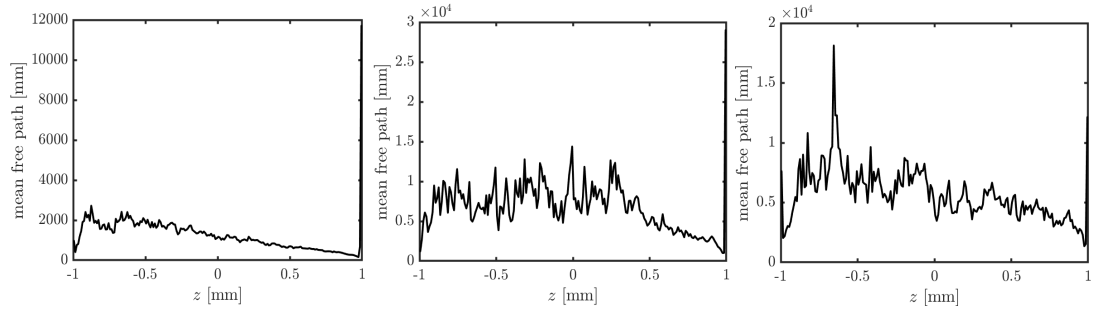

(a) TRIS **(b)** 150 ppm PASA Solution **(c)** 7 % Ficoll solution

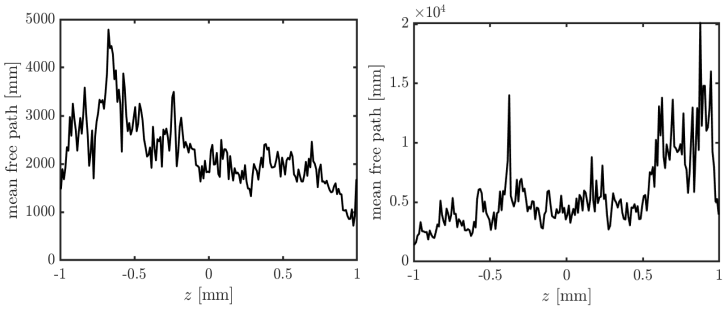

(d) 250 ppm PASA solution **(e)** 12.5 % Ficoll solution

Figure E.1: Mean free path of the cell as a function of the height over the domain

F

Velocity distribution

As mentioned in Chapter 4, a distribution of velocities is obtained for all the cases instead of a specific value. The velocity distribution in all the solutions along with the track lengths are plotted in Figure F.1.

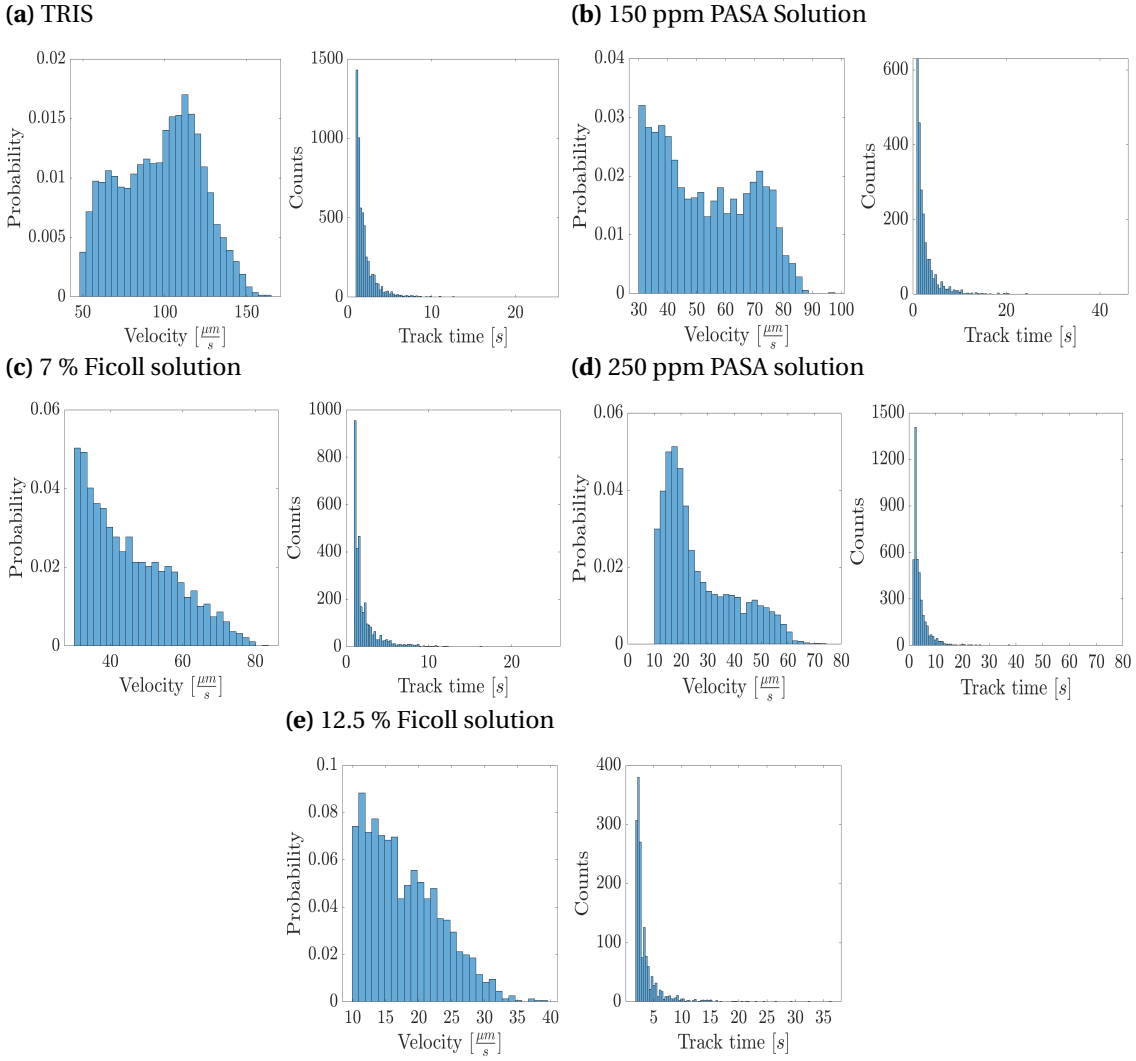

Figure F.1: Velocity and track length distribution

G

Additional trajectories

In addition to the trajectories presented in Chapter 4, wall bound wobbling is another commonly observed behaviour shown in Figure G.1.

(a) 150 ppm PASA

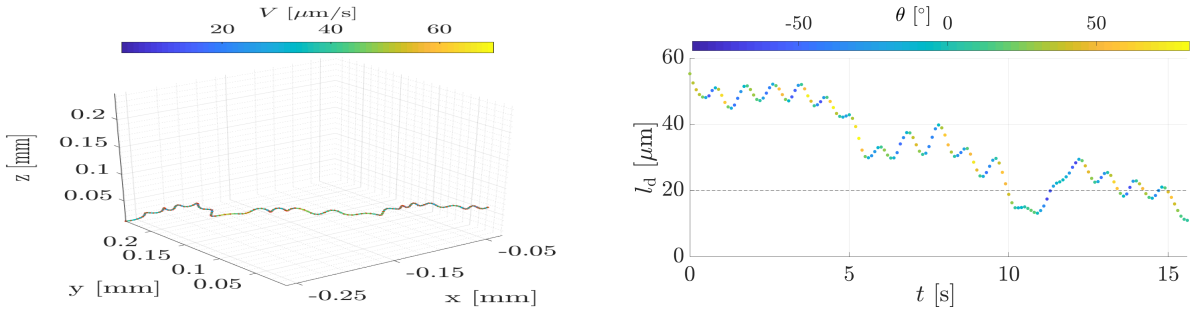

(b) 7 % Ficoll solution

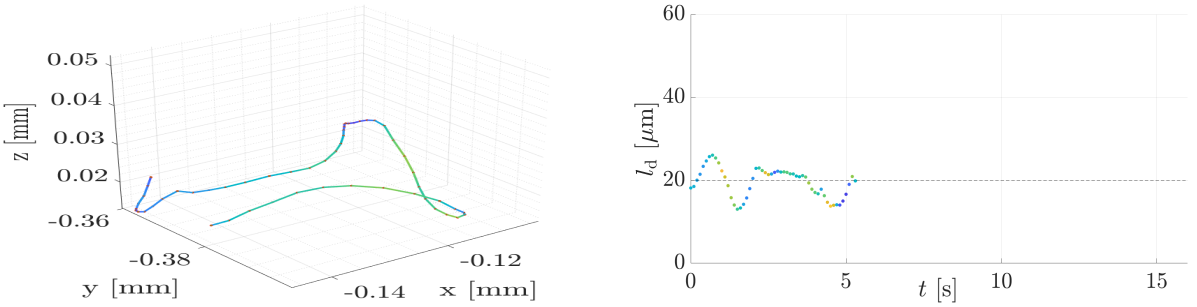

(c) 250 ppm PASA

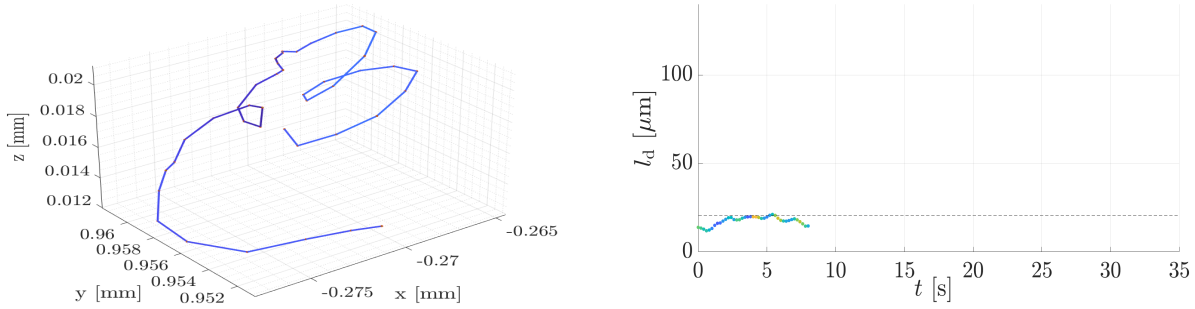

Figure G.1: Wall bound wobbling for the three cases. The dashed black line in the 2D plot indicates the contact region

The trajectories of the cells that come within l_c in TRIS are presented in Figure G.2. The overall trajectories are similar to those obtained by Muller [19].

(a) Symmetric Reflection

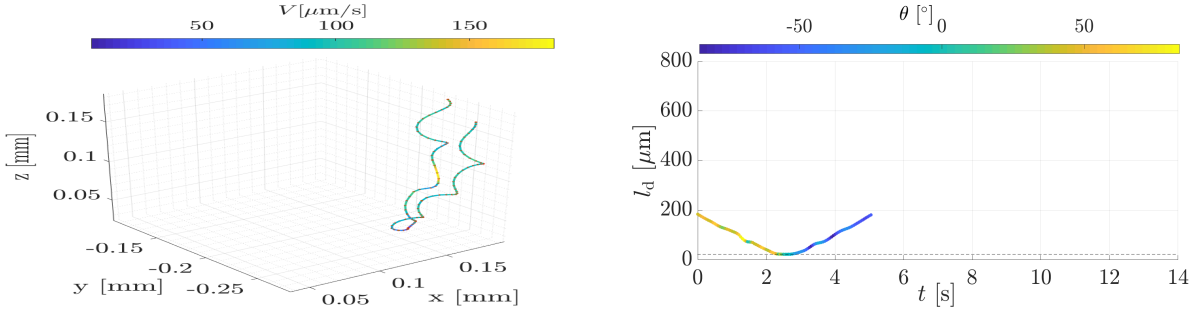

(b) Asymmetric Reflection

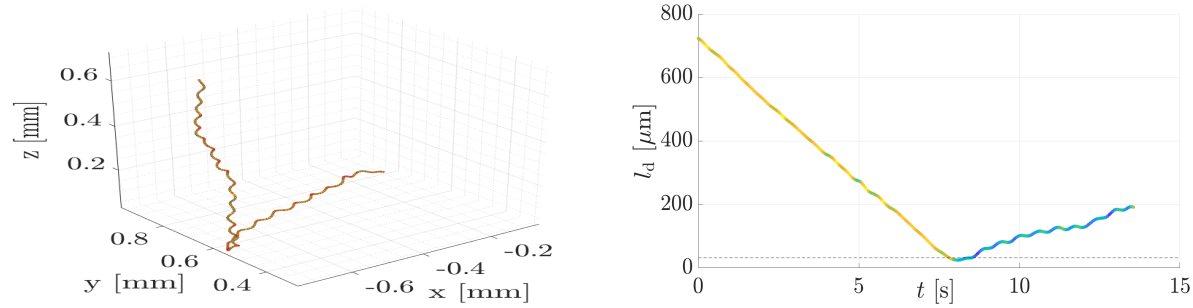

(c) Circling near the wall

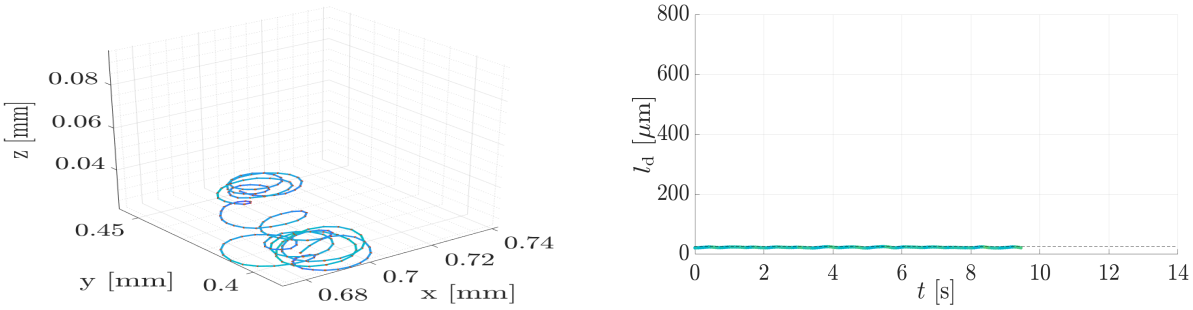

(d) Repeated wall bouncing

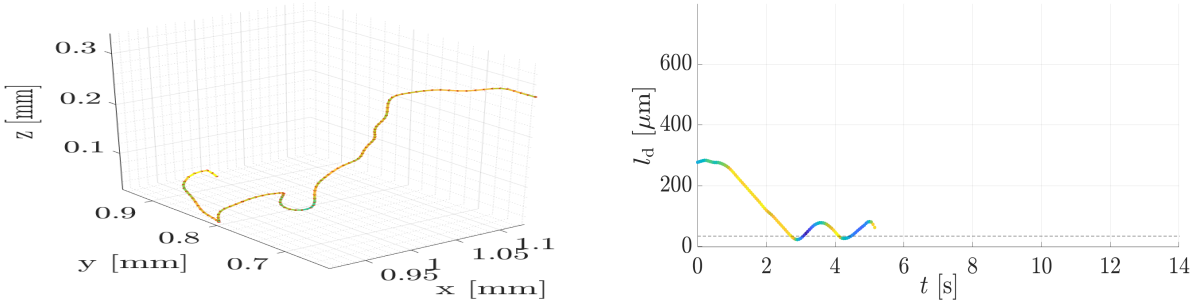

Figure G.2: Typical trajectories found near the wall for the TRIS case. The dashed black line in the 2D plot indicates the contact region

Bibliography

[1] Cesare Montecucco and Rino Rappuoli. Living dangerously: How helicobacter pylori survives in the human stomach. *Nature Reviews Molecular Cell Biology*, 2(6):457–466, 2001. ISSN 14710072. doi: 10.1038/35073084.

[2] Luanne Hall-Stoodley, J. William Costerton, and Paul Stoodley. Bacterial biofilms: From the natural environment to infectious diseases. *Nature Reviews Microbiology*, 2(2):95–108, 2004. ISSN 17401526. doi: 10.1038/nrmicro821.

[3] Chari Nithya, Felix Lewisoscar, Selvaraj Kanaga, Renganathan Kavitha, and Dhamodharan Bakkiyaraj. Biofilm inhibitory potential of Chlamydomonas sp . extract against Pseudomonas aeruginosa. *J. Algal Biomass Utln. 2014,*, 5(4):74–81, 2014.

[4] Leslie A. Pratt and Roberto Kolter. Genetic analysis of Escherichia coli biofilm formation: Roles of flagella, motility, chemotaxis and type I pili. *Molecular Microbiology*, 30(2):285–293, 1998. ISSN 0950382X. doi: 10.1046/j.1365-2958.1998.01061.x.

[5] Max Teplitski, Hancai Chen, Sathish Rajamani, Mengsheng Gao, Massimo Merighi, Richard T. Sayre, Jayne B. Robinson, Barry G. Rolfe, and Wolfgang D. Bauer. Chlamydomonas reinhardtii secretes compounds that mimic bacterial signals and interfere with quorum sensing regulation in bacteria. *Plant Physiology*, 134(1):137–146, 2004. ISSN 0032-0889. doi: 10.1104/pp.103.029918. URL `http://www.plantphysiol.org/content/134/1/137`.

[6] Wolfgang D. Bauer and Ulrike Mathesius. Plant responses to bacterial quorum sensing signals. *Current Opinion in Plant Biology*, 7(4):429–433, 2004. ISSN 13695266. doi: 10.1016/j.pbi.2004.05.008.

[7] S. S. Suarez and A. A. Pacey. Sperm transport in the female reproductive tract. *Human Reproduction Update*, 12(1):23–37, 2006. ISSN 13554786. doi: 10.1093/humupd/dmi047.

[8] Nidal Hilal, Victor Kochkodan, Laila Al-Khatib, and Tetyana Levadna. Surface modified polymeric membranes to reduce (bio)fouling: A microbiological study using E. coli. *Desalination*, 2004. ISSN 00119164. doi: 10.1016/j.desal.2004.06.138.

[9] Diego Meseguer Yebra, Søren Kiil, and Kim Dam-Johansen. Antifouling technology - Past, present and future steps towards efficient and environmentally friendly antifouling coatings. *Progress in Organic Coatings*, 50(2):75–104, 2004. ISSN 03009440. doi: 10.1016/j.porgcoat.2003.06.001.

[10] Tae Young Jeong, Gi Cheol Cha, Ik Keun Yoo, and Dong Jin Kim. Characteristics of bio-fouling in a submerged MBR. *Desalination*, 2007. ISSN 00119164. doi: 10.1016/j.desal.2006.07.006.

[11] E. M. Purcell. Life at low Reynolds number. *American Journal of Physics*, 45(1):3–11, 1977. ISSN 0002-9505. doi: 10.1119/1.10903. URL `http://aapt.scitation.org/doi/10.1119/1.10903`.

[12] E. Lauga. Life at high Deborah number. *Epl*, 86(6), 2009. ISSN 02955075. doi: 10.1209/0295-5075/86/64001.

[13] Elizabeth H Harris. Chapter 2 - Cell Architecture. *The Chlamydomonas Sourcebook*, pages 25–64, 2009. doi: 10.1016/B978-0-12-370873-1.00002-2. URL http://linkinghub.elsevier.com/retrieve/pii/B9780123708731000022.

[14] J. Elgeti, R. G. Winkler, and G. Gompper. Physics of microswimmers - Single particle motion and collective behavior: A review. *Reports on Progress in Physics*, 78(5):56601, 2015. ISSN 00344885. doi: 10.1088/0034-4885/78/5/056601. URL http://dx.doi.org/10.1088/0034-4885/78/5/056601.

[15] Elizabeth Harris H. Chapter 4 - motility and behavior. pages 89 – 117, 2009. doi: https://doi.org/10.1016/B978-0-12-370873-1.00004-6. URL http://www.sciencedirect.com/science/article/pii/B9780123708731000046.

[16] Jeffrey S. Guasto, Karl A. Johnson, and J. P. Gollub. Oscillatory flows induced by microorganisms swimming in two dimensions. *Physical Review Letters*, 105(16):18–21, 2010. ISSN 00319007. doi: 10.1103/PhysRevLett.105.168102.

[17] Knut Drescher, Raymond E. Goldstein, Nicolas Michel, Marco Polin, and Idan Tuval. Direct measurement of the flow field around swimming microorganisms. *Physical Review Letters*, 105 (16):1–4, 2010. ISSN 00319007. doi: 10.1103/PhysRevLett.105.168101.

[18] Sang Joon, Lee Taesik, and Go Hyeokjun. Three - dimensional swimming motility of microorganism in the near - wall region. *Experiments in Fluids*, 57(2):1–10, 2016. ISSN 1432-1114. doi: 10.1007/s00348-016-2113-0.

[19] Koen Muller. Collective Swimming Dynamics of Motile Micro-Algae.

[20] Marco Polin, Idan Tuval, Knut Drescher, Jerry P. Gollub, and Raymond E. Goldstein. Chlamydomonas Swims with Two Gears. *Science*, 325(July):487–490, 2009. ISSN 1687-806X. doi: 10.1126/science.1172667.

[21] A E Patteson, A Gopinath, M Goulian, and P E Arratia. Running and tumbling with E . coli in polymeric solutions. *Nature Publishing Group*, pages 1–11, 2015. doi: 10.1038/srep15761. URL http://dx.doi.org/10.1038/srep15761.

[22] Eric Lauga, Willow R. DiLuzio, George M. Whitesides, and Howard A. Stone. Swimming in circles: Motion of bacteria near solid boundaries. *Biophysical Journal*, 90(2):400–412, 2006. ISSN 00063495. doi: 10.1529/biophysj.105.069401. URL http://dx.doi.org/10.1529/biophysj.105.069401.

[23] Knut Drescher, Kyriacos C. Leptos, Idan Tuval, Takuji Ishikawa, Timothy J. Pedley, and Raymond E. Goldstein. Dancing volvox: Hydrodynamic bound states of swimming algae. *Physical Review Letters*, 102(16):1–4, 2009. ISSN 00319007. doi: 10.1103/PhysRevLett.102.168101.

[24] Allison P. Berke, Linda Turner, Howard C. Berg, and Eric Lauga. Hydrodynamic attraction of swimming microorganisms by surfaces. *Physical Review Letters*, 101(3):1–4, 2008. ISSN 00319007. doi: 10.1103/PhysRevLett.101.038102.

[25] Lord Rothschild. Non-random Distribution of Bull Spermatozoa in a Drop of Sperm Suspension. *Nature*, 198(4886):1221–1222, jun 1963. ISSN 0028-0836. doi: 10.1038/1981221a0. URL http://www.nature.com/articles/1981221a0.

[26] Gao Jin Li and Arezoo M. Ardekani. Hydrodynamic interaction of microswimmers near a wall. *Physical Review E - Statistical, Nonlinear, and Soft Matter Physics*, 90(1):1–12, 2014. ISSN 15502376. doi: 10.1103/PhysRevE.90.013010.

[27] Lailai Zhu, Eric Lauga, and Luca Brandt. Self-propulsion in viscoelastic fluids: Pushers vs. pullers. *Physics of Fluids*, 24(5), 2012. ISSN 10706631. doi: 10.1063/1.4718446. URL https://doi.org/10.1063/1.4718446.

[28] Bian Qian, Hongyuan Jiang, David A. Gagnon, Kenneth S. Breuer, and Thomas R. Powers. Minimal model for synchronization induced by hydrodynamic interactions. *Physical Review E - Statistical, Nonlinear, and Soft Matter Physics*, 80(6):1–10, 2009. ISSN 15393755. doi: 10.1103/PhysRevE.80.061919.

[29] Benjamin M. Friedrich and Frank Jülicher. Flagellar synchronization independent of hydrodynamic interactions. *Physical Review Letters*, 109(13):1–5, 2012. ISSN 00319007. doi: 10.1103/PhysRevLett.109.138102.

[30] Vasily Kantsler, Jörn Dunkel, Marco Polin, and Raymond E. Goldstein. Ciliary contact interactions dominate surface scattering of swimming eukaryotes. (4), 2013. ISSN 0027-8424. doi: 10.1073/pnas.1210548110. URL http://dx.doi.org/10.1073/pnas.1210548110.

[31] Matteo Contino, Enkeleida Lushi, Idan Tuval, Vasily Kantsler, and Marco Polin. Microalgae Scatter off Solid Surfaces by Hydrodynamic and Contact Forces. *Physical Review Letters*, 115 (25):1–5, 2015. ISSN 10797114. doi: 10.1103/PhysRevLett.115.258102.

[32] Salima Rafaï, Levan Jibuti, and Philippe Peyla. Effective viscosity of microswimmer suspensions. *Physical Review Letters*, 104(9):1–4, 2010. ISSN 10797114. doi: 10.1103/PhysRevLett.104.098102.

[33] Matthias Mussler, Salima Rafaï, Philippe Peyla, and Christian Wagner. Effective viscosity of non-gravitactic Chlamydomonas Reinhardtii microswimmer suspensions. *Epl*, 101(5), 2013. ISSN 02955075. doi: 10.1209/0295-5075/101/54004.

[34] Rob Poole. The Deborah and Weissenberg Numbers. *The British Society of Rheology,Rheology Bulletin*, 53(2):32–39, 2012.

[35] Emily E. Riley and Eric Lauga. Enhanced active swimming in viscoelastic fluids. *Epl*, 108(3), 2014. ISSN 12864854. doi: 10.1209/0295-5075/108/34003.

[36] Geoffrey Taylor. Analysis of the swimming of microscopic organisms. *Proceedings of the Royal Society of London*, 209(1099):447–461, 1951.

[37] Eric Lauga. Propulsion in a viscoelastic fluid. *Physics of Fluids*, 19(8), 2007. ISSN 10706631. doi: 10.1063/1.2751388. URL https://doi.org/10.1063/1.2751388.

[38] Henry C. Fu, Thomas R. Powers, and Charles W. Wolgemuth. Theory of swimming filaments in viscoelastic media. *Physical Review Letters*, 99(25):1–4, 2007. ISSN 00319007. doi: 10.1103/PhysRevLett.99.258101.

[39] G. J. Li, A. Karimi, and A. M. Ardekani. Effect of solid boundaries on swimming dynamics of microorganisms in a viscoelastic fluid. *Rheologica Acta*, 53(12):911–926, 2014. ISSN 00354511. doi: 10.1007/s00397-014-0796-9.

[40] Shahrzad Yazdi, Arezoo M. Ardekani, and Ali Borhan. Locomotion of microorganisms near a no-slip boundary in a viscoelastic fluid. *Physical Review E - Statistical, Nonlinear, and Soft Matter Physics*, 90(4):1–11, 2014. ISSN 15502376. doi: 10.1103/PhysRevE.90.043002.

[41] A. M. Ardekani and E. Gore. Emergence of a limit cycle for swimming microorganisms in a vortical flow of a viscoelastic fluid. *Physical Review E - Statistical, Nonlinear, and Soft Matter Physics*, 85(5):1–5, 2012. ISSN 15393755. doi: 10.1103/PhysRevE.85.056309.

[42] Shahrzad Yazdi, Arezoo M. Ardekani, and Ali Borhan. Locomotion of microorganisms near a no-slip boundary in a viscoelastic fluid. *Physical Review E - Statistical, Nonlinear, and Soft Matter Physics*, 90(4):1–11, 2014. ISSN 15502376. doi: 10.1103/PhysRevE.90.043002.

[43] Yaser Bozorgi and Patrick T. Underhill. Effect of viscoelasticity on the collective behavior of swimming microorganisms. *Physical Review E - Statistical, Nonlinear, and Soft Matter Physics*, 84(6):10–13, 2011. ISSN 15393755. doi: 10.1103/PhysRevE.84.061901.

[44] Gaojin Li and Arezoo M. Ardekani. Collective Motion of Microorganisms in a Viscoelastic Fluid. *Physical Review Letters*, 117(11):1–5, 2016. ISSN 10797114. doi: 10.1103/PhysRevLett.117.118001.

[45] Herve Nganguia, Kyle Pietrzyk, and On Shun Pak. Swimming efficiency in a shear-thinning fluid. *Physical Review E*, 96(6):1–8, 2017. ISSN 24700053. doi: 10.1103/PhysRevE.96.062606.

[46] Charu Datt, Lailai Zhu, Gwynn J. Elfring, and On Shun Pak. Squirming through shear-thinning fluids. *Journal of Fluid Mechanics*, 784:R1, 2015. ISSN 14697645. doi: 10.1017/jfm.2015.600.

[47] Howard C. Berg and Linda Turner. Movement of microorganisms in viscous environments. *Nature*, 278(5702):349–351, mar 1979. ISSN 0028-0836. doi: 10.1038/278349a0. URL `http://www.nature.com/articles/278349a0`.

[48] Nathan C. Keim, Mike Garcia, and Paulo E. Arratia. Fluid elasticity can enable propulsion at low Reynolds number. *Physics of Fluids*, 24(8), 2012. ISSN 10706631. doi: 10.1063/1.4746792. URL `https://doi.org/10.1063/1.4746792`.

[49] Siti Aminah Ahmed, Doblin Anak Sandai, Suzana Musa, Hoe Chee Hock, Mehdi Riadzi, Lau Kwok Leong, and Tang Thean Hock. Rapid Diagnosis of Leptospirosis by Multiplex PCR. *Malaysian Journal of Medical Sciences*, 19(3):9–16, 2012. ISSN 1394195X. doi: 10.1103/PhysRevLett.106.208101.

[50] D. A. Gagnon, N. C. Keim, and P. E. Arratia. Undulatory swimming in shear-thinning fluids: Experiments with Caenorhabditis elegans. *Journal of Fluid Mechanics*, 758:R3, 2014. ISSN 14697645. doi: 10.1017/jfm.2014.539.

[51] Julian Espinosa-Garcia, Eric Lauga, and Roberto Zenit. Fluid elasticity increases the locomotion of flexible swimmers. *Physics of Fluids*, 25(3):1–7, 2013. ISSN 10706631. doi: 10.1063/1.4795166. URL `https://doi.org/10.1063/1.4795166`.

[52] B. Qin, A. Gopinath, J. Yang, J. P. Gollub, and P. E. Arratia. Flagellar kinematics and swimming of algal cells in viscoelastic fluids. *Scientific Reports*, 5:1–7, 2015. ISSN 20452322. doi: 10.1038/srep09190.

[53] Chuanbin Li, Boyang Qin, Arvind Gopinath, Paulo E. Arratia, Becca Thomases, and Robert D. Guy. Flagellar swimming in viscoelastic fluids: Role of fluid elastic stress revealed by simulations based on experimental data. *Journal of the Royal Society Interface*, 14(135), 2017. ISSN 17425662. doi: 10.1098/rsif.2017.0289.

[54] H C Crenshaw. A new look at locomotion in microorganisms: rotating and translating. (part of a special issue on aquatic locomotion). *Am. Zool. 36: 608-18*, 618:608–618, 1997.

[55] H C Crenshaw (et al). Analysis of the 3-D trajectories of organisms: Estimates of velocity, curvature, and torsion from positional information. *Jeb*, 203:961–982, 2000.

[56] Rasika M. Harshey. Bacterial motility on a surface: Many ways to a common goal. *Annual Review of Microbiology*, 57(1):249–273, 2003. doi: 10.1146/annurev.micro.57.030502.091014. URL https://doi.org/10.1146/annurev.micro.57.030502.091014. PMID: 14527279.

[57] Nhan Phan-Thien. *Understanding Viscoelasticity*. Graduate Texts in Physics. Springer Berlin Heidelberg, Berlin, Heidelberg, 2013. ISBN 978-3-642-32957-9. doi: 10.1007/978-3-642-32958-6. URL http://link.springer.com/10.1007/978-3-642-32958-6.

[58] Marc André Meyers and Krishan Kumar Chawla. *Mechanical Behavior of Materials*. Cambridge University Press, 2 edition, 2008. doi: 10.1017/CBO9780511810947.

[59] Hiong Yap Gan and Yee Cheong Lam. *Viscoelasticity*, pages 1–12. Springer US, Boston, MA, 2013. ISBN 978-3-642-27758-0. doi: 10.1007/978-3-642-27758-0_1666-2. URL https://doi.org/10.1007/978-3-642-27758-0_1666-2.

[60] Tim A. Osswald, Georg Menges, Tim A. Osswald, and Georg Menges. Rheology of Polymer Melts. *Materials Science of Polymers for Engineers*, pages 111–159, 2012. doi: 10.3139/9781569905241.005.

[61] C. Gallegos and M. García-Morales. Rheology of polymer-modified bitumens. *Polymer Modified Bitumen*, pages 197–237, 2011. doi: 10.1016/B978-0-85709-048-5.50007-9.

[62] Vincent A. Martinez, Jana Schwarz-Linek, Mathias Reufer, Laurence G. Wilson, Alexander N. Morozov, and Wilson C. K. Poon. Flagellated bacterial motility in polymer solutions. 111 (50):17771–17776, 2014. doi: 10.1073/pnas.1415460111. URL http://dx.doi.org/10.1073/pnas.1415460111.

[63] Claudia Barba, Daniel Montané, Marguerite Rinaudo, and Xavier Farriol. Synthesis and characterization of carboxymethylcelluloses (CMC) from non-wood fibers I. Accessibility of cellulose fibers and CMC synthesis. *Cellulose*, 9(3-4):319–326, 2002. ISSN 09690239. doi: 10.1023/A:1021184509189.

[64] Chen Sheng, Bao Wenting, Tu Shijian, and Wang Yuechuan. Electrochromic Behaviors of Poly (3-n-octyloxythiophene). *Polymer*, (April), 2008. doi: 10.1002/app.

[65] Ling Zhang, Huicui Sun, Bo Han, Li Peng, Fulong Ning, Guosheng Jiang, and V. F. Chehotkin. Effect of shearing actions on the rheological properties and mesostructures of CMC, PVP and CMC + PVP aqueous solutions as simple water-based drilling fluids for gas hydrate drilling. *Journal of Unconventional Oil and Gas Resources*, 14:86–98, 2016. ISSN 22133976. doi: 10.1016/j.juogr.2016.02.002. URL http://dx.doi.org/10.1016/j.juogr.2016.02.002.

[66] J Kulicke,W.M, Kniewske,R and Klein. Preparation,Characteristics,Solution Properties and Rheological Behaviour of Polyacrylamide. *Progress in Polymer Science*, 8:373–468, 1982.

[67] G Pesce, A C De Luca, R R Brau, and J M Ferrer. Reports on Progress in Physics Related content Microrheology of complex fluids. *Reports on Progress in Physics*, 68:685–742, 2005. doi: 10.1088/0034-4885/68/3/R04.

[68] Karim M. Addas, Christoph F. Schmidt, and Jay X. Tang. Microrheology of solutions of semiflexible biopolymer filaments using laser tweezers interferometry. *Physical Review E - Statistical Physics, Plasmas, Fluids, and Related Interdisciplinary Topics*, 70(2):16, 2004. ISSN 1063651X. doi: 10.1103/PhysRevE.70.021503.

[69] Hyungsuk Lee, Jorge M Ferrer, Fumihiko Nakamura, Matthew J Lang, and Roger D Kamm. Passive and active microrheology for cross-linked F-actin networks in vitro. *Acta Biomaterialia*, 6(4):1207–1218, 2010. ISSN 1742-7061. doi: 10.1016/j.actbio.2009.10.044. URL http://dx.doi.org/10.1016/j.actbio.2009.10.044.

[70] Keir C Neuman and Steven M Block. Optical trapping. *The Review of scientific instruments*, 75(9):2787–809, 2004. ISSN 0034-6748. doi: 10.1063/1.1785844. URL http://www.ncbi.nlm.nih.gov/pubmed/16878180{%}0Ahttp://www.pubmedcentral.nih.gov/articlerender.fcgi?artid=PMC1523313.

[71] Da Wei, Parviz Ghoddoosi Dehnavi, Marie Eve Aubin-Tam, and Daniel Tam. Is the Zero Reynolds Number Approximation Valid for Ciliary Flows? *Physical Review Letters*, 122(12):124502, 2019. ISSN 10797114. doi: 10.1103/PhysRevLett.122.124502. URL https://doi.org/10.1103/PhysRevLett.122.124502.

[72] Matthew J. Lang, Charles L. Asbury, Joshua W. Shaevitz, and Steven M. Block. An automated two-dimensional optical force clamp for single molecule studies. *Biophysical Journal*, 83(1):491–501, 2002. ISSN 00063495. doi: 10.1016/S0006-3495(02)75185-0.

[73] Kirstine Berg-Sørensen and Henrik Flyvbjerg. Power spectrum analysis for optical tweezers. *Review of Scientific Instruments*, 75(3):594–612, 2004. ISSN 00346748. doi: 10.1063/1.1645654.

[74] B. Schnurr, F. Gittes, F. C. MacKintosh, and C. F. Schmidt. Determining Microscopic Viscoelasticity in Flexible and Semiflexible Polymer Networks from Thermal Fluctuations. *Macromolecules*, 30(25):7781–7792, dec 1997. ISSN 0024-9297. doi: 10.1021/ma970555n. URL https://pubs.acs.org/doi/10.1021/ma970555n.

[75] Hyoungsoo Kim, Jerry Westerweel, and Gerrit E. Elsinga. Comparison of Tomo-PIV and 3D-PTV for microfluidic flows. *Measurement Science and Technology*, 24(2), 2013. ISSN 13616501. doi: 10.1088/0957-0233/24/2/024007.

[76] Hyoungsoo Kim, Sebastian Groe, Gerrit E. Elsinga, and Jerry Westerweel. Full 3D-3C velocity measurement inside a liquid immersion droplet. *Experiments in Fluids*, 51(2):395–405, 2011. ISSN 07234864. doi: 10.1007/s00348-011-1053-y.

[77] Kyriacos C. Leptos, Jeffrey S. Guasto, J. P. Gollub, Adriana I. Pesci, and Raymond E. Goldstein. Dynamics of Enhanced Tracer Diffusion in Suspensions of Swimming Eukaryotic Microorganisms. *Physical Review Letters*, 103(19):1–4, 2009. ISSN 00319007. doi: 10.1103/PhysRevLett.103.198103.

[78] Greta Quaranta, Marie Eve Aubin-Tam, and Daniel Tam. Hydrodynamics Versus Intracellular Coupling in the Synchronization of Eukaryotic Flagella. *Physical Review Letters*, 115(23):1–5, 2015. ISSN 10797114. doi: 10.1103/PhysRevLett.115.238101.

[79] Beata Sweryda-Krawiec, Halagowder Devaraj, George Jacob, and James J. Hickman. A New Interpretation of Serum Albumin Surface Passivation. *Langmuir*, 20(6):2054–2056, 2004. ISSN 07437463. doi: 10.1021/la034870g.

[80] Ronald Adrian and Jerry Westerweel. *Particle Image Velocimetry*. Cambridge University Press, Cambridge,New York, 2011. ISBN 978-0-521-44008-0.

[81] A. Attanasi, A. Cavagna, L. D. Castello, I. Giardina, A. Jelić, S. Melillo, L. Parisi, F. Pellacini, E. Shen, E. Silvestri, and M. Viale. Greta-a novel global and recursive tracking algorithm in three dimensions. *IEEE Transactions on Pattern Analysis and Machine Intelligence*, 37(12):2451–2463, Dec 2015. ISSN 0162-8828. doi: 10.1109/TPAMI.2015.2414427.

[82] D. Maas, H.G.; Gruen, A.; Papantoniou. Experiments in Fluids: Particle tracking velocimetry in three-dimensional flows. *International Archives of Photogrammetry and Remote Sensing*, 146: 133–146, 1993.

[83] Jochen Willneff and Armin Gruen. A New Spatio-Temporal Matching Algorithm For 3D-Particle Tracking Velocimetry. *The 9th of International Symposium on Transport Phenomena and Dynamics of Rotating Machinery*, pages 1–7, 2002.

[84] H. C. Crenshaw. Kinematics of helical motion of microorganisms capable of motion with four degrees of freedom. *Biophysical Journal*, 56(5):1029–1035, 1989. ISSN 00063495. doi: 10.1016/S0006-3495(89)82748-1. URL http://dx.doi.org/10.1016/S0006-3495(89)82748-1.

[85] Eric Lauga and Thomas R Powers. The hydrodynamics of swimming microorganisms. *Reports on Progress in Physics*, 72(9):096601, sep 2009. ISSN 0034-4885. doi: 10.1088/0034-4885/72/9/096601. URL http://arxiv.org/abs/0812.2887http://dx.doi.org/10.1088/0034-4885/72/9/096601http://stacks.iop.org/0034-4885/72/i=9/a=096601?key=crossref.736a5c13368e75b7395f94099aead8e4.

[86] S. Yazdi, A. M. Ardekani, and A. Borhan. Swimming Dynamics Near a Wall in a Weakly Elastic Fluid. *Journal of Nonlinear Science*, 25(5):1153–1167, 2015. ISSN 14321467. doi: 10.1007/s00332-015-9253-x.